Stony Brook University

Ultrafast Coherent Control Spectroscopy

A Dissertation Presented

by

Chien-hung Tseng

to

The Graduate School

in Partial Fulfillment of the Requirements

for the Degree of

Doctor of Philosophy

in

Physics

Stony Brook University

May 2012

Stony Brook University

The Graduate School

Chien-hung Tseng

We, the dissertation committee for the above candidate for the Doctor of Philosophy degree, hereby recommend acceptance of this dissertation.

Thomas C. Weinacht - Advisor
Associate Professor, Department of Physics and Astronomy

Dominik Schneble - Chairperson of defence
Associate Professor, Department of Physics and Astronomy

Maria Victoria Fernandez-Serra
Assistant Professor, Department of Physics, Stony Brook University

Sanford Ruhman
Professor, Department of Physical Chemistry, Hebrew University of Jerusalem

This dissertation is accepted by the Graduate School

Charles Taber
Interim Dean of the Graduate School

Abstract of the Dissertation

Ultrafast Coherent Control Spectroscopy

by

Chien-hung Tseng

Doctor of Philosophy

in

Physics

Stony Brook University

2012

Coherent control of quantum systems is currently a very active area of research in physics and chemistry. The goal of coherent control is to prepare molecules in specific quantum states that can lead to different chemical reactions, e.g. fragmentation and isomerization. One approach is the control of interference between multiple quantum pathways via their phases from the initial to the final state which consequently excites one molecular state or molecule over another with shaped pulses. The other approach is to generate different reaction products with pulses that match specific transient Franck Condon windows and transfer the wavepacket in a precise phase of vibrational motion to a new electronic state.

Recently, there are increasing applications of coherent control towards cellular imaging. It is especially beneficial for distinguishing broadband fluorophores with similar two-photon absorption cross-sections, e.g. for free and enzyme-bound nicotinamide adenine dinucleotide (NADH). In this thesis, we discriminate between samples

containing either free NADH or enzyme-bound NADH solutions with pulses that have a π phase jump at a given frequency within the excitation bandwidth. This parameter scan is sensitive to as low as 3% of binding. The same idea can be generalized to other two-photon fluorescence systems, and a closed-loop feedback control approach should allow even wider application.

We also develop two-dimensional (2D) Fourier transform spectroscopy in the deep UV (262 nm) to study DNA bases excited state relaxation dynamics. We compare 2D spectroscopy measurements in the deep UV for monomeric adenine and uracil in aqueous solutions. Both molecules show excited state absorption on short timescales and ground state bleach extending for over 1 ps. While the 2D spectrum for uracil shows changes in the center of gravity during the first few hundred femtoseconds, the center of gravity of the 2D spectrum for adenine does not show similar changes. We discuss our results in light of *ab initio* electronic structure calculations.

To my family.

Contents

List of Figures **viii**

Acknowledgements **x**

1 Introduction **1**

2 Experimental Apparatus **5**

2.1 Ultrafast Laser System 5

2.2 Pulse Shaper 6

2.3 2PF Spectroscopy 8

2.4 2D Spectroscopy in the Deep UV 8

3 Coherent Control Two-Photon Fluorescence Spectroscopy **16**

3.1 Time-Dependent Perturbation Theory 17

3.1.1 Interaction picture 18

3.1.2 Two level systems in electric fields 20

3.1.3 Multiphoton transitions in weak fields 21

3.1.4 Control the TPA probability with a pulse with a π phase jump in the spectrum 22

3.2 Distinguishing between different states of NADH 25

3.2.1 NADH as an intrinsic fluorophore 25

3.2.2 π scans on NADH 28

4 2D Spectroscopy in the Deep UV **35**

4.1 Theory 36

4.1.1 Density operator 36

4.1.2 Perturbation expansion 37

4.1.3 Polarization and nonlinear response function 39
4.1.4 n-wave mixing signal 41
4.1.5 Linear response 43
4.1.6 Third-order response function 45
4.2 Two-dimensional spectroscopy 46
4.2.1 Photon echo spectroscopy 50
4.2.2 Impulsive limit 52
4.2.3 Heterodyne detection 53
4.2.4 Collinear measurement 55
4.2.5 Hole burning spectroscopy 57
4.2.6 Phase-locked pump-probe spectroscopy 59
4.2.7 Recovering rephasing and non-rephasing spectra from PLPP measurements 61
4.2.8 Generating phase-locked pulses with a pulse shaper . . 62
4.3 Ultrafast measurements on DNA bases 63
4.4 2D spectroscopy on adenine and uracil in aqueous solutions . . 65
4.4.1 Background subtraction 65
4.4.2 Center of gravity (COG) and variance 68
4.4.3 UV-UV pump-probe measurements on adenine and uracil vapor 72
4.4.4 Discussion 73

5 Conclusion and Perspectives **79**

Bibliography **82**

A Appendix: NADH Solution Preparation **94**

B Appendix: Inhomogeneous Line-broadening **95**
B.1 Time evolution operator of a time dependent Hamiltonian . . 96
B.2 Fluctuating transition frequencies for a two electronic level system 97

List of Figures

1.1 Two approaches to coherent control. 2

2.1 Pulse shaper. 7
2.2 Experimental setup for 2PF spectroscopy. 9
2.3 Experimental setup for 2D UV spectroscopy. 11
2.4 Relative phase between pump-pump pulse pair. 13

3.1 Intensity and phase for a pulse with π phase jump. 23
3.2 SHG-FROG for TL and π phase flip pulses and 2P power spectrum. 25
3.3 Single photon absorption and emission spectrum of pure NADH and mMDH-bound NADH. 26
3.4 π scan traces for pure NADH and MDH-bound NADH solutions. 29
3.5 Ratio of the fluorescence signal vs. NADH-MDH binding fraction. 30
3.6 π scan traces vs. chirp for pure NADH solution. 31
3.7 Histogram distributions for fluorescence ratio of different states of NADH solutions. 33
3.8 π scan traces vs. temperature for NADH solutions. 34

4.1 Time ordering 40
4.2 Liouville pathways four-wave-mixing in a two-level system. . . 47
4.3 Schematic layouts of 2D spectroscopy. 49
4.4 Liouville pathways for pump-probe and hole burning spectroscopy. 58
4.5 Adenine and Uracil UV-Vis spectrum. 64
4.6 Adenine 2D spectrum with water subtraction 67
4.7 Horizontal lineouts for adenine 2D spectrum with different amount of water subtraction 67

4.8 Adenine 2D spectrum 69
4.9 Uracil 2D spectrum 70
4.10 COG and variance along diagonal and anti-diagonal axes for adenine and uracil spectrum 71
4.11 Magnitude of the 2D signal as a function of pump probe delay for adenine and uracil. 72
4.12 Adenine and uracil ion yields vs pump probe delay. 73
4.13 Neutral and ionic energies of (A) adenine and (B) uracil. . . . 74
4.14 Cartoons illustrating the excited-state PES for (A) adenine and (B) uracil near the FC region. 76
4.15 Adenine tautomers 76

Acknowledgements

I have to thank many people for making this thesis possible. Thanks to my advisor, Tom Weinacht, for all his support, guidance and tolerance over the years. Discussion with Tom and working with him in the lab are always inspiring and fruitful.

Many big thanks to our current and former group members. Péter Sandor, with whom we improved the 2D spectroscopy setup together. There are many days that we had to search for timezero until late or to take long night shifts, Péter has been super-supportive and helpful. The work in Chapter 3 was done in collaboration with Brett Pearson when he was on sabbatical in Stony Brook. I really enjoy discussion and working together with Brett, he always has great suggestions and comments. Before I joined the group, I worked on an Optics Rotation project with Marty, that we looked into improving the performance of the acoustio-optic modulator. In later years, whenever I had to fix our amplifier system, had problem with the pulse-shaper, or was drafting my presentation, Martin Cohen always gives excellent advice. Thank you, Marty. Thanks also to Marija Kotur, Steve Clow, Dominik Geissler, Ian Borukhovich, Matt Murray, and Oumarou Njoya, for providing a pool of ideas and a spare pair of hands in the lab. Thanks to Spiridoula Matsika in Temple University for the *ab initio* calculations on adenine and uracil and many discussions to help us interpret our measurement.

The AMO group has been a great support. Thanks to Harold Metcalf, Dominik Schneble, and Tom Bergemann for keeping the AMO group fun and productive. The Metcalf and the Schneble groups were always generous and helpful with finding a crucial piece of equipment. It was great to be part of the AOM group.

Many thanks also to staff in the Department. Especially to Walter Schmeling and Jeff Slechta of the machine shop who helped us build the sample holder essential for the 2D measurements. And to Andrzej Lipski for making us a

glass cell, and many interesting chats that lift my spirit though out the day. Thanks to Chuck Pancake and Eugene Shafto of the electronics shop for looking into the control circuit board of our pump laser, it was relieving to know that the board was fine and we were able to fix the problem in house to continue our experiments. And thanks to all the main office staff, who made everything administrative as easy as possible and always greeted me with a smile.

Finally, thanks to my family for all the love, support, and patience.

Chapter 1

Introduction

Coherent control has drawn interest in the Atomic, Molecular, and Optical (AMO) community because it can steer a photoreaction towards a desired product channel through shaped excitation pulses. Brumer and Shapiro proposed that control can be achieved by interference between possible pathways that lead to the desired product state [1]. For example, in photo-induced transitions between molecular energy states, we can enhance or suppress the multiphoton transition probability by tailoring the spectral phase of the excitation pulses [2, 3]. Another approach to control introduced by Tannor and Rice [4, 5] is to steer the molecular wavepacket out from one of the exit channels (e.g. dissociation) by matching the ultrafast pulses to specific vertical transition (Frank Condon) windows. The first pulse transfers ground state wave function vertically and launches the wavepacket to the excited state. The wavepacket propagates on the excited potential energy surface (PES) and evolves with time. Finally, the second pulse leads to another vertical transition, and the propagation time on the excited state PES (i.e. the position from where the wavepacket is "dumped" by the second pulse) is determined by the delay between the two ultrafast pulses. Wavepackets produced at different positions on the excited state PES can result in different products [5]. Figure 1.1 illustrates the two approaches to coherent control.

This thesis describes coherent control spectroscopy in the weak field regime where the evolution of quantum states can be solved by the time-dependent perturbation theory. We apply coherent control to functional two-photon fluorescence (2PF) cellular imaging. As the name suggests, 2PF measures the

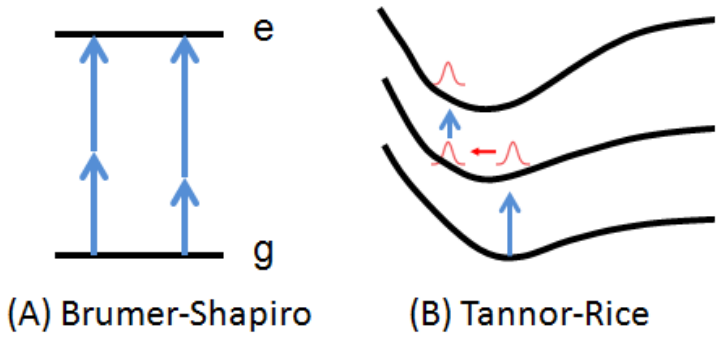

Figure 1.1: Two approaches to coherent control. Blue arrows refer to photo-induced transitions, and the red arrow is the wavepacket motion on the PES. Left panel: the Brumer-Shapiro approach, which controls the transition probability by tailoring the interference between possible pathways to the final state. Right panel: the Tannor-Rice approach, which exploits the wavepacket dynamics to steer the wavepacket to different exit channels by varying the delay between the pump and "dump" pulses.

fluorescence from two-photon transitions. Since the two-photon absorption (TPA) only occurs when the photon flux is sufficiently high, the 2PF signal can only be induced from the area in the sample where the laser is focused, and the sample away from the focus will not have contribution to the signal. When applied to imaging, it has the benefit of better spatial resolution, less background, and larger penetration depth. Coherent control spectroscopy has been demonstrated to selectively excite different fluorescent probes and detect the same probe in different pH environments [6–11]. Meshulach *et al.* show that it is possible to control a non-resonant two-photon transition by tailoring the spectral phase. For example, the TPA probability is maximized when the laser pulse is transform-limited, or when there is a π phase jump at half of transition frequency in the laser spectrum [2, 3]. In this thesis, we use π phase scans to discriminate between unbound and enzyme-bound forms of NADH in solutions. The two forms of NADH have very similar single-photon absorption and emission spectrum, and it requires spectrofluorometry or fluorescence-lifetime-imaging measurements to distinguish between the two. In contrast, we are able to excite the TPA of the two forms of NADH and probe their difference in the TPA spectrum with shaped pulses from a single laser. As we apply a π phase scan to the NADH, the two forms of NADH respond differ-

ently to the field because of the difference in their TPA spectrum. We can determine the enzyme binding ratio of NADH by exciting the sample with two pulse shapes in succession without measuring the fluorescence spectrum.

We also measure the excited electronic state relaxation dynamics of DNA bases under UV radiation with third-order coherent spectroscopy, which is generally known as the two-dimensional Fourier transform spectroscopy. There is continuous interest in excited electronic states of DNA because they are the precursors to mutations. One-dimensional ultrafast spectroscopy measurements indicate that the DNA bases can return nonradiatively to the ground state through internal conversion. But one-dimensional spectroscopy has its limitations. For molecules in condensed medium, inhomogeneous broadening due to variation of the local environment makes it difficult to extract structural information and molecular dynamics from the measurement. It has been proposed that 2D spectroscopy, the optical analog of NMR, might have less of a contribution from inhomogeneous broadening. It has been predicted that 2D spectrum can correlate initial and final position within vibrational wavepackets [12], so we would like to elucidate the wavepacket dynamics of DNA bases under UV exposure with 2D spectroscopy measurements.

This thesis is composed of five chapters and two appendices. Chapter 2 shows the details of the laser system, the ultrafast pulse-shaper, and the setups for coherent control 2PF spectroscopy and 2D Fourier transform spectroscopy. It also explains how we tackled possible sources of error, e.g. laser intensity fluctuations, beam-pointing instability, background signal due UV absorption by the solvent, in the 2D spectroscopy measurements.

In Chapter 3, we introduce the theory of multiphoton absorption in the weak field limit and demonstrate that the multiphoton transition probability is sensitive to the spectral phase of the excitation pulse. Two forms of NADH in solutions with similar two-photon absorption cross section can be identified by coherent control spectroscopy. This technique is also sensitive to change in the enzyme-biding ratio of NADH caused by variation in the solution temperature.

Chapter 4 gives an overview of the two-dimensional Fourier transform spectroscopy. We start from constructing the third-order response of photon-matter interaction with time-dependent perturbation theory. Different excitation and detection geometries of 2D spectroscopy are introduced in this

chapter. Finally, we present 2D spectrum of single adenine and uracil. Both of them show excited state absorption (ESA) for short times (< 100 fs), and ground state bleach (GSB) extending for long times (> 1 ps). Uracil shows an evolution of the 2D spectrum on a $100 \sim 300$ fs timescale, which adenine does not. We interpret this difference between adenine and uracil in terms of the slope of the excited state potential energy surface near the Frank Condon (FC) region. We give the conclusion and discuss possible future projects and improvement to the setup in Chapter 5.

Chapter 2

Experimental Apparatus

In this chapter we will describe two experimental apparatus for ultrafast coherent control spectroscopy - the first one is two-photon-fluorescence (2PF) spectroscopy and the second one is two-dimensional (2D) Fourier transform spectroscopy in the deep UV. Both experiments measure molecular response of targeted systems after they are excited by shaped ultrafast laser pulses. In 2PF spectroscopy, we measure the fluorescence yields from fluorescent proteins and coenzyme-enzyme solutions as a function of different shaped IR (780 nm) pulses to distinguish different proteins and enzyme-binding states without spectrally resolve fluorescence. In 2D UV spectroscopy, we excite DNA bases with phase-locked UV (260 nm) pump pulses and measure probe transmission spectrum as a function of pump-pump delay. Both spectroscopies made use of our ultrafast laser system, which is described below.

2.1 Ultrafast Laser System

Our laser system consists of a modelocked Ti:Sapphire oscillator (KM Labs model TS), which seeds the Ti:Sapphire, chirped-pulse amplified ultrafast laser amplifier (KM Labs HAP-AMP). The oscillator is pumped by a Coherent Verdi V5 Continuous Wave (CW) laser and the amplifier by a Quantronix Q-switched Nd:YLF laser. The amplifier operates at 1 kHz, with pulse duration 30 fs and average power 1 W. The laser central wavelength is at 780 nm and can be tuned by several nanometers by a pellicle in the amplifier cavity.

2.2 Pulse Shaper

Because the pulse duration for femtosecond pulses are much shorter than the fastest electronics available, it is impossible to shape laser pulses directly in real time by conventional switches. Here, we followed Weiner's proposal [13] to shape the pulse in the spectral domain that includes (1) spatial Fourier analysis of the incident pulse, (2) spatial filtering of the dispersed frequencies, and (3) recombination of all the frequencies into a single collimated beam. Figure 2.1 shows a schematic diagram of the pulse shaper used in our lab, which employs the concept of 4F correlator in Fourier optics. The first grating (GT1) and converging mirror (CM1) first spatially separate the frequency components of the incoming pulse, then in the Fourier plane of the zero-dispersion line, we apply a programmable amplitude/phase mask with an acousto-optic modulator (AOM) to shape light in the frequency domain. The shaped pulse spectrum $E(\omega)_{shaped}$ is

$$E(\omega)_{shaped} = E(\omega)_{input} \times M(\omega) \tag{2.1}$$

where $E(\omega)_{input}$ is the input pulse spectrum and $M(\omega)$ the amplitude/phase mask programmed on the AOM. We use an arbitrary waveform function generator (GAGE Compugen 11G) to send out desirable radio frequency (RF) voltage signals of 150 MHz to drive a piezoelectric transducer next to the AOM and generate RF waves inside the AOM crystal. When traveling though the crystal, laser pulses experience Bragg diffraction, and amplitude/phase modulations in the RF waves will write on the diffracted light and therefore modify its amplitude/phase. Besides AOMs [14, 15], other spatial light modulators (SLM) like liquid crystal arrays can also serve as pulse shaping masks, but AOMs provide a continuous phase/amplitude mask and rapid waveform refresh rates so we chose to use an AOM in our setup. After the AOM, one focal length away from the Fourier plane, the second curved mirror performs the second Fourier transform from the masking plane to the plane of the second grating, where all colors are combined back to a collimated beam.

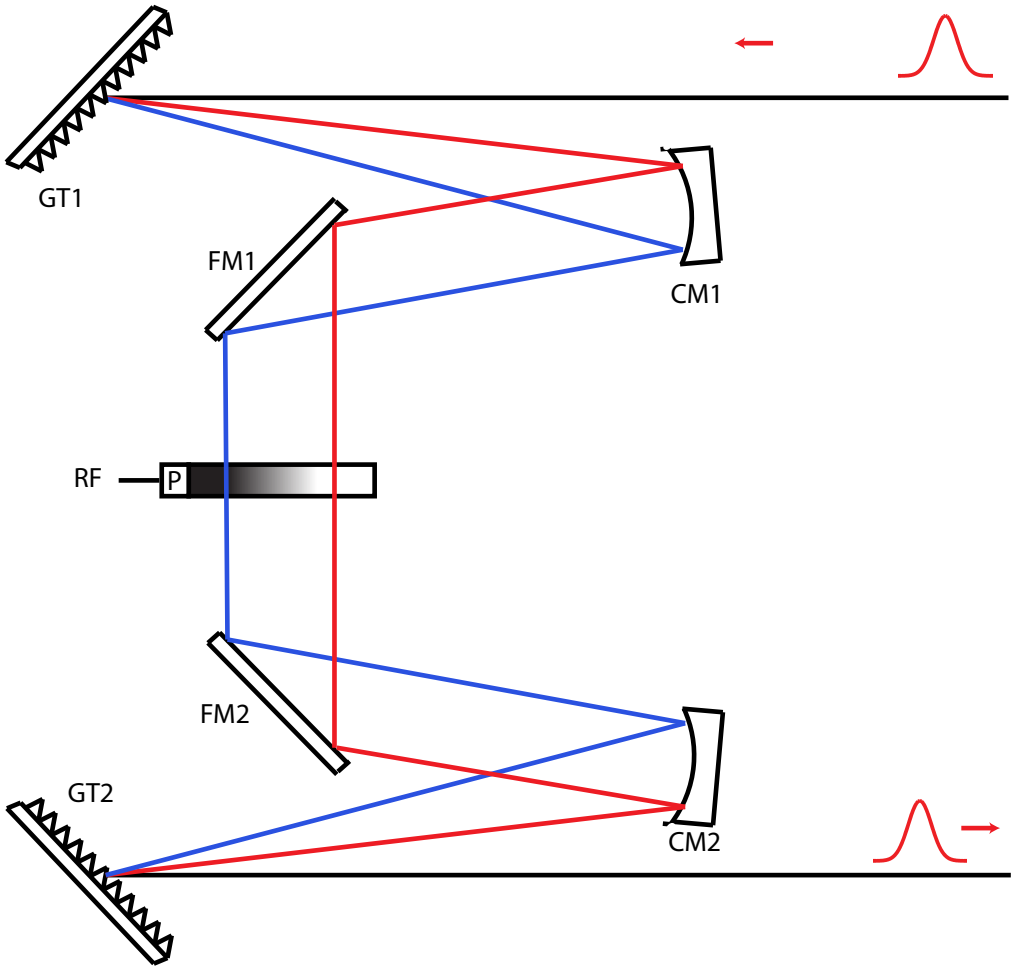

Figure 2.1: Pulse shaper. GT1, GT2: diffraction gratings; CM1, CM2: curved mirrors; FM1, FM2: folding mirrors; P: piezoelectric transducer. The AOM applies an amplitude/phase mask to the laser spectrum in the Fourier plane.

2.3 2PF Spectroscopy

Two-photon fluorescence microscopy has been widely used in biomedical imaging as it provides better optical sectioning, higher resolution, deeper penetration depth and less photodamaging and photodamage [16–18] than traditional confocal microscopy. Recently, coherent control techniques have been applied to nonlinear microscopy for selective excitation of different fluorescence probes and of the same probe in different environments [6–11]. Here we developed 2PF spectroscopy with shaped excitation pulses to distinguish fluorescence molecules that have similar two-photon absorption and emission spectrum without the need of spectrally resolving fluorescence spectrum. This technique can selectively excite different fluorescence molecules and detect NADH-enzyme binding states.

Figure 2.2 illustrates the experimental setup for 2PF spectroscopy. The excitation IR pulses are shaped in phase and/or amplitude according to the specific character of the samples of interest. Then we can selectively enhance fluorescence from certain molecule with designated excitation pulse shapes. The desirable pulse shape can be determined by closed-loop feedback genetic algorithm (GA) [19–22] or by performing parameter scans (e.g. π phase flip scans, sinusoidal phase scans). The excitation pulse energy is tuned down to 25 μJ and focused into the cuvettes with a long 1 m lens to avoid three-photon absorption and photodamaging. Several fluorescent samples are used to demonstrate the feasibility of this technique: the fluorescent proteins and dyes (eGFP, citrine, cherry, Alexa, and Fluorescein) are stored in PBS buffer, and fluorescent coenzyme reduced nicotinamide adenine dinucleotide (NADH) (Acros) is kept in Trizma (Sigma Aldrich, pH 7.0, 1 M) buffer. The induced 2PF is converted to magnified electronic signal by photo multiplier tubes (PMTs) and finally measured by a PC based oscilloscope (Gage Compuscope).

2.4 2D Spectroscopy in the Deep UV

2D Fourier transform ultrafast infrared (IR) and electronic spectroscopies have become powerful techniques for studying biological and physical systems. 2D spectroscopies provide information on molecular structure and energy transfer, e.g. protein-folding, electronic couplings in photosynthesis and semiconduc-

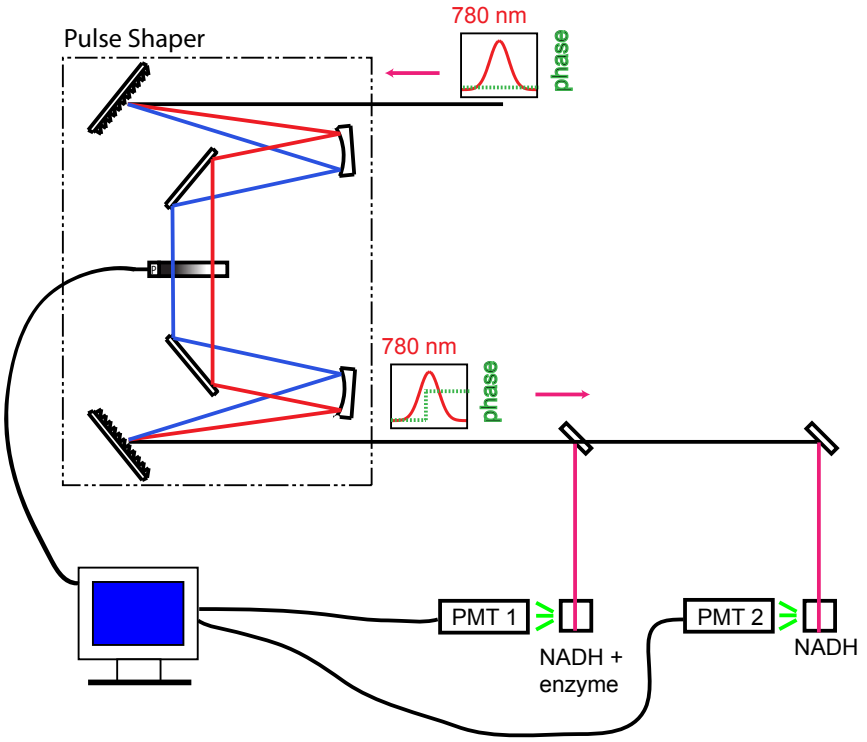

Figure 2.2: Experimental setup for 2PF spectroscopy. The pulse shaper apply a π phase jump at different frequencies in the laser spectrum.

tor carrier dynamics [12, 23, 24]. In 2D spectroscopies, one measures the third order polarization generated by a pair of excitation pulses. It is crucial to maintain the phase (time) stability between these excitation pulses. Experiments have maintained the phase stability between excitation pulses via diffractive optics [25, 26], active interferometric stabilization [27] and most recently by generating phase-locked pulses in the collinear or boxcar geometry with a pulse-shaper [28–31]. Performing 2D spectroscopy with a pulse shaper in a pump-probe geometry allows taking measurements with a very simple experimental setup [30]. In this approach, one measures absorptive spectra and is able to work in a rotating frame and implement phase-cycling [28, 32] for relaxed sampling requirements, selectivity in the couplings measured, and improved signal to noise.

While there have been many advances made in 2D spectroscopy over the past few years, 2D spectroscopy has been limited to the IR and visible regime although many molecules of interest absorb in the UV and deep UV. The phase stability required for 2D UV spectroscopy is over an order of magnitude greater than that for 2D IR spectroscopy because of the difference in wavelength. For 1/100 of a cycle phase stability between pulses, one requires a timing jitter between excitation pulses of less than 10 attoseconds, which is quite demanding using a conventional interferometer-based setup. Here, we demonstrate pulse shaper assisted 2D UV ($\sim$ 262 nm) spectroscopy at the S_0-S_1 transition band for many interesting molecules. Figure 2.3 shows the apparatus for 2D UV spectrsocopy. Pulses from the amplified Ti:sapphire laser system are separated into two beams with an 80/20 beam-splitter. We produce UV pulses (λ_0=262 nm) in both beams via third harmonic generation using an array of three Beta-Barium Borate (BBO) crystals. We use the first crystal for second harmonic generation (SHG), the second for group velocity dispersion compensation of the remaining fundamental and second harmonic, and the third crystal for sum frequency generation to obtain the third harmonic. The resulting third-harmonic UV pulses have a bandwidth of 13 THZ (433 cm^{-1}) and a pulse duration slightly under 50 fs.

In order to generate phased-locked UV pump-pump pulses for the 2D experiment, the stronger UV beam goes through a computer controlled acousto-optic modulator (AOM) based ultrafast pulse shaper [14, 33]. Unlike an interferom-

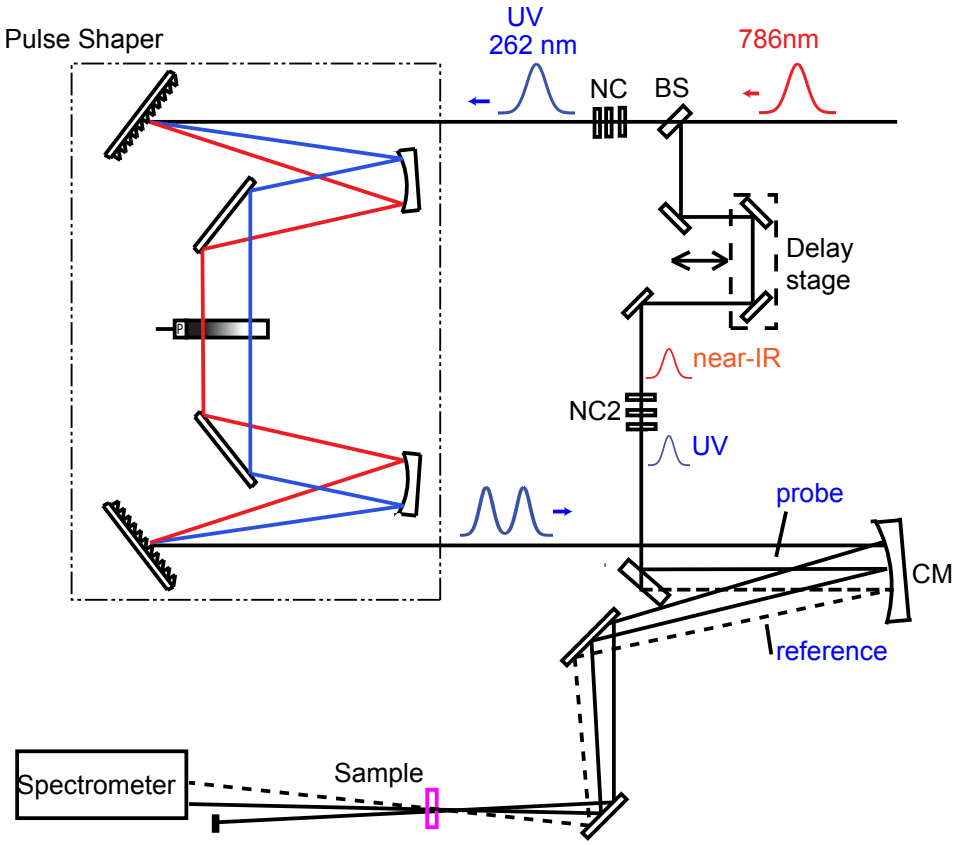

Figure 2.3: Experimental setup for 2D UV spectroscopy. BS: 80/20 beam splitter, NC and NC2: nonlinear third-harmonic-generation crystals, CM: UV-Aluminum curved mirror with focal length = 500 mm.

eter, the pulse shaper can independently control the delay (τ) and phase (ϕ_{12}) between pulses, and naturally produces phase stable pulse pairs. The phase mask to be programmed on the AOM to generate a phase-locked pulse-pair can be described by

$$M(\omega) = \frac{1}{2}[e^{i(2\pi f t_{ac}+\phi_1)} + e^{i(2\pi f t_{ac}+\phi_1)}] \tag{2.2}$$

where ϕ_1 and ϕ_2 correspond to the phase of pulses at $t = 0$ and $t = \tau$ respectively, and $\phi_2(\omega) = \phi_1(\omega) + \omega \cdot \tau$. f is the carrier frequency of the acoustic wave, and t_{ac} is the time-axis for the acoustic wave. Because the acoustic wave is static to the femtosecond laser pulse, t_{ac} can be thought as different pixels in the AOM crystal. The frequency ω can be programmed as the natural frequency of the pulses (non-rotating frame), or shifted to lower frequencies (partial rotating frame), which lowers the required sampling rate and can transfer the signal to a less noisy region in the frequency domain [30, 32]. Moreover, the pulse-shaper can apply arbitrary phases to each pulse so that one can remove artifacts in the signal with phase-cycling. For instance, phase cycling allows us to separate the third order signal we are interested in from a 'transient absorption signal'. The details of phase-cycling and how to generate phase-locked pulses will be explained in Chapter 4.

The pump-pump pulses generated by the pulse-shaper intrinsically have high relative phase stability without requiring additional adaptive optics. We used spectral interferometry to measure the relative phase between the two pump pulses. We measured the spectrum of the pump pulse pair and recovered the relative phase between the pulses for 30 minutes. The delay between the two pulses was kept constant as 400 fs. Figure 2.4 shows the fluctuations of retrieved relative phase over time, which RMS deviation 0.017 rad corresponding to a timing jitter of about 2 attoseconds. This measurement is limited by the signal-to-noise ratio of our spectrometer, and places a lower limit on the phase stability between the pump-pump pulses [34]. As the phase of the acoustic wave for the pulse shaper is locked to the arrival time of the laser pulse in the modulator, the phase of the pump pulse pair is also constant relative to the probe, although we average over all pump probe phases by working in a crossed beam geometry.

Given the phase stability of the pump pulses from our pulse shaper, the

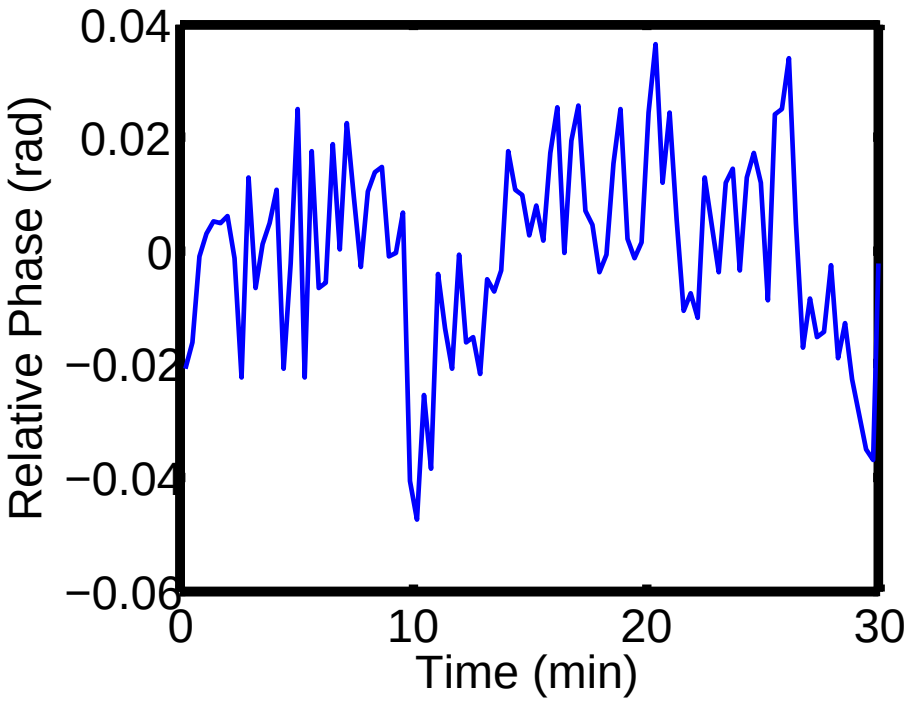

Figure 2.4: Relative phase between pump-pump pulse pair measured over 30 mins.

major sources of noise in the measurement are spectrometer coupling instability, laser intensity fluctuations, spectral instabilities (fluctuations dominated by changes in the center of the spectrum originating from the Kerr lens mode-locked oscillator in our laser system), Rayleigh scattering from the DNA/RNA solutions, and thermal/readout noise from the spectrometer. We implemented three improvements to the apparatus to mitigate these sources of noise. First, we implemented a closed loop proportional-integrative-derivative (PID) control system to improve the beam pointing stability of the pump and probe beams. This improved the stability of the coupling into the spectrometer and reduced the noise in the measurement due to spectrometer coupling by a factor of about 5. We also built a box around the optics to further reduce beam pointing fluctuations due to air currents. However, because it is difficult to asses the improvements due to the box alone, we did not quantize the amount of improvement from putting a box around the laser. In order to correct for laser intensity fluctuations and spectral instabilities, we introduced a third reference beam in the setup, which is a replica of the probe pulse and arrives in

the sample several picoseconds after the pump and probe pulses. An inverted UV Aluminum mirror with fused silica substrate is placed at 45 degrees in the 2^{nd} UV beam. The beam reflected from the front surface acts as the probe beam in the 2D measurement, and the one reflected by the metal coating on the second surface serves as a reference beam. The reference has the same spectrum as the probe and is proportional in energy. The probe and reference then pass through the same optics and their spectra are measured simultaneously with a dual-channel spectrometer behind the sample. Since the reference pulse arrives over 50 picoseconds after the probe, the molecular dynamics are only registered by the probe, while common laser noise present in both spectra can be canceled by dividing the probe by the reference.

The pump pair, probe, and reference pulses are focused into the sample solution by a 500 mm focal length UV-enhanced Aluminum mirror (Edmund Optics). The energy of the pump pulses is between 200 and 500 nJ each. The probe and reference pulses have energies more than an order of magnitude lower than the pump pulses. The focused intensities are difficult to estimate because the mode of the shaped UV beam is structured. However, measurements carried out with a 1000 mm focal length mirror (having a focal intensity 4 times lower than for the 500 mm focal length mirror) show very similar 2D spectra. The adenine and uracil were obtained from Sigma Aldrich and used without further purification. Solutions were prepared with ultra-purified water from purification system Milli-Q (Millipore). The solution absorbance was kept at $1 \sim 1.3$.

In order to improve the sample circulation, we also constructed a flow cell that minimizes artifacts due to the cell windows and the solvent. An important source of systematic error in DNA/RNA 2D spectra is strong linear and nonlinear UV absorption by the solvent and fused silica windows on the sample holder, which can be several times larger than DNA/RNA signal and mask the real DNA dynamics near short pump-probe delays. The excited states lifetimes for DNA/RNA bases in water are on the order of a few hundreds femtoseconds [35], but impurities in the solvent and the fused silica, and two-photon absorption from the solvent also lead to a large non-resonant background signal near zero time delay. Therefore, the 2D spectrum measured from 0 to 120 fs is the sum of DNA/RNA signals plus a significant background

from the windows and solvent. If we suppress the background to some extent, we can still extract pure DNA/RNA data with careful background subtraction. The intuitive solution is to use the highest quality UV grade fused silica (UVFS) and high-performance liquid chromatography (HPLC) water in order to avoid absorption by impurities. After testing out several UVFS windows from different companies, we found that all of the windows we tested absorb in the UV, and the signal modulation depth depends largely on their thickness, so the simplest solution was to use thin UVFS cover slips as windows rather than thick windows with higher quality. Our home-designed flow cell can hold windows of varying thickness. Our measurements were made with the thinnest windows which we could find, and which did not deform during the experiments due to the pressure variations with the peristaltic pump. The window thickness is 160 μm and the cell path length is just under 2 mm.

Chapter 3

Coherent Control Two-Photon Fluorescence Spectroscopy

The goal of coherent control is to prepare molecules in specific quantum states. One approach is the control of interference between multiple quantum pathways via their phases from the initial to the final state which consequently excites one molecular state or molecule over another with shaped pulses [1] (Figure 1.1, left panel). The other approach is to generate different reaction products with pulses that match specific transient Franck Condon windows [5] and transfer the wavepacket in a precise phase of vibrational motion to a new electronic state (Figure 1.1, right panel). Recently, there are increasing applications of coherent control towards cellular imaging. For example, shaping of the spectral phase of an ultrafast laser pulse has been used to enhance image contrast in coherent anti-Stokes Raman scattering microscopy [36]. Coherent control microscopy has also been demonstrated to selectively excite different fluorescent probes and detect the same probe in different pH environments [6–11]. Compared to using a tunable ultrafast laser to separately excite cells/tissues labeled with different fluorophores, coherent control allows selective imaging of fluorophores with a single broadband light source and pseudo-simultaneous imaging of different cells/tissues by switching pulse shapes rapidly. It is especially beneficial for distinguishing broadband fluorophores with similar two-photon absorption cross section, e.g. for NADH, the enzyme-binding induced shifts of the absorption spectrum (up to $\sim$ 10 nm) are small compared to the width of the NADH emission spectrum ($\sim$ 150

nm).

The ideal situation for coherent control is to know the system's Hamiltonian and design the control light field accordingly. However, total Hamiltonian for molecules, even atoms, are complicated to construct, so it is not always feasible to design a pulse shape to enhance a desired product from calculation. One solution to this problem is to use a closed-loop feedback technique with a learning algorithm. The basic idea is to guess a pulse shape, measure how well it controls the system, then modify the pulse shape iteratively until maximum control has been achieved. Details of our closed-loop feedback genetic algorithm(GA) can be found in [19]. At the same time, for some microscopy applications (e.g. to discriminate fluorophores of different absorption spectrum) coherent control can also be achieved with parameter scans which probe the system with adjustable parameters, e.g. adding linear chirp in the time domain to optimize population transfer [37], or applying phase jump at half of the resonance frequency to enhance TPA probability [3]. In the following sections, we will explain how we selectively excite individual fluorescent proteins and endogenous compounds with parameter scan methods.

3.1 Time-Dependent Perturbation Theory

In order to understand why the best shape of laser pulse can maximize or suppress the yield of a certain chemical product, we start with the time-dependent perturbation theory for a molecule-field interaction system with Hamiltonian $H = H_0 + V(t)$, where H_0 represents the field-free Hamiltonian and satisfies the equation for the eigenstates $\{|n\rangle\}$ and eigenenergies E_n

$$H_0|n\rangle = E_n|n\rangle = \hbar\omega_n|n\rangle \tag{3.1}$$

$V(t) = -\mu \cdot \tilde{\mathbf{E}}(t)$ is the interaction Hamiltonian, where $\mu = e\mathbf{r}$ is the electric dipole moment operator. For a linearly-polarized light with electric field $\epsilon(t)$, the matrix element of $V(t)$ in the eigenstate basis is

$$V_{ij}(t) = \mu_{ij}(\epsilon(t) + c.c.) \tag{3.2}$$

If we define the initial state ket $|i\rangle$ of a physical system at $t = 0$ for $t_0 = 0$as

$$|i\rangle = |\psi, t_0 = 0; t = t_0\rangle = \sum_n C_n(0)|n\rangle \tag{3.3}$$

and at t > 0, $C_n(t)$ is time-dependent and satisfies

$$|\psi, t_0 = 0; t\rangle = \sum_n C_n(t)e^{-iE_nt/\hbar}|n\rangle \tag{3.4}$$

If there is no external interaction (i.e. $V(t) = 0$), the state ket will simply be $|\psi, t_0 = 0; t\rangle = \sum_n C_n(0)e^{-iE_nt/\hbar}|n\rangle$. $C_n(t)$ will change with time only in the presence of $V(t)$, so it is natural to solve Eq. 3.4 in the Interaction picture, where the evolution of the state ket is determined by $V_I(t)$.

3.1.1 Interaction picture

Suppose we have a system with initial state ket $|\psi, t_0 = 0; t = t_0\rangle$, at a later time, we denote the state ket in the Schrödinger's picture as $|\psi, t_0; t\rangle_S$, where the subscript S refers to a state ket in the Schrödinger picture. Then we define the state ket and the interaction Hamiltonian in the interaction picture as

$$\begin{aligned} |\psi, t_0; t\rangle_I &\equiv U_0^\dagger(t, t_0 = 0)|\psi, t_0; t\rangle_S \\ &\equiv e^{iH_0t/\hbar}|\psi, t_0; t\rangle_S \\ V_I &\equiv U_0^\dagger(t, t_0 = 0)V_S U_0(t, t_0 = 0) = e^{iH_0t/\hbar}V_S e^{-iH_0t/\hbar} \end{aligned} \tag{3.5}$$

where the subscript "I" refers to a state ket or an operator in the Interaction picture, and $U_0(t, t_0 = 0) = e^{-iH_0t/\hbar}$ is the time evolution operator with respect to the Hamiltonian H_0. Combining Eq. 3.4 and 3.5, there is a simple representation of $|\psi, t_0; t\rangle_I$ in $C_n(t)$

$$\begin{aligned} |\psi, t_0; t\rangle_I &= e^{iH_0t/\hbar}|\psi, t_0; t\rangle_S = e^{iH_0t/\hbar}\sum_n C_n(t)e^{-iE_nt/\hbar}|n\rangle \\ &= \sum_n C_n(t)|n\rangle \end{aligned} \tag{3.6}$$

where $C_n(t) = \langle n|\psi, t_0; t\rangle_I$ since $\langle n|\sum_{n'} C'_n(t)|n'\rangle = \sum_{n'} C'_n(t)\delta_{n,n'}$

So how does $C_n(t)$ evolve with time? We start by differentiating both sides of Eq. 3.5

$$\begin{aligned} i\hbar\frac{\partial}{\partial t}|\psi,t_0;t\rangle_I &= i\hbar\frac{\partial}{\partial t}(e^{iH_0t/\hbar}|\psi,t_0;t\rangle_S) \\ &= i\hbar[\frac{iH_0}{\hbar}e^{iH_0t/\hbar}|\psi,t_0;t\rangle_S + e^{iH_0t/\hbar}(H_0+V_S(t))|\psi,t_0;t\rangle_S] \\ &= \left(e^{iH_0t/\hbar}V_S(t)e^{-iH_0t/\hbar}\right)e^{iH_0t/\hbar}|\psi,t_0;t\rangle_S \\ &= V_I(t)|\psi,t_0;t\rangle_I \end{aligned} \tag{3.7}$$

then multiply Eq. 3.7 by $\langle n|$ from the left and use results from Eq. 3.6,we obtain

$$\begin{aligned} i\hbar\frac{\partial}{\partial t}C_n(t) &= i\hbar\frac{\partial}{\partial t}\langle n|\psi,t_0;t\rangle_I \\ &= \sum_m \langle n|V_I(t)|m\rangle\langle m|\psi,t_0;t\rangle_I \\ &= \sum_m \langle n|e^{iH_0t/\hbar}V_S(t)e^{-iH_0t/\hbar}|m\rangle C_m(t) \\ &= \sum_m V_{nm}e^{i(E_n-E_m)t/\hbar}C_m(t) = \sum_m V_{nm}e^{i\omega_{nm}t/\hbar}C_m(t) \end{aligned} \tag{3.8}$$

where $V_{nm}(t)$ is the matrix element for the external interaction Hamiltonian, and $\omega_{nm} \equiv \omega_n - \omega_m = (E_n - E_m)/\hbar$. For most of the systems exposed to an electromagnetic field, the above equation cannot be solved exactly. Oftentimes, in the weak field limit, we can find a solution by time-dependent perturbation [38, 39]. From Eq. 3.7, the state ket in the interaction picture can be expressed as:

$$\begin{aligned} |\psi_I(t)\rangle = |\psi_I(t_0)\rangle + \sum_{n=1}^{\infty}\left(\frac{-i}{\hbar}\right)^n \int_{t_0}^{t} d\tau_n \int_{t_0}^{\tau_n} d\tau_{n-1}\ldots\int_{t_0}^{\tau_2} d\tau_1 \\ V_I(\tau_n)V_I(\tau_{n-1})\ldots V_I(\tau_1)|\psi_I(t_0)\rangle \end{aligned} \tag{3.9}$$

And the different orders of transitions amplitude $C_n(t)$ can be expressed as

$$\begin{aligned}
C_n^{(0)}(t) &= \sum_i \delta_{ni} \\
C_n^{(1)}(t) &= \frac{-i}{\hbar}\sum_m \int_{t_0}^{t} V_{nm}(t')e^{i\omega_{nm}t'}dt' C_m^{(0)}(t') = \frac{-i}{\hbar}\sum_m \int_{t_0}^{t} V_{nm}(t')e^{i\omega_{nm}t'}dt'\delta_{mi} \\
&= \frac{-i}{\hbar}\int_{t_0}^{t} V_{ni}(t')e^{i\omega_{ni}t'}dt' \\
C_n^{(2)}(t) &= \left(\frac{-i}{\hbar}\right)^2 \sum_m \int_{t_0}^{t} V_{nm}(t')e^{i\omega_{nm}t'}dt' C_m^{(1)}(t) \\
&= \left(\frac{-i}{\hbar}\right)^2 \sum_m \int_{t_0}^{t} V_{nm}(t')e^{i\omega_{nm}t'}dt' \left(\int_{t_0}^{t'} V_{mi}(t'')e^{i\omega_{mi}t''}dt''\right) \\
&\vdots
\end{aligned} \tag{3.10}$$

3.1.2 Two level systems in electric fields

For resonant interaction of a weak laser pulse with a two-level system, assuming the atom is initially in the ground state $|g\rangle$, and $t_0 = -\infty$ first-order-time-dependent perturbation predicts the amplitude of the excited state $|f\rangle$ equals

$$\begin{aligned}
C_f^{(1)}(t) &= \frac{-i}{\hbar}\int_{-\infty}^{t} \mu_{ij}\epsilon(t')e^{-i\omega_{fg}t'}dt' \\
&= \frac{-i}{\hbar}\int_{-\infty}^{t} \mu_{ij}\left(\int_{-\infty}^{\infty} \tilde{\epsilon}(\omega)e^{-i(\omega+\omega_{fg})t'}d\omega\right)dt'
\end{aligned} \tag{3.11}$$

where $\tilde{\epsilon}(\omega)$ is the Fourier transform of $\epsilon(t)$. At times after the excitation pulse duration, t$\rightarrow \infty$, the transition amplitude is then

$$C_f^{(1)}(t) = \frac{-i}{\hbar}\mu_{ij}\tilde{\epsilon}(\omega - \omega_{fg}) \tag{3.12}$$

which largely depends on the energy content of the excitation pulse spectrum resonant with transition, and neither the amplitudes or the phases of the other spectral components have any effect to the transition possibility. The equation for the transition amplitude becomes more interesting as we consider higher order perturbation theory.

3.1.3 Multiphoton transitions in weak fields

Even if the pulse is not resonant with any one-photon transition, there is still finite possibility for the system to absorb multiple photons within a short period of time if the pulse intensity is high enough - this phenomenon is called multiphoton transition. As we will show in the following, the relative phase of the different frequencies in the field is extremely important for multiphoton transitions. We first consider a two-photon transition with no intermediate resonances and apply rotating wave approximation (RWA) to the 2nd order perturbation theory. The amplitude to the final state $|f\rangle$ can be expressed as:

$$C_f^{(2)}(t) = \left(\frac{-i}{\hbar}\right)^2 \sum_m \mu_{fm}\mu_{mg} \int_{-\infty}^{t} \int_{-\infty}^{t'} \epsilon(t')\epsilon(t'') e^{i(\omega_f - \omega_m)t'} e^{i(\omega_m - \omega_g)t''} dt' dt'' \tag{3.13}$$

where $|g\rangle$ is the ground state, and $|m\rangle$ are the possible intermediate states. Since we assume ultrafast pulse excitation and all states are far from resonance, the contribution of all intermediate levels adds up coherently only for a short duration, and we can thus approximate the summation over all intermediate states as [3]

$$\sum_m \mu_{fm}\mu_{mg} e^{i\omega_m(t''-t')} \approx \begin{cases} \langle f|(\mu)^2|g\rangle & |t_1 - t_2| < \frac{1}{\bar{\omega}} \\ 0 & |t_1 - t_2| \geq \frac{1}{\bar{\omega}} \end{cases} \tag{3.14}$$

where $\langle f|(\mu)^2|g\rangle$ is the effective two photon coupling, and $\hbar\bar{\omega}$ is the weighted average energy where all the possible intermediate states are taken into considerations [40]. Combining Eq. 3.13 and Eq. 3.14, the two-photon absorption (TPA) probability becomes

$$\begin{aligned} P_{g\to f}^{TPA} &\equiv \left|C_f^{(2)}(t=\infty)\right|^2 \\ &= \frac{1}{(\hbar)^4} \left|\frac{\langle f|(\mu)^2|g\rangle}{\bar{\omega}}\right|^2 \left|\int_{-\infty}^{\infty} \epsilon^2(t) e^{i\omega_{fg}t} dt\right|^2 \end{aligned} \tag{3.15}$$

where $\hbar\omega_{fg}$ is the transition energy from the ground ($|g\rangle$) to the final ($|f\rangle$) state. The TPA probability is in proportional to the two-photon power spectrum

$$\mathcal{F}\left(\epsilon^2(t)\right) = \int_{-\infty}^{\infty} \epsilon^2(t) e^{i\omega_{fg}t} dt \tag{3.16}$$

This result can easily be generalized to an N^{th} order process, where the probability for N-photon transition to the excited state is proportional to the Fourier component of $\epsilon^N(t)$ [3] at the excited-ground state energy difference divided by $\hbar$. In contrast to a single-photon transition, all frequency components of the pulse may contribute to the multiphoton transition with their relative phases playing important roles. We will use the case of TPA to explain this idea more explicitly.

3.1.4 Control the TPA probability with a pulse with a π phase jump in the spectrum

In the frequency domain, the transition probability for TPA, Eq. 3.15 can be rewritten as

$$\begin{aligned} P_{g\to f}^{TPA} &\propto \left| \int_{-\infty}^{\infty} \epsilon(t) e^{i(\omega_{fg}/2+\omega)t} \epsilon(t) e^{i(\omega_{fg}/2-\omega)t} dt \right|^2 \\ &= \left| \int_{-\infty}^{\infty} \tilde{\epsilon}(\omega_{fg}/2+\omega)\tilde{\epsilon}(\omega_{fg}/2-\omega) d\omega \right|^2 \\ &= \left| \int_{-\infty}^{\infty} A(\omega_{fg}/2+\omega) e^{i\Phi(\omega_{fg}/2+\omega)} A(\omega_{fg}/2-\omega) e^{i\Phi(\omega_{fg}/2-\omega)} d\omega \right|^2 \end{aligned} \tag{3.17}$$

where $\tilde{\epsilon}(\omega) = A(\omega)e^{\Phi(\omega)}$ is the Fourier transform of $\epsilon(t)$. $A(\omega)$ and $\Phi(\omega)$ are the spectral amplitude and phase respectively. Unlike for a single photon transition, in the case of multi-photon transition, both the amplitude and phase of the excitation pulses affect the transition amplitudes. From Eq. 3.17, the transition probability can be interpreted as a coherent sum over photon pairs that fulfill the resonance condition $(\omega_{fg}/2+\omega)+(\omega_{fg}/2-\omega)=\omega_{fg}$ for $\Omega = \omega_{fg}/2 \pm \omega$ within the spectrum of the excitation pulse. The two-photon transition probability can therefore be controlled by tailoring the amplitude and phase of a single pulse. For a given power spectrum, the TPA transition probability $P_{g\to f}^{TPA}$ is maximized when the spectral phase of the integrand is a constant. The most obvious solution is a transform-limited pulse with $\Omega = 0$ across the excitation spectrum, which is consistent with the intuition that shorter pulses with higher peak intensities enhance TPA probability. One of the other possible solutions are pulses with antisymmetric spectral phase

distribution around the two-photon transition frequency $\omega_{fg}/2$, i.e. $\Phi(\omega_{fg}/2+\omega) = -\Phi(\omega_{fg}/2-\omega)$, where the phase for the two terms in Eq. 3.17 cancel each other.

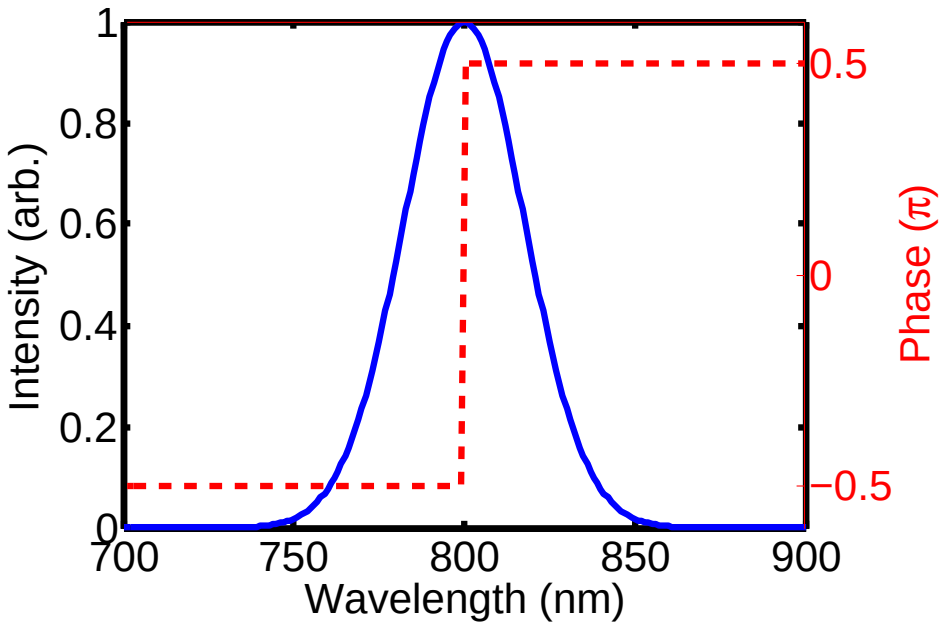

Figure 3.1: Intensity and phase of a pulse with a π phase jump.

As stated above, the TPA transition probability of a system reaches a maximum when it is illuminated by transform-limited pulses, or by pulses with a π phase jump (Figure 3.1) at the half of the transition frequency, where $\Phi(\omega_{fg}/2-\omega) = -\pi/2$, $\Phi(\omega_{fg}/2+\omega) = \pi/2$.

So how does a π-phase step affect the pulse shape in the time domain? Figure 3.2 shows second harmonic generation frequency-resolved optical gating (SHG-FROG) plots for an unshaped pulse (left panel) and for a pulse with a π phase step in the center of the spectrum (middle panel). The π phase step in the spectrum stretches a nearly transform-limited 30 fs pulse to $100 \sim 200$ fs duration. It might seem counterintuitive that a pulse spreading in time (as long as it is less than the excited state lifetime) can drive TPA transitions as efficiently as a short transform-limited pulse. This result can be understood by considering the second-order power spectrum of the pulse, or the Fourier transform of the square of the electric field in time: $\mathcal{F}\left(E^2\left(t\right)\right)$. In the weak field limit, the two-photon transition probability can be estimated as

the product of the two-photon action cross section and the second-order power spectrum of the excitation pulse. The right panel in Figure 3.2 indicates that the second-order power spectrum has a spike with the same spectral density as a transform-limited pulse at frequency twice the π-phase jump position. For a narrow absorption lineshape characteristic of an atomic system, because the TPA amplitude is only determined by the second-order power spectrum near resonance, both a transform-limited pulse and a pulse with a π phase step at half the resonance frequency can induce equal amount of transitions. On the other hand, for a broad inhomogeneous TPA spectrum of a molecular system, the transition probability is proportional to a sum of many individual transitions [3].

$$P^{TPA} \propto \int_{-\infty}^{\infty} g(\omega_{fg}) \left| \int_{-\infty}^{\infty} \epsilon^2(t) e^{i\omega_{fg}t} dt \right|^2 d\omega_{fg} \tag{3.18}$$

where $g(\omega_{fg})$ is the molecular TPA lineshape. Assuming $g(\omega_{fg})$ is much wider than the excitation spectrum, P^{TPA} becomes

$$\begin{aligned} P^{TPA} &\propto \int_{-\infty}^{\infty}\int_{-\infty}^{\infty}\int_{-\infty}^{\infty} \epsilon^2(t_1) e^{i\omega_{fg}t_1}\ \epsilon^{*2}(t_2) e^{-i\omega_{fg}t_2} dt_1 dt_2 d\omega_{fg} \\ &= \int_{-\infty}^{\infty}\int_{-\infty}^{\infty}\int_{-\infty}^{\infty} \epsilon^2(t_1)\epsilon^{*2}(t_2) e^{i\omega_{fg}(t_1-t_2)} dt_1 dt_2 d\omega_{fg} \\ &= \int_{-\infty}^{\infty}\int_{-\infty}^{\infty} \epsilon^2(t_1)\epsilon^{*2}(t_2) dt_1 dt_2 \delta(t_1-t_2) \\ &= \int_{-\infty}^{\infty} \epsilon^2(t_1)\epsilon^{*2}(t_1) dt_1 \\ &= \int_{-\infty}^{\infty} I^2(t) dt \end{aligned} \tag{3.19}$$

which is consistent with the expectation that the multiphoton transition probability for a molecule with a broad inhomogeneous absorption line depends only on the excitation intensity and not its phase.

We found that data from free and enzyme-bound NADH lie between the two extremes. Both forms of NADH have TPA spectrum wider than 150 nm [41], with their two-photon fluorescence maximized when they are illuminated by transform-limited pulses, and slightly different response curves to π phase step pulses between these two forms imply that a ratio of the signals can easily

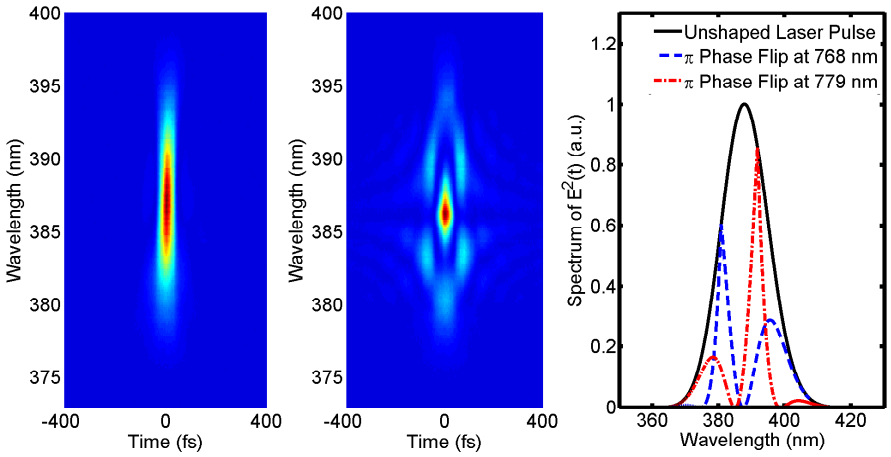

Figure 3.2: SHG-FROG plots showing both an unshaped pulse (left panel) and a shaped pulse with π phase step in the middle of the spectral bandwidth (middle panel). The right panel shows the second-order power spectrum, or the Fourier transform of the square of the electric field in time, for an unshaped pulse and two π phase step pulses that are representative of the control pulses used in Figure 3.4

distinguish them. Our goal is to discriminate between samples containing either free NADH or enzyme-bound NADH solutions with a π phase jump at a given frequency within the excitation bandwidth, leaving the spectral amplitudes unchanged.

3.2 Distinguishing between different states of NADH

3.2.1 NADH as an intrinsic fluorophore

The electron transport chain is the most efficient way of energy production in cells. The electron transport chain produces energy in the form of Adenosine-5'-triphosphate (ATP) by transferring electrons to molecular oxygen. The metabolic coenzymes flavin adenine dinucleotide (FAD) and NADH are the primary electron acceptor and donor, respectively, in oxidative phosphorylation. The fluorescence of reduced NADH has been a useful non-invasive tool for studying cellular energy metabolism [42–45]. Traditionally, metabolic dy-

namics have been characterized by the total NADH concentration, however, the reaction velocity of intracellular NADH-linked dehydrogenase depends on the local concentration of free NADH [46]. As a result, there is increasing research dedicated to identify intracellular free NADH concentrations. Three major techiniques to deteremine free NADH conctrations are: calibrated spectrofluorometry, time-resolved fluorescence and anisotropy decays [47, 48], and the fluorescence lifetime measurement [47, 49].

As there is fluorescence enhancement in enzyme-bound NADH, accompanied with shifts in the emission peak, calibrated spectrofluorometry can be used to determine the free/bound NADH concentrations. Figure 3.3 shows the single photon absorption and emission spectrum of pure NADH and mitochondrial malate dehydrogenase (mMDH)-bound NADH. On the left panel, the absorption peak shifts from 340 nm to 348 nm for 37% bound NADH (NADH 27 μM + MDH 13 μM). On the right panel, the emission peak slightly shifts to the blue for 63% bound NADH (NADH 27 μM + MDH 25 μM), and its the fluorescence yield is four times more than that for pure NADH. Time-

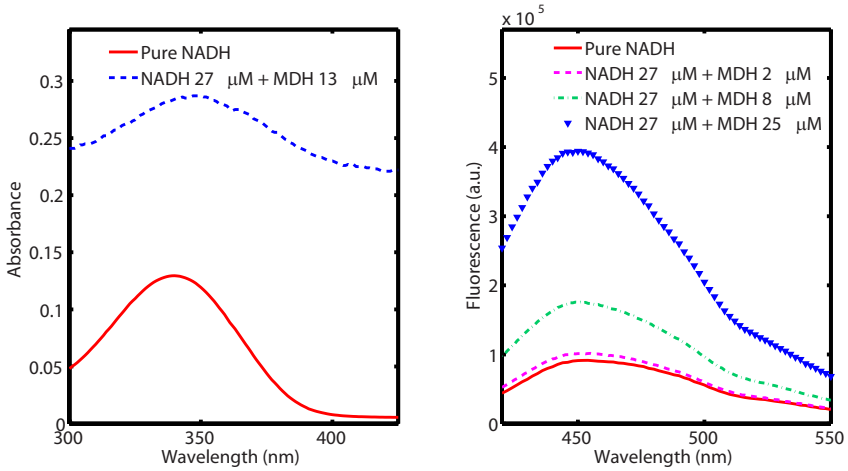

Figure 3.3: Left panel: one-photon absorption spectrum of NADH and NADH plus mMDH. Right panel: one-photon fluorescence spectrum of NADH and NADH plus mMDH at various concentrations measured by a spectrofluorometer. The excitation wavelength was 385 nm.

resolved fluorescence and anisotropy decays [47, 48] also provide information to the excited state dynamics and rotational mobility of NADH. The fluorescence lifetime measurement, which probes the decay time of the excited

state, is sensitive to fluorophore micro-environment, and provides a method for discriminating free and enzyme-bound components. The anisotropy of the fluorescence measures its parallel and perpendicular components relative to the excitation polarization and reveals the angle between the excitation and emission dipoles. The change of the net molecular orientation due to rotational diffusive motion results in the decay of anisotropy. The characteristic decay time, known as the rotational diffusion time, characterizes the timescale of this diffusive motion. As there is a significant increment in the size of enzyme-bound NADH, binding of NADH leads to a large increase (> 10 times) in the anisotropy decay time.

The above three techniques, however, have their own drawbacks that make them less appealing to microscopy. To perform calibrated spectrofluorometry, one has to cleverly couple dim scattering fluorescence into a tiny spectrometer slit ($\sim$ 10 μm) to spectrally resolve the fluorescence, not to mention possible UV damage and the extra post-processing time to analyze the spectrum shift. By the same token, time-resolved fluorescence measurements need to record low-level light signals with picosecond time resolution that requires extra time-correlated single-photon counting instruments and detail fittings for the decay function. For the anisotropy measurements, additional optics to measure fluorescence along different polarization and post-processing are also essential. Most important of all, as there are seven different cellular dehydrogenases that are known to bind NADH in glucose metabolism alone, with each of them haviing its own specific effect on the NADH steady state and time-resolved properties, it would be hard to determine the free NADH concentration from a signal that is a sum of various decays and different amounts of spectral shifts. To get around these problem, we use coherent control spectroscopy to discriminate free and enzyme-bound NADH. We can rapidly determine the state of NADH without measuring the spectrum or fluorescence decay time by illuminating the sample with different pulse shapes in succession. As mentioned above, there are multiple enzymes that can bind NADH, here we have selected free vs. mMDH-bound NADH as an example for coherent control 2PF spectroscopy.

3.2.2 π scans on NADH

Figure 3.4 shows the normalized two-photon fluorescence as a function of π phase step position for the pure NADH solution and for NADH+MDH mixture. Details of the sample preparation are described in Appendix A. The left and right panels in Figure 3.4 correspond to data taken in two different runs. Even though the detailed shape of the π scan traces can vary from day to day, the main discrimination feature remains. The primary feature in the π scan traces for both the free and enzyme-bound NADH is the "double-minimum" whose relative depth systematically changes with the enzyme binding fraction. In the left panel, the dip positions are at 767 and 787 nm (laser spectrum centered at 778 nm), while in the right panel the positions are 768 and 779 nm (laser spectrum at 775 nm). In both cases, the short-wavelength minimum becomes less pronounced with higher MDH concentration. A natural choice of two pulse shapes to selectively excite free or bound NADH would be the pulse shape with the spectral phase jump located at each of the two minima in the π phase scan. As shown in Figure 3.5, the relative strength between the short-wavelength and long-wavelength minima raises with increasing binding fraction. The inset shows the dip ratio vs. enzyme concentration for measurements performed on different days, where the monotonic increase in the ratio is consistent over separate measurements. This parameter scan is sensitive to as low as 3% of binding, with the sensitivity largely depends on the amount signal averaging one can afford to perform. One possible explanation to the day to day variations in the π scan traces is that the π scan curves are sensitive to pulse chirp and the exact chirp value depends on the positioning of the cell with respect to the PMT.

To understand why π scan curves vary from day to day, we illuminated pure NADH solution with transform-limited and chirped pulses and recorded its 2PF as a function of π step position. The red curve in Figure 3.6 shows laser pulse duration vs. the second compressor position of our chirped pulse amplifier system. The pulse duration reaches a minimum ($\sim$ 30 fs) when it is compressed and exceeds 100 fs when either positive or negative chirp has been introduced to the pulse. The depth of the double-minima either increases (third blue curve from right) or degenerates to a single peak (fifth blue curve from right) when the pulse is lengthened from 30 fs to 70 fs. The π scan

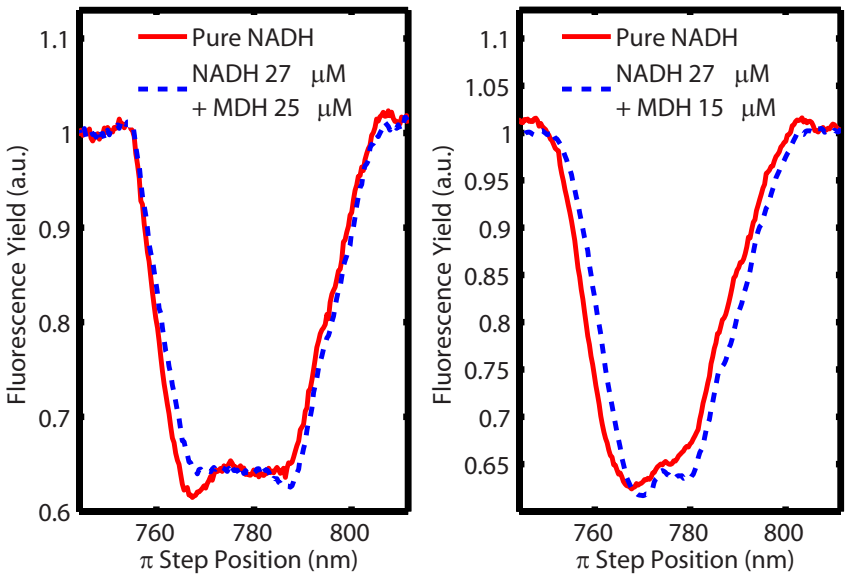

Figure 3.4: Normalized fluorescence as a function of π step position for pure NADH (solid red) and mMDH-bound NADH (dashed blue) solutions. The left and right panels are measurement from different days. Even though the details of the curves vary from day to day, the main discrimination feature remains, that the dip at the longer wavelength becomes more prominent as the binding ratio increases.

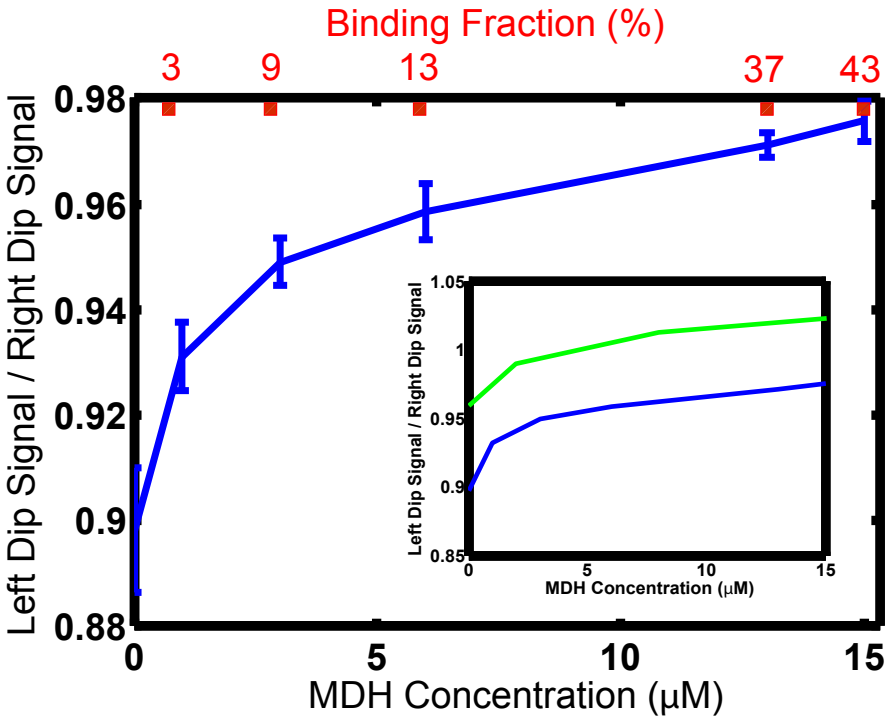

Figure 3.5: Ratio of the fluorescence signal at the short-wavelength minimum to that at the long-wavelength minimum vs. mMDH concentration. The binding fraction is shown on the top of the graph. The error bars show the standard deviation of the mean for repeated measurements. The inset shows the dip ratio vs. enzyme concentration for data take on different days (blue and green curves). The two curves have the same shape but are level-shifted. The absolute dip ratio changes from day to day because of different chirp in the excitation laser pulse, but the relative change in the dip ratio vs. enzyme concentration is preserved.

traces for NADH solution changes from "double-minima" (bottom blue curve) to more structured curves when the excitation pulses are stretched to 200 fs. Since we are imaging fluorescence from a thick sample (path length 10 mm), the pulse undergoes moderate dispersion within the sample, and a perfectly transform-limited pulse is not preserved. A 35 fs long laser pulse at wavelength 800 nm will be stretched to 50 fs long after going through a 10 cm thick glass. The dispersion caused by the same thickness of water will be slightly smaller. Depending on where we place the PMT with respect to the cuvette, we are collecting 2PF from different segment of the NADH solution which experiences pulses of different amount of chirp. However, as illustrated in the inset of Figure 3.5, the control was not affected by these day-to-day changes. As long as the excitation pluse is nearlly transform-limited, the ratio between the two dips always changes monotonically with NADH-enzyme binding ratio.

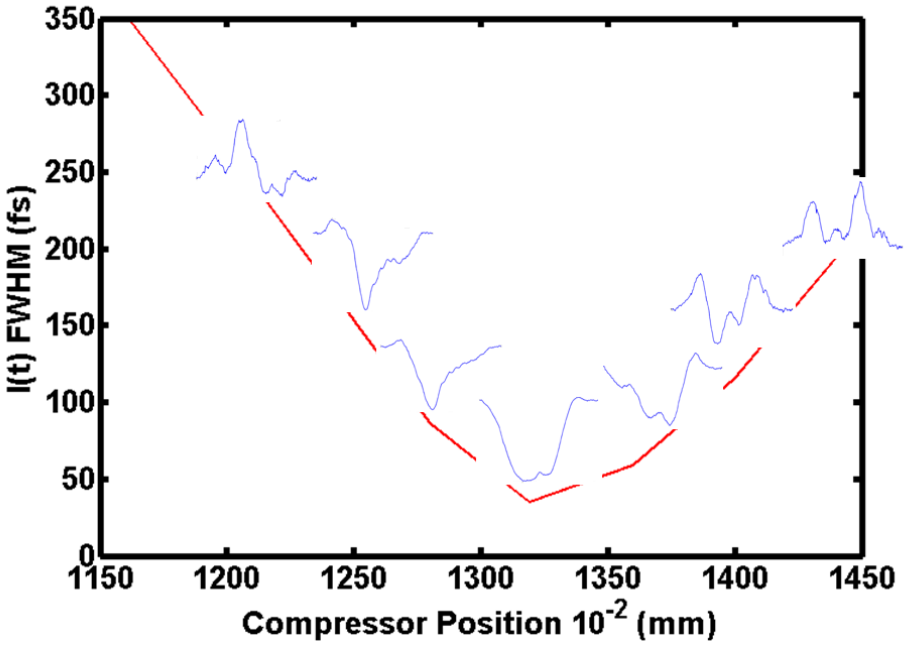

Figure 3.6: π scan traces vs. chirp for pure NADH. The red curve indicates the pulse duration of chirped pulses. The blue curves are the corresponding π scan data for a pure NADH solution. The double-minima feature in the π scan curve became more structured as extra chirp was added to a transform limited pulse.

Another way to highlight the selective excitation of different forms of NADH with shaped pulses is to examine the histogram distributions for fluorescence ratio between two pulse shapes (fluorescence by excitation pulse with a π phase step at the longer-wavelength dip / fluorescence by excitation pulse with a π phase step at the shorter-wavelength dip) for both free (Figure 3.7, shaded pink) and enzyme-bound (solid blue) NADH. Each histogram depicts the number of measurements recorded that resulted in a given ratio of fluorescence for the two pulse shapes located at each of the two minima in the π phase scan. The peaks were constructed from 100 measurements, with 500 laser shots in each measurement. While this measurement took 50 seconds to complete with our 1 kHz amplifier, a similar measurement with a high repetition rate laser (e.g. our Ti:Sapphire oscillator with a repetition rate of 88 MHz) would take less than 0.6 s. We noted that the absolute dip ratio can change from day to day as shown in the inset of Figure 3.5, however, for a given laser spectrum, the ratio only depends on the MDH concentration. The histogram peaks are well separated by more than 3σ, indicating that the two pulse shapes can efficiently discriminate between the two forms of NADH in the presence of laser and sample fluctuations.

To further demonstrate the π phase scan technique is sensitive to the NADH-enzyme binding ratio, we ran π-scan measurements on NADH solutions at different temperatures. Like all chemical reactions, the NADH-enzyme binding ratio is sensitive to the change in temperature. It decreases at higher temperature. Figure 3.8 shows the π scan traces for NADH solution taken at room temperature and at 40 °C. The left panel is data for NADH-MDH mixture, and the right panel is for pure NADH solution. We started from measurement at room temperature (blue curve), and slowly warmed up the solution temperature by water bath. At 40 °C, the dip at longer wavelength becomes slightly less prominent for the mixture (red dots), which indicates less binding. As we cooled down the solution back to room temperature, the dip depth almost recovered back to the earlier value (green dashed), which suggests that the binding/un-binding process induced by the change in temperature is reversible. The right panel of Figure 3.8 shows the blank measurements on pure NADH solution. The shape of the π scan traces is independent of temperature. From these two measurements, we conclude that the π phase scan

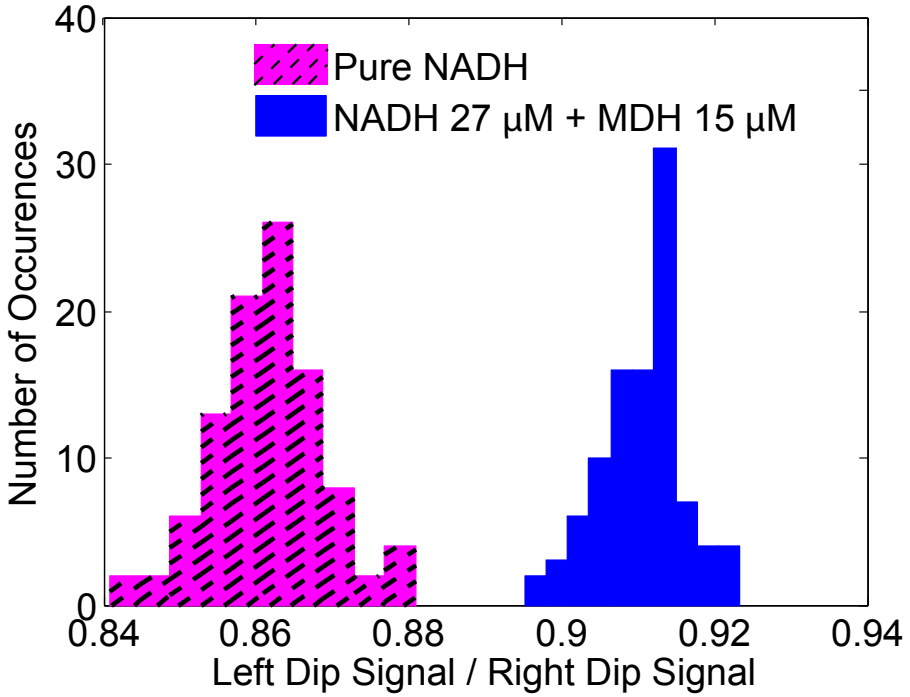

Figure 3.7: Histogram distributions for fluorescence ratio between two pulse shapes for both free (shaded pink) and enzyme-bound (solid blue) NADH.

technique can detect minuscule variations in the binding ratio caused by temperature fluctuations, and it is not because of damage of NADH at higher temperature.

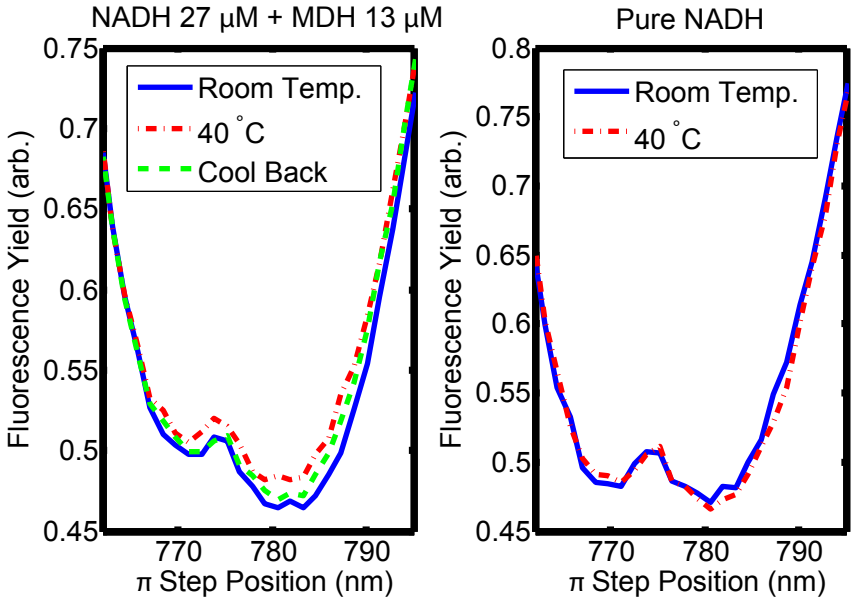

Figure 3.8: π scan traces vs. temperature for NADH solutions. Left panel: blue curve: π scan traces for NADH-MDH mixture at room temperature; red dots: at 40 °C; green dash: cool back to room temperature. Right panel: blue curve: π scan traces for pure NADH solution at room temperature; red dots: at 40 °C. The dip at longer wavelength becomes less pronounced when the NADH+MDH mixture is warmed up, indicating less binding, while the shape of the traces for pure NADH solution at different temperature remain the same.

The coherent control with shaped pulse techinique is therefore, useful for discrimination-based microscopy as one can selectively excite different fluorophores by switching bewteen different pulse shapes. It is especially beneficial for functional microscopy that wants to follow molecular function in real time, because the coherent control approach allows discrimination between fluorophores with only a few shaped laser shots and doesn't require complicated analysis instrument or optics, or tuning the laser wavelength. Here we have demostrated the concept of coherent control two-photon spectroscopy achieved by pulse shape parameterizations on two forms of NADH, the same idea can be generalized to other 2PF systems, and a closed-loop feedback control approach should allow even wider application.

Chapter 4

2D Spectroscopy in the Deep UV

Traditional linear optical spectroscopy measures the emission and absorption spectrum of molecular systems. For molecules in condensed media, inhomogeneous broadening effect due to a variation of the local environment often dominates the linear line shapes and makes it difficult to extract structural information and molecular dynamics from the measurement. Nonlinear optical spectroscopy techniques, e.g. photon echoes (PEs), hole burning, and phase-locked pump-probe (PLPP) absorption, are used to selectively eliminate inhomogeneous broadening. Because these techniques measure third-order molecular response as a function of time delay between the three pulses in the case of PEs and PLPP or the frequencies of the two excitation pulses in the case of hole burning, they are in general referred to as 2D spectroscopy. As mentioned briefly in Chapter 2, 2D electronic and vibrational spectroscopy has been widely used to study molecular structures and energy transfer, and there is an increasing interest in understanding DNA excited state relaxation dynamics with 2D UV spectroscopy. In this chapter we will first introduce the theory of 2D spectroscopy and compare different methods for collecting 2D spectra. Then we review earlier studies on the ultrafast non-radiative decay routes for UV-excited monomeric DNA bases using two other UV femtosecond laser spectroscopic techniques- transient absorption (TA) and fluorescence up-conversion (FU). Finally, we compare 2D UV spectrum of adenine and uracil in solution, while both molecules show excited state absorption (ESA) for short

times (< 100 fs), and ground state bleach (GSB) extending for long times (> 1 ps), uracil shows an evolution of the 2D spectrum on a $100 - 300$ fs timescale, which adenine does not. We interpret this difference between adenine and uracil in terms of the slope of the excited state potential energy surface near the Frank Condon (FC) region [50–62].

4.1 Theory

In Chapter 3, we have explained two-photon absorption probability with time-dependent perturbation theory in Hilbert space using wavefunctions, in this chapter, we introduce the density matrix and further generalize time-dependent perturbation theory to higher order process [63]. The density operator can be used to describe ensemble averages through a mixed state and to construct a description of linear and nonlinear optical spectroscopy that maintains the time orderings of various interactions.

4.1.1 Density operator

An ensemble which can be characterized by a wavefunction $|\psi\rangle$ is said to be a pure state. According to the postulates of quantum mechanics, the system is then completely defined. The expectation value of any operator A is given by:

$$\langle A(t)\rangle = \langle\psi(t)|A|\psi(t)\rangle \tag{4.1}$$

If $|\psi(t)\rangle$ is represented with a set of eigenstates $\{|n\rangle\}$, $|\psi(t)\rangle = \sum_n C_n(t)|n\rangle$, Eq. 4.1 becomes:

$$\langle A(t)\rangle = \sum_{n,m} C_n(t)C_m^*(t)\langle m|A|n\rangle \equiv \sum_{n,m} C_n(t)C_m^*(t)A_{mn} \tag{4.2}$$

Here we introduce the density operator formalism, proposed by J. von Neumann in 1927, where

$$\begin{aligned} \rho &\equiv |\psi(t)\rangle\langle\psi(t)| = \sum_{n,m} C_n(t)C_m^*(t)|n\rangle\langle m| \equiv \sum_{n,m} \rho_{nm}(t)|n\rangle\langle m| \\ \rho_{nm}(t) &\equiv C_n(t)C_m^*(t) \end{aligned} \tag{4.3}$$

Eq. 4.2 thus can be written as:

$$\langle A(t)\rangle = \sum_{n,m} A_{mn}\rho_{nm}(t) \equiv \mathrm{Tr}[A\rho(t)] \tag{4.4}$$

the expectation of an operator can be expressed simply as the trace of product of the operator and the density matrix. In most cases, however, a general state of a quantum system may not be pure, and the precise state of the system is unknown. The density matrix formalism can be used to describe the system in the statistical sense. Consider an ensemble of systems with a given probability P_k to be in the quantum state $|\psi_k(t)\rangle$. The corresponding density operator is defined by

$$\rho \equiv \sum_k P_k |\psi_k(t)\rangle\langle\psi_k(t)| \tag{4.5}$$

where the fractional populations satisfy the normalization condition

$$\sum_k P_k = 1 \tag{4.6}$$

Suppose we make a measurement on the ensemble of an observable A, the ensemble average of A naturally becomes

$$\overline{\langle A(t)\rangle} = \sum_k P_k \sum_{n,m} C_n^k(t) C_m^{k*}(t) A_{mn} \tag{4.7}$$

4.1.2 Perturbation expansion

So how does the density operator ρ evolve with time? In Chapter 3, we introduced time-dependent perturbation theory to solve the Schrödinger equation for wavefunctions, where

$$|\psi_I(t)\rangle = |\psi_I(t_0)\rangle + \sum_{n=1}^{\infty} \left(\frac{-i}{\hbar}\right)^n \int_{t_0}^{t} d\tau_n \int_{t_0}^{\tau_n} d\tau_{n-1} \ldots \int_{t_0}^{\tau_2} d\tau_1 \\ V_I(\tau_n) V_I(\tau_{n-1}) \ldots V_I(\tau_1) |\psi_I(t_0)\rangle \tag{4.8}$$

Similarly, we can define the density matrix in the interaction picture:

$$\begin{aligned}\rho_I(t) &= |\psi_I(t)\rangle\langle\psi_I(t)| \\ &= U_0^\dagger(t,t_0)|\psi_S(t)\rangle\langle\psi_S(t)|U_0(t,t_0) \\ &= U_0^\dagger(t,t_0)\rho_S(t)U_0(t,t_0) \end{aligned} \tag{4.9}$$

and use the facts that (1) the time evolution of $|\psi_S(t)\rangle$ follows the Schrödinger equation $\frac{\partial}{\partial t}|\psi_S(t)\rangle = -\frac{i}{\hbar}H|\psi_S\rangle$, (2) $\frac{\partial}{\partial t}U_0^\dagger = \frac{-i}{\hbar}H_0U_0^\dagger$, and (3) U_0 and H_0 commute. The time derivative of the density operator is thus

$$\begin{aligned}\frac{\partial\rho_I(t)}{\partial t} &= \frac{\partial U_0^\dagger}{\partial t}|\psi_S(t)\rangle\langle\psi_S(t)|U_0 + U_0^\dagger|\psi_S(t)\rangle\langle\psi_S(t)|\frac{\partial U_0}{\partial t} \\ &+ U_0^\dagger\left(\frac{\partial}{\partial t}|\psi_S(t)\rangle\right)\langle\psi_S(t)|U_0 + U_0^\dagger|\psi_S(t)\rangle\left(\frac{\partial}{\partial t}\langle\psi_S(t)|\right)U_0 \\ &= -\frac{i}{\hbar}H_0U_0^\dagger|\psi_S\rangle\langle\psi_S|U_0 - \frac{i}{\hbar}U_0^\dagger\left(H_0+V\right)|\psi_S\rangle\langle\psi_S|U_0 \\ &+ \frac{i}{\hbar}U_0^\dagger|\psi_S\rangle\langle\psi_S|\left(H_0+V\right)U_0 + \frac{i}{\hbar}U_0^\dagger|\psi_S\rangle\langle\psi_S|U_0H_0 \\ &= -\frac{i}{\hbar}U_0^\dagger VU_0U_0^\dagger|\psi_S\rangle\langle\psi_S|U_0 + \frac{i}{\hbar}U_0^\dagger|\psi_S\rangle\langle\psi_S|U_0U_0^\dagger VU_0 \\ &= -\frac{i}{\hbar}[V_I,\rho_I] \end{aligned} \tag{4.10}$$

which is known as the Liouville- von Neumann equation. In the Schrödinger picture, the interaction Hamiltonian $V(t) = -\mu\cdot\tilde{\mathbf{E}}(t)$. In the interaction picture, it becomes $V_I = U_0^\dagger VU_0 = -\mu_I\cdot\tilde{\mathbf{E}}(t)$, where μ_I corresponds to the time-dependent dipole operator in the interaction picture:

$$\mu_I(t) = U_0^\dagger(t,t_0)\mu_S U_0(t,t_0) \tag{4.11}$$

In the weak field limit, we can find a solution to ρ_I by time-dependent perturbation theory.

$$\begin{aligned}\rho_I(t) &= \rho_I(t_0) + \textstyle\sum_{n=1}^{\infty}\left(\frac{-i}{\hbar}\right)^n\int_{t_0}^{t}d\tau_n\int_{t_0}^{\tau_n}d\tau_{n-1}\ldots\int_{t_0}^{\tau_2}d\tau_1 \\ &\quad [V_I(\tau_n),[V_I(\tau_{n-1}),\ldots[V_I(\tau_1),\rho_I(t_0)]\ldots]] \end{aligned} \tag{4.12}$$

where τ_j with $t\geq\tau_n\geq\cdots\geq\tau_1\geq t_0$ represent the actual time of the interac-

tions. Going back to the Hilbert space

$$\begin{aligned}
\rho(t) &= \rho(t_0) + \sum_{n=1}^{\infty} \left(\frac{-i}{\hbar}\right)^n \int_{t_0}^{t} d\tau_n \int_{t_0}^{\tau_n} d\tau_{n-1} \ldots \int_{t_0}^{\tau_2} d\tau_1 \\
&\quad U_0(t,t_0)[V_I(\tau_n),[V_I(\tau_{n-1}),\ldots[V_I(\tau_1),\rho_I(t_0)]\ldots]]U_0^{\dagger}(t,t_0) \\
&= \rho(t_0) + \sum_{n=1}^{\infty} \left(\frac{-i}{\hbar}\right)^n \int_{t_0}^{t} d\tau_n \int_{t_0}^{\tau_n} d\tau_{n-1} \ldots \int_{t_0}^{\tau_2} d\tau_1 \tilde{\mathbf{E}}(\tau_n)\tilde{\mathbf{E}}(\tau_{n-1})\ldots\tilde{\mathbf{E}}(\tau_1) \\
&\quad U_0(t,t_0)[\mu_I(\tau_n),[\mu_I(\tau_{n-1}),\ldots[\mu_I(\tau_1),\rho_I(t_0)]\ldots]]U_0^{\dagger}(t,t_0) \qquad (4.13)
\end{aligned}$$

4.1.3 Polarization and nonlinear response function

Now we proceed to describe the interaction of a non-relativistic quantum system with the electromagnetic field. The polarization density corresponds to the induced and permanent electric dipole moment in a system. It is controlled by light-matter interaction and inter-molecular forces and can be respresented by the expectation value of the dipole operator μ:

$$\tilde{\mathbf{P}}(\mathbf{r},t) = \mathrm{Tr}[\mu\rho(t)] = \langle\mu\rho(t)\rangle \qquad (4.14)$$

We now expand the polarization in powers of the electric field $\tilde{\mathbf{E}}(t)$ ($\tilde{\mathbf{E}}(t) = \mathbf{E}(t)e^{-i\omega t} + \mathbf{E}^*(t)e^{i\omega t}$) to obtain

$$\tilde{\mathbf{P}} = \epsilon_0\left(\chi^{(1)}\tilde{\mathbf{E}}(t) + \chi^{(2)}\tilde{\mathbf{E}}^2(t) + \chi^{(3)}\tilde{\mathbf{E}}^3(t) + \ldots\right) \qquad (4.15)$$

where $\chi^{(n)}$ are the n^{th} order optical susceptibilities. Comparing Eq. 4.15 with Eqs. 4.13 and 4.14 for the terms in powers of the electric field $\tilde{\mathbf{E}}(t)$, we obtain the nth order polarization

$$\begin{aligned}
\tilde{\mathbf{P}}^{(n)}(\mathbf{r},t) &= \langle\mu\rho^n(t)\rangle \\
&= \left(\frac{-i}{\hbar}\right)^n \int_{t_0}^{t} d\tau_n \int_{t_0}^{\tau_n} d\tau_{n-1} \ldots \int_{t_0}^{\tau_2} d\tau_1 \tilde{\mathbf{E}}(\tau_n)\tilde{\mathbf{E}}(\tau_{n-1})\ldots\tilde{\mathbf{E}}(\tau_1) \\
&\quad \langle\mu U_0(t,t_0)[\mu_I(\tau_n),[\mu_I(\tau_{n-1}),\ldots[\mu_I(\tau_1),\rho_I(t_0)]\ldots]]U_0^{\dagger}(t,t_0)\rangle \\
&= \left(\frac{-i}{\hbar}\right)^n \int_{t_0}^{t} d\tau_n \int_{t_0}^{\tau_n} d\tau_{n-1} \ldots \int_{t_0}^{\tau_2} d\tau_1 \tilde{\mathbf{E}}(\tau_n)\tilde{\mathbf{E}}(\tau_{n-1})\ldots E(\tau_1) \\
&\quad \langle\mu_I(t)[\mu_I(\tau_n),[\mu_I(\tau_{n-1}),\ldots[\mu_I(\tau_1),\rho_I(t_0)]\ldots]]\rangle
\end{aligned} \qquad (4.16)$$

Here we introduce another set of time variables as depicted in Figure 4.1

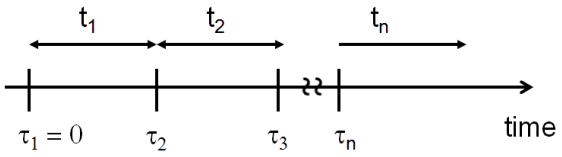

Figure 4.1: Time ordering

$$\begin{aligned} \tau_1 &= 0 \\ t_1 &= \tau_2 - \tau_1 \\ t_2 &= \tau_3 - \tau_2 \\ &\vdots \\ t_n &= t - \tau_n \end{aligned} \tag{4.17}$$

and transform Eq. 4.16 to the following equation:

$$\begin{aligned} \tilde{\mathbf{P}}^{(n)}(\boldsymbol{r},t) &= \int_0^\infty dt_n \int_0^\infty dt_{n-1} \ldots \int_0^\infty dt_1 S^{(n)}(t_n, t_{n-1}, \ldots, t_1) \\ &\quad \tilde{\mathbf{E}}(\boldsymbol{r}, t-t_n)\tilde{\mathbf{E}}(\boldsymbol{r}, t-t_n-t_{n-1})\tilde{\mathbf{E}}(\boldsymbol{r}, t-t_n-t_{n-1}\cdots-t_1) \end{aligned} \tag{4.18}$$

with $S^{(n)}(t_n, t_{n-1}, \ldots, t_1)$ the nth order nonlinear response function, carrying the complete microscopic information for the calculation of optical measurements.

$$\begin{aligned} &S^{(n)}(t_n, t_{n-1}, \ldots, t_1) \equiv \left(\frac{-i}{\hbar}\right)^n \theta(t_1)\theta(t_2)\ldots\theta(t_n) \\ &\langle \mu_I(t_n+\cdots+t_1)[\mu_I(t_{n-1}+\cdots+t_1), [\ldots[\mu_I(t_1)[\mu_I(0), \rho_I(-\infty)]]\ldots]]\rangle \end{aligned} \tag{4.19}$$

$$\theta(t) \begin{cases} 1 & \text{if } t \geq 0 \\ 0 & \text{if } t < 0 \end{cases} \tag{4.20}$$

$\theta(t)$ is the heaviside function to ensure time ordering.

4.1.4 n-wave mixing signal

The nth order polarization described in Eq. 4.18 is related to a new generated field by the Maxwell equation:

$$\nabla \times \nabla \times \tilde{\mathbf{E}}(\boldsymbol{r},t) + \frac{n^2}{c^2}\frac{\partial^2 \tilde{\mathbf{E}}(\boldsymbol{r},t)}{\partial t^2} = -\frac{4\pi}{c^2}\frac{\partial^2[\sum_{n=2,3,\ldots}\tilde{\mathbf{P}}^{(n)}(\boldsymbol{r},t)]}{\partial t^2} \tag{4.21}$$

with vector fields:

$$\tilde{\mathbf{E}}(\boldsymbol{r},t) = \sum_{j=1}^{n}[\mathbf{E}_j(\boldsymbol{r},t)\exp(i\boldsymbol{k}_j\boldsymbol{r} - i\omega_j t) + \mathbf{E}_j^*(\boldsymbol{r},t)\exp(-i\boldsymbol{k}_j\boldsymbol{r} + i\omega_j t)] \tag{4.22}$$

Here we separate the linear and nonlinear polarization terms in Eq. 4.21, where the linear polarization is denoted by "n" in the 2^{nd} term on the left-hand-side, with $k_j = \frac{\omega_j}{c}n_j$. The nonlinear polarization in Eq. 4.21 (the term on the right-hand side) can be expanded as:

$$\tilde{\mathbf{P}}^{(n)}(\boldsymbol{r},t) = \sum_s \mathbf{P}_s^{(n)}(t)\exp(i\boldsymbol{k}_s\boldsymbol{r} - i\omega_s t) + c.c. \tag{4.23}$$

where s refers to different nonlinear pathways, and $\boldsymbol{k}_s$ and ω_s are the corresponding combination of the incoming wavevectors and frequencies.

$$\begin{aligned} \boldsymbol{k}_s &= \pm\boldsymbol{k}_1 \pm \boldsymbol{k}_2 \pm \boldsymbol{k}_3 \cdots \pm \boldsymbol{k}_n \\ \omega_s &= \pm\omega_1 \pm \omega_2 \pm \omega_3 \cdots \pm \omega_s \end{aligned} \tag{4.24}$$

To simplify the notations, we look at a specific induced polarization with wavevector $\boldsymbol{k}_s$ and omit (n) because the following derivation holds for all nth $(n > 2)$ order transitions:

$$\tilde{\mathbf{P}}(\boldsymbol{r},t) = \mathbf{P}_s(t)\exp(i\boldsymbol{k}_s\boldsymbol{z} - i\omega_s t) + c.c. \tag{4.25}$$

We assume the solution for Eq. 4.21 is a field with wavevector $\boldsymbol{k}_s'$:

$$\tilde{\mathbf{E}}(\boldsymbol{r},t) = \mathbf{E}_s(\boldsymbol{z},t)\exp(i\boldsymbol{k}_s'\boldsymbol{z} - i\omega_s t) + c.c. \tag{4.26}$$

where

$$|\boldsymbol{k}_s'| \equiv \frac{\omega_s}{c} n_s \tag{4.27}$$

After plugging in Eqs. 4.26 and 4.25 into Eq. 4.21 and assuming the the polarization has a slowly varying envelope in time compared with the optical period:

$$\left| \frac{\partial}{\partial t} \mathbf{P}_s(t) \right| \ll |\omega_s \mathbf{P}_s(t)| \tag{4.28}$$

the right-hand-side of Eq. 4.21 becomes

$$\frac{-4\pi}{c^2} \frac{\partial^2 \tilde{\mathbf{P}}_s(t)}{\partial t^2} = \frac{4\pi\omega_s^2}{c^2} \mathbf{P}_s(t) \exp(i\boldsymbol{k}_s \boldsymbol{r} - i\omega_s t) + c.c. \tag{4.29}$$

To simplify the left-hand-side of Eq. 4.21, we first apply the slowly varying amplitude approximation for the field envelope $\mathbf{E}_s(\boldsymbol{z}, t)$

$$\left| \frac{\partial^2}{\partial z^2} \mathbf{E}_s(\boldsymbol{z}, t) \right| \ll \left| \boldsymbol{k}_s' \frac{\partial}{\partial z} \mathbf{E}_s(\boldsymbol{z}, t) \right| \tag{4.30}$$

and replace $\nabla \times \nabla \times$ with $-\nabla^2$, the left-hand-side of Eq. 4.21 becomes:

$$\begin{aligned}
& \nabla \times \nabla \times \tilde{\mathbf{E}}(\boldsymbol{r}, t) + \frac{n^2}{c^2} \frac{\partial^2 \tilde{\mathbf{E}}(\boldsymbol{r}, t)}{\partial t^2} \\
= \; & -2ik_s \frac{\partial \mathbf{E}(\boldsymbol{r}, t)}{\partial z} \exp(i\boldsymbol{k}_s \boldsymbol{r} - i\omega_s t) - |\boldsymbol{k}_s|^2 \mathbf{E}(\boldsymbol{r}, t) \exp(i\boldsymbol{k}_s \boldsymbol{r} - i\omega_s t) \\
+ \; & \frac{n_s^2 \omega_s^2}{c^2} \mathbf{E}(\boldsymbol{r}, t) \exp(i\boldsymbol{k}_s \boldsymbol{r} - i\omega_s t) + c.c. \\
= \; & -2ik_s \frac{\partial \mathbf{E}(\boldsymbol{r}, t)}{\partial z} \exp(i\boldsymbol{k}_s \boldsymbol{r} - i\omega_s t) + c.c.
\end{aligned} \tag{4.31}$$

Combining Eqs. 4.29 and 4.31, we get

$$ik_s \frac{\partial \mathbf{E}(\boldsymbol{r}, t)}{\partial z} = -\frac{2\pi\omega_s^2}{c^2} \mathbf{P}_s(t) \exp[i(\boldsymbol{k}_s - \boldsymbol{k}_s')\boldsymbol{r}] \tag{4.32}$$

From Eq. 4.32, it is obvious that the induced nonlinear field strength $\mathbf{E}(\boldsymbol{r},t)$ is directly in proportional to the nonlinear polarization amplitude $\mathbf{P}_s(t)$, i.e.

$$\mathbf{E}(\boldsymbol{r},t) \propto i\omega_s \mathbf{P}_s^{(n)}(\boldsymbol{r},t) \tag{4.33}$$

4.1.5 Linear response

It is obvious from Eq. 4.19 that for nth order process, S$^{(n)}$ contains 2^n terms when the commutators are evaluated explicitly. However, only half of the 2^n terms are independent, and the other half is simply their complex conjugates. We now expand the linear response $S^{(1)}$:

$$\begin{aligned} S^{(1)}(t_1) &= \frac{-i}{\hbar}\theta(t_1)\langle\mu_I(t_1)[\mu_I(0),\rho_I(-\infty)]\rangle \\ &= \frac{-i}{\hbar}\theta(t_1)\left(\langle\mu_I(t_1)\mu_I(0)\rho_I(-\infty)\rangle - \langle\mu_I(t_1)\rho_I(-\infty)\mu_I(0)\rangle\right) \\ &= \frac{-i}{\hbar}\theta(t_1)\left(\langle\mu_I(t_1)\mu_I(0)\rho_I(-\infty)\rangle - \langle\rho_I(-\infty)\mu_I(0)\mu_I(t_1)\rangle\right) \end{aligned} \tag{4.34}$$

We can illustrate the above two processes with double-sided Feynman diagrams [39]:

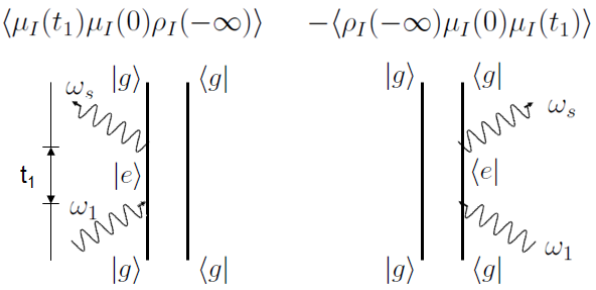

The rules for the Feynman diagrams are:

1. The density operator is represented by two vertical lines, the left one is the ket, the right one the bra.
2. Time is running from bottom to top vertically.
3. Each arrow corresponds to an interaction with the light field. The last arrow refers to emission of the signal.
4. Each diagram has a factor $(-1)^k$, where k is the number of interactions on

the bra. This is because each time the interaction μ_I in a commutator acts from the right, it carries a minus sign. The last emission is excluded from this rule, because the last interaction does not come from a term in a commutator.
5. An arrow pointing to the right labeled as ω_j represents a field $\mathbf{E}_j e^{i(-\omega_j t + \boldsymbol{k}_j \cdot \boldsymbol{r} + \phi)}$. An arrow pointing to the left and labeled ω_j represents an field $\mathbf{E}_j^* e^{i(\omega_j t - \boldsymbol{k}_j \cdot \boldsymbol{r} - \phi)}$. The emitted signal has frequency and wavevector the sum of the input frequencies and wavevectors with their appropriate signs.
6. An arrow pointing towards the diagram corresponds to excitation of the ket or bra, and an arrow pointing away from the diagram refers to de-excitation.
7. The last interaction must end in a population state, e.g. in the diagram for the linear absorption, the final state is the ground state $|g\rangle\langle g|$.

$\langle \mu_I(t_1)\mu_I(0)\rho_I(-\infty)\rangle$ describes a system in $|g\rangle\langle g|$ that absorbs a photon at $t = 0$, and the coherence $|e\rangle\langle g|$ evolves until $t = t_1$ when the system relaxes back to the ground state. The response function $\langle \mu_I(t_1)\mu_I(0)\rho_I(-\infty)\rangle$ is constructed as:

- $\rho(-\infty) = \rho_{gg}$
- At t=0, light interacts with the medium and generates an off-diagonal matrix element $\rho_{eg}(0)$. The probability of this happening is proportional to the transition dipole moment μ_{eg}.
- $\mu_{eg}(t)$ evolves with time from t = 0 to t_1

$$\rho_{eg}(t) \propto \mu_{eg}(t) = \mu_{eg} e^{-i\omega_{eg} t_1} e^{-\Gamma t_1} \tag{4.35}$$

- At $t = t_1$, the medium is de-excited back to ground state. This process is proportional to μ_{eg}.

$$S^{(1)}(t_1) \propto \mu_{eg}^2 e^{-i\omega_{eg} t_1} e^{-\Gamma t_1} \tag{4.36}$$

- Finally, assuming $\tilde{E}(t - t_1) = |E(t - t_1)|(e^{-i\omega t} + e^{i\omega t})$ and using Eq. 4.36,

the first order polarization is

$$\begin{aligned} P^{(1)}(t) &= \frac{-i}{\hbar}\int_0^\infty dt_1 E(t-t_1)S^{(1)} \\ &\propto \frac{-i}{\hbar}\int_0^\infty dt_1 |E(t-t_1)|(e^{-i\omega t}+e^{i\omega t})\mu_{eg}^2 e^{-i\omega_{eg}t_1}e^{-\Gamma t_1} \\ &= \frac{-i}{\hbar}\mu_{eg}^2(e^{-i\omega t}\int_0^\infty dt_1 |E(t-t_1)|e^{i(\omega-\omega_{eg})t_1}e^{-\Gamma t_1} \\ &+ e^{i\omega t}\int_0^\infty dt_1 |E(t-t_1)|e^{-i(\omega+\omega_{eg})t_1}e^{-\Gamma t_1}) \end{aligned} \tag{4.37}$$

We note that for excitation near resonance, the light frequency is close to the energy gap $\omega \approx \omega_{eg}$, the term $e^{i(\omega-\omega_{eg})t_1}$ is slowly varying, while the term $e^{-i(\omega+\omega_{eg})t_1}$ oscillates much faster. The second integral can be neglected as long as the variation in the envelope of $E(t)$ is also slow compare to its carrier frequency. The above condition is called the rotating wave approximation. The excitation pulse is centered at t_1 before the spontaneous emission.

4.1.6 Third-order response function

In a centrosymmetric medium, the even-order response functions disappear because of inversion symmetry in the material. The lowest non-zero nonlinear response function for an isotropic system is therefore $S^{(3)}$. Following Eq. 4.18 and 4.19, $S^{(3)}$ can be written as:

$$\begin{aligned} S^{(3)}(t_1) &= \left(\frac{-i}{\hbar}\right)^3 \theta(t_1)\theta(t_2)\theta(t_3)\langle \mu_I(t_3+t_2+t_1),[\mu_I(t_2+t_1), \\ &\quad [\mu_I(t_1),[\mu_I(0),\rho_I(-\infty)]]]\rangle \\ &= \left(\frac{-i}{\hbar}\right)^3 \theta(t_1)\theta(t_2)\theta(t_3)\sum_{\alpha=1}^{4}[R_\alpha(t_3,t_2,t_1)-R_\alpha^*(t_3,t_2,t_1)] \end{aligned} \tag{4.38}$$

where R_α and R_α^* are different Liouville pathways towards third-order response:

$$\begin{aligned}
&\sum_{\alpha=1}^{4}[R_\alpha(t_3,t_2,t_1) - R_\alpha^*(t_3,t_2,t_1)] \\
= \;& \langle \mu_I(t_3+t_2+t_1)\mu_I(0)\rho_I(-\infty)\mu_I(t_1)\mu_I(t_2+t_1)\rangle \Rightarrow R_1 \\
+ \;& \langle \mu_I(t_3+t_2+t_1)\mu_I(t_1)\rho_I(-\infty)\mu_I(0)\mu_I(t_2+t_1)\rangle \Rightarrow R_2 \\
+ \;& \langle \mu_I(t_3+t_2+t_1)\mu_I(t_2+t_1)\rho_I(-\infty)\mu_I(0)\mu_I(t_1)\rangle \Rightarrow R_3 \\
+ \;& \langle \mu_I(t_3+t_2+t_1)\mu_I(t_2+t_1)\mu_I(t_1)\mu_I(0)\rho_I(-\infty)\rangle \Rightarrow R_4 \\
- \;& \langle \mu_I(t_3+t_2+t_1)\mu_I(t_2+t_1)\mu_I(t_1)\rho_I(-\infty)\mu_I(0)\rangle \Rightarrow R_1^* \\
- \;& \langle \mu_I(t_3+t_2+t_1)\mu_I(t_2+t_1)\mu_I(0)\rho_I(-\infty)\mu_I(t_1)\rangle \Rightarrow R_2^* \\
- \;& \langle \mu_I(t_3+t_2+t_1)\mu_I(t_1)\mu_I(0)\rho_I(-\infty)\mu_I(t_2+t_1)\rangle \Rightarrow R_3^* \\
- \;& \langle \mu_I(t_3+t_2+t_1)\rho_I(-\infty)\mu_I(0)\mu_I(t_1)\mu_I(t_2+t_1)\rangle \Rightarrow R_4^*
\end{aligned} \tag{4.39}$$

For a two-level system, pathways $R_1 - R_4$ can be illustrated by the Feynman diagrams in Figure 4.2. For example, R_1 corresponds to the following pathway: at $t = 0$, absorption of light at frequency ω_1 on the left ket of the diagram brings the vertex from the ground state $|g\rangle$ to the excited state $|e\rangle$. The amplitude of the transition is in proportional to $-\frac{i}{\hbar}\langle e|\mathbf{E}(t)e^{-i\omega_1 t}|g\rangle|_{t=0}$. At $t = t_1$, absorption at frequency ω_2 on the right bra of the diagram brings the vertex from $|g\rangle$ to $|e\rangle$, whose amplitude is in proportional to $\frac{i}{\hbar}\langle g|\mathbf{E}^*(t)e^{i\omega_2 t_1}|e\rangle$. At $t = t_1+t_2$, the emission at frequency ω_3 can be expressed as $\frac{i}{\hbar}\langle e|\mathbf{E}^*(t)e^{-i\omega_3(t_1+t_2)}|g\rangle$. Finally, at $t = t_1 + t_2 + t_3$, the emitted signal has frequency at $\omega_s = -\omega_1 + \omega_2 - \omega_3$. Similar interpretation can be generalized to other Liouville pathways.

4.2 Two-dimensional spectroscopy

There are various third-order spectroscopy techniques, e.g. photon echoes, hole burning and pump-probe absorption that utilize different laser pulse geometries and sequences for measuring the third-order response of a sample. In this section, we will first introduce the experimental geometries of each technique. Then we will compare different techniques after constructing the for-

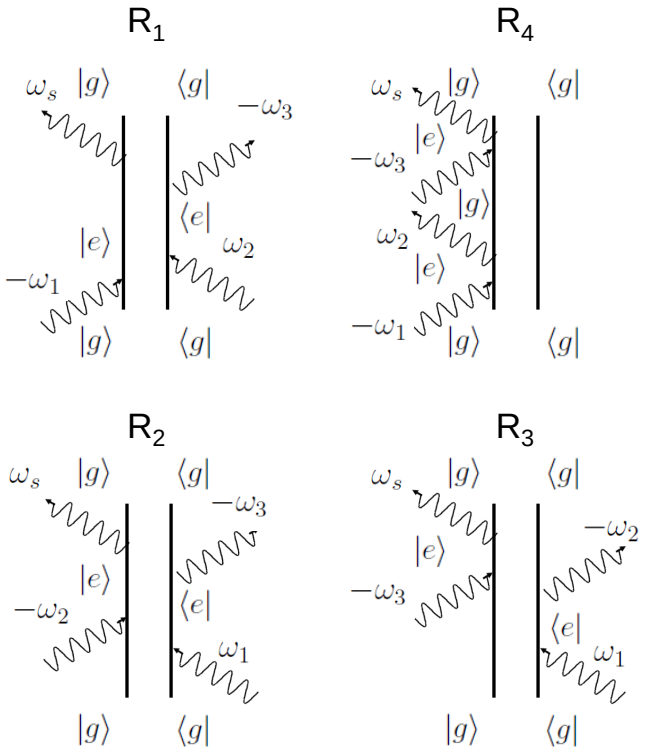

Figure 4.2: Liouville pathways four-wave-mixing in a two-level system. R_1: non-rephasing (NR), stimulated emission (SE). R_2: rephasing (R), SE. R_3: rephasing, ground state bleaching (GSB). R_4: non-rephasing, GSB.

malism of each spectroscopy. The Fourier transform of the third-order response $S^{(3)}(t_1, T, t_3)$ leads to the two-dimensional spectrum $S^{(3)}(\omega_1, T, \omega_3)$ which reveals homogeneous and inhomogeneous broadening in a medium, as well as how energy transfers between transition dipoles. Two Liouville pathway selecting methods, phase-matching and phase-cycling will also be discussed in this section.

The most intuitive way to probe third-order optical response is to excite with three femtosecond excitation pulses in full collinear geometry [28] (Figure 4.3(A)) or boxcar geometry [64–66] (Figure 4.3(B)). In the collinear geometry, a series of phase-locked pulses are generated by a pulse shaper and travel along the same path before reaching the sample. In this case, the relative phase stability between pulses is well-maintained as all pulses experience the same amount of jitters in the optics. Because the excitation pulse energy is orders of magnitude higher than $S(\tau_1, \tau_2)$, where τ_1 refers to delay between the first and the second pulses and τ_2 refers to delay between the second and the third pulses, it can saturate the detector easily if one directly measures the absorption spectrum. Generally, the third-order fluorescence spectrum is collected orthogonal to the beam propagation axis. For samples with fast non-radiative excited-state decays like DNA, it is challenging to generate enough fluorescence without photo-damaging the samples.

2D spectroscopy in boxcar or four-wave-mixing (FWM) geometry, on the other hand, excites the sample with three ultrafast pulses of different wavevectors $\boldsymbol{k_1}$, $\boldsymbol{k_2}$, and $\boldsymbol{k_3}$, and measures third order response along the fourth direction. An important advantage of the boxcar geometry is that the signal is generated in a new direction ($\boldsymbol{k_{sa}}$, $\boldsymbol{k_{sb}}$) and has essentially no background. The third-order response can be measured directly or mixed with a local oscillator beam $\tilde{\mathbf{E}}_{LO}$, which has the same wavevector. The later method is called heterodyne detection. Ideally, if the local oscillator is noise-free, heterodyne detection can enhance the signal-to-noise ratio (S/N). In a boxcar geometry, the pulse train is either generated by spatially separating the pulses with a series of beam splitters or by a two-dimensional pulse shaper [66]. However, both methods are complicated to implement in the deep UV. As discussed in Chapter 2.4, extra diffractive [25, 26] and active interferometric stabilization [27] optics are required to maintain phase stability for a conventional

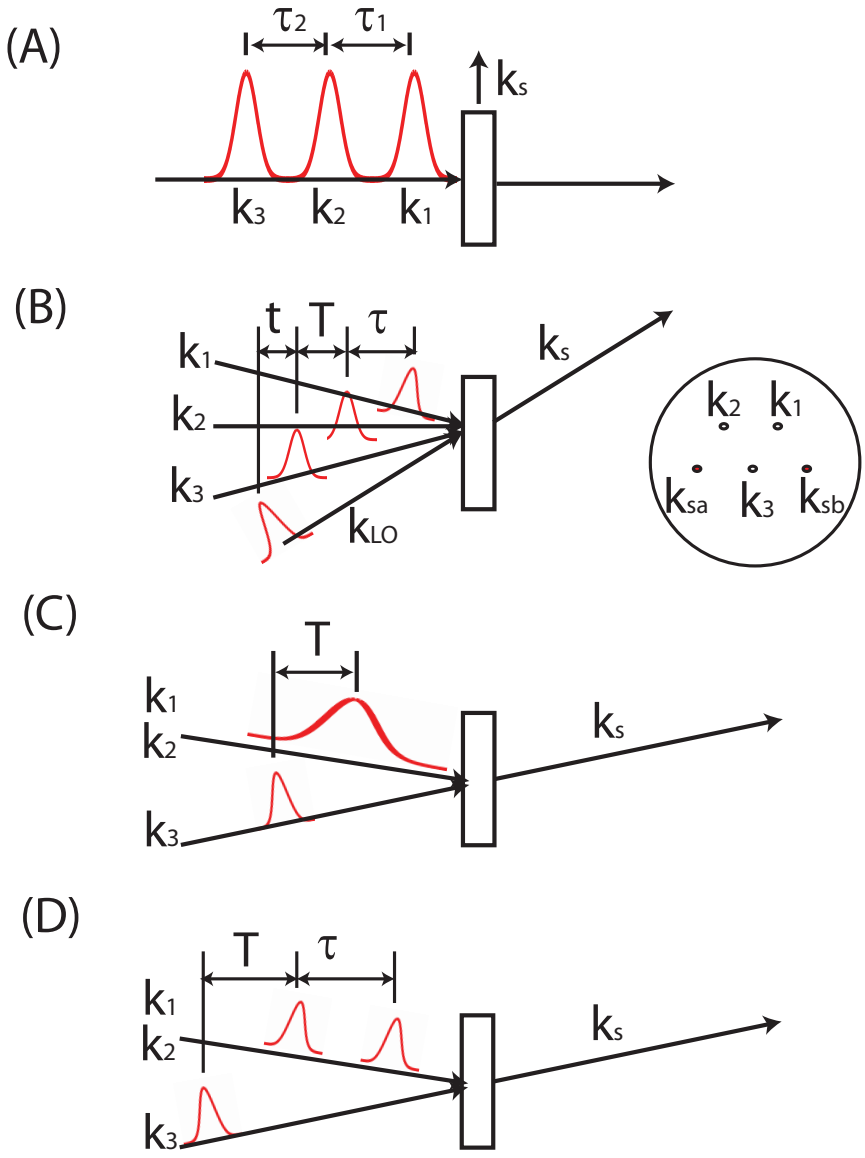

Figure 4.3: Schematic layouts of 2D spectroscopy, where $\mathbf{k}_n$ $(n = 1, 2, 3)$ are the excitation, $\mathbf{k}_{LO}$ the local oscillator, and $\mathbf{k}_s$ the emission wavevectors. (A) Collinear geometry: fluorescence orthogonal to the excitation wavevectors is collected. (B) Four-wave mixing or boxcar geometry: rephasing or non-rephasing signals are emitted at the phase-matching angle, where an local oscillator helps to retrieve its phase. (C) Hole-burning method: the transmission probe spectrum is measured after the excitation with a narrow bandwidth pump. (D) Pump-probe geometry using a pulse shaper.

interferometer-based setup, and two-dimensional pulse shapers in the deep UV are not available.

The third approach, hole burning spectroscopy, is to excite a group of molecules with in a broad inhomogeneous line using a narrow bandwidth pump and then probe its absorption spectrum $S(T, \omega_{probe})$ with a broadband pulse as depicted in Figure 4.3(C). A full 2D spectrum $S(\omega_{pump}, T, \omega_{probe})$ can be mapped out by scanning the pump frequency ω_{pump} across the spectral region of interest, and the 2D relaxation spectrum is constructed by collecting 2D spectra at several different pump probe delays T. This hole burning technique does not require phase stability between the pump and probe, but it sacrifices time resolution for spectral selectivity as the pump pulse is stretched to picoseconds when its bandwidth is narrowed down to less than the molecular homogeneous linewidth. The measured 2D spectrum is therefore averaged over time delays.

Our approach, the three-pulse phase-locked pump-probe spectroscopy (Figure 4.3(D)), is a combination of the hole burning method and collinear geometry. It utilizes a pump-probe geometry where the collinear pump pulse pair ($\boldsymbol{k_1} = \boldsymbol{k_2}$) is generated by a pulse shaper [30, 32], and the probe pulse serves simultaneously as the third excitation and the local oscillator. As will be explained in more detail later, the two pump pulses are inherently phase-locked and different phase-cycling conditions can be applied to select specific Liouville pathways [28] and to remove transient absorption background [32]. As opposed to the hole burning method, in this approach, the spectral resolution is determined by the delay between the first two pulses and not by the pulse bandwidth, therefore, the excitation pulses are allowed to be short to achieve good temporal resolution without sacrificing the spectral resolution.

4.2.1 Photon echo spectroscopy

We follow the derivations in [63, 67–70] to introduce the theoretical description of photon echo, hole burning, and three-pulse pump-probe spectroscopy. The most general external field for a four-wave-mixing process is

$$\begin{aligned} \tilde{\mathbf{E}}(\boldsymbol{r}, t) &= \mathbf{E}_1(t) e^{i(\omega_1 t - \boldsymbol{k}_1 \cdot \boldsymbol{r} - \phi_1)} + \mathbf{E}_2(t-\tau) e^{i(\omega_2 t - \boldsymbol{k}_2 \cdot \boldsymbol{r} - \phi_2)} \\ &+ \mathbf{E}_3(t-\tau-T) e^{i(\omega_3 t - \boldsymbol{k}_3 \cdot \boldsymbol{r} - \phi_3)} + c.c. \end{aligned} \tag{4.40}$$

where $E_j, j = 1, 2, 3$ is the temporal envelope of the jth incident pulse, each has wavevector $\boldsymbol{k}_j$ and mean frequency ω_j. As illustrated in Figure 4.3(B), the three pulses are delayed by time intervals T and τ. The first two pulses of the three-pulse sequence form a grating in the medium, and the third pulse diffracts off the grating. To satisfy different phase-matching conditions, the induced field has two different wave vectors: $\boldsymbol{k}_{sa}$ and $\boldsymbol{k}_{sb}$. After the third excitation pulse, the stimulated photon echo (SPE) signal propagating along $\boldsymbol{k}_{sa} = -\boldsymbol{k}_1 + \boldsymbol{k}_2 + \boldsymbol{k}_3$. The other signal following different Liouville pathways is generated towards the direction of $\boldsymbol{k}_{sb} = \boldsymbol{k}_1 - \boldsymbol{k}_2 + \boldsymbol{k}_3$.

Figure 4.2 illustrates the Liouville pathways of four-wave-mixing process for a two-level system in a phase space of the density matrix. Because in pathways R_1 and R_2, the response function describes the dynamics of the excited-state population ρ_{ee} created by the first two excitation pulses, R_1 and R_2 are related to stimulated emission from the electronically excited-state. In pathways R_3 and R_4, the response function describes the dynamics of the ground state population ρ_{gg} created by the the first two excitation pulses, and is related to ground state bleaching.

Combining Eqs. 4.18 and 4.40 and invoking the rotating wave approximation, the photon echo polarization is described by

$$\begin{aligned}
&\tilde{\mathbf{P}}^{(3)}_{SPE}(\boldsymbol{k}_a, t, T, \tau) = \left(\frac{-i}{\hbar}\right)^3 \int_0^\infty dt_3 \int_0^\infty dt_2 \int_0^\infty dt_1 \\
\times\ & [R_2(t_3, t_2, t_1) + R_3(t_3, t_2, t_1)]\chi(t_3 - t_1) \\
\times\ & \mathbf{E}_3(t - \tau - T - t_3)\mathbf{E}_2(t - \tau - t_3 - t_2)\mathbf{E}_1^*(t - t_3 - t_2 - t_1) \\
\times\ & \exp[i(\omega_3 + \omega_2 - \omega_1)t_3 + i(\omega_2 - \omega_1)t_2 - i\omega_1 t_1]\exp[i(-\phi_1 + \phi_2 + \phi_3)]
\end{aligned} \tag{4.41}$$

Here $\chi(t_3 - t_1)$ is the inhomogeneous broadening because different molecules are imbedded in different local environments which affect the transition frequencies of chromophores. Note that $\chi(t)$ here is different from the n_{th} order optical susceptibilities $\chi^{(n)}$ defined by Eq. 4.15. The formalism of inhomogeneous broadening will be explained in detail in Appendix B. There are two pathways R_2 and R_3 satisfying the phase-matching condition for stimulated photo echoes, which can be described as follows. At $t = 0$, the first pulses excites the initial ground state density matrix ρ_{gg} to an optical coherence ρ_{ge},

which evolves according to the time evolution operator. At the end of the time interval $\sim \tau$, the coherence acquires a phase $\omega_{eg}\tau$. The second interaction at $t = \tau$, produces population in the excited (R_2: ρ_{ee}) or ground (R_3: ρ_{gg}) states, whose transition probabilities depend on the phase of coherence relative to the that of the second pulse. At $t = \tau + T$, the third pulse generates a coherence ρ_{eg} that is oscillating in the opposite direction to the first coherence: $e^{-i\omega_{eg}t}$. Finally, at $t = \tau + T + \tau$, the oscillating terms cancels each other, a phenomenon called rephasing. If we also assume broad inhomogeneous dephasing, i.e. $\chi(\omega) = 1$, its Fourier transform pair: $\chi(t)$ is essentially a δ function. The $\chi(t_3 - t_1)$ factor in the SPE process reaches a maximum at $t_1 \sim t_3$, i.e. $t = \tau + T + \tau$. Combining the above two conditions, the echo is peaked at $t = \tau$ and the effect of the inhomogeneous dephasing is eliminated. For $t > \tau + T + \tau$, dephasing starts to kick in, and echo rapidly disappears.

4.2.2 Impulsive limit

In time-resolved nonlinear spectroscopy, we often use pulses that are short compared to the timescale of the homogeneous dephasing and solvent reorganization processes, but long compared to the oscillation period of the carrier. Therefore, we can invoke the *impulsive limit* and approximate the envelope of the excitation field with a δ function. The external field in Eq. 4.40 is

$$\begin{aligned} \tilde{\mathbf{E}}(\boldsymbol{r}, t) &= \mathbf{A}_1 \delta(t + T + \tau) e^{i(\omega_1 t - \boldsymbol{k}_1 \cdot \boldsymbol{r})} + \mathbf{A}_2 \delta(t + T) e^{i(\omega_2 t - \boldsymbol{k}_2 \cdot \boldsymbol{r})} \\ &+ \mathbf{A}_3 \delta(t) e^{i(\omega_3 t - \boldsymbol{k}_3 \cdot \boldsymbol{r})} + c.c. \end{aligned} \tag{4.42}$$

In the homodyne detection scheme, the stimulated photon echo signal $\mathfrak{S}_{SPE}$ is the total integral of the new generated field in the $\boldsymbol{k}_{sa}$ direction.

Combining Eqs. 4.33, 4.41 and 4.42, we obtain:

$$\begin{aligned} \mathfrak{S}_{SPE}(T, \tau) &\propto \int_0^\infty |P^{(3)}_{SPE}(\boldsymbol{k}_{sa}, t, T, \tau)|^2 dt \\ &= \int_0^\infty |R_2(t, T, \tau) + R_3(t, T, \tau)|^2 |\chi(t - \tau)|^2 dt \end{aligned} \tag{4.43}$$

Although inhomogeneous broadening is eliminated at $t = \tau$, the signal $\mathfrak{S}_{SPE}$ has contributions from all t, and as a result, $\mathfrak{S}_{SPE}$ is not free of inhomoge-

neous broadening. In the *large inhomogeneous broadening limit*, where the inhomogeneous dephasing time is shorter than other dynamic timescales of the system, $\chi(t-\tau) \sim \delta(t-\tau)$, Eq. 4.43 becomes

$$\mathfrak{S}_{SPE}(T,\tau) \propto |R_2(\tau,T,\tau) + R_3(\tau,T,\tau)|^2 \tag{4.44}$$

4.2.3 Heterodyne detection

In the case of heterodyne detection, the generated field is mixed with a new local oscillator field of the same wave vector. There are two ways to measure the signal, either directly, or directing the light into a spectrometer. From Eqs. 4.41 and 4.33, the heterodyne-detected stimulated photon echo (HSPE) signal $\mathfrak{S}_{HSPE}$ is

$$\begin{aligned} \mathfrak{S}_{HSPE}(t,T,\tau,\phi) &\propto \left|\tilde{\mathbf{P}}_{SPE} + \tilde{\mathbf{E}}_{LO}\right|^2 \\ &= \left|\tilde{\mathbf{P}}_{SPE}\right|^2 + \left|\tilde{\mathbf{E}}_{LO}\right|^2 - 2\,\mathrm{Im}\,\mathbf{P}_{SPE}\mathbf{E}^*_{LO} \end{aligned} \tag{4.45}$$

Because the third-order polarization $\tilde{\mathbf{P}}_{SPE}$ is much smaller than the local oscillator, the first term in Eq. 4.45 can be neglected. We further assume $\tilde{\mathbf{E}}_{LO}$ is constant throughout the measurement, therefore $\left|\tilde{\mathbf{E}}_{LO}\right|^2$ remains constant. The change in the signal is

$$\begin{aligned} & \mathfrak{S}_{HSPE}(t,T,\tau,\phi) \\ \propto\ & \frac{-2}{\hbar^3}\,\mathrm{Im}\int_{-\infty}^{\infty} dt_4 \mathbf{E}^*_{LO}(t-t_4)\mathbf{P}^{(3)}_{SPE}(\boldsymbol{k}_a,t_4,T,\tau)\exp[i\phi + i(\omega_{LO}-\omega_{sa})t_4] \\ =\ & \frac{2}{\hbar^3}\,\mathrm{Re}\int_{-\infty}^{\infty} dt_4 \int_0^{\infty} dt_3 \int_0^{\infty} dt_2 \int_0^{\infty} dt_1 [R_2(t_3,t_2,t_1) + R_3(t_3,t_2,t_1)] \\ \times\ & \chi(t_3-t_1)\mathbf{E}^*_{LO}(t-\tau-T-t_4)\mathbf{E}_3(t-\tau-T-t_3) \\ \times\ & \mathbf{E}_2(t-\tau-t_3-t_2)\mathbf{E}^*_1(t-t_3-t_2-t_1) \\ \times\ & \exp[i\phi + i(\omega_{LO}-\omega_{sa})t_4 + i\omega_{sa}t_3 + i(\omega_2-\omega_1)t_2 - i\omega_1 t_1] \end{aligned} \tag{4.46}$$

where ϕ is the phase of the local oscillator with respect to the third excitation pulse. and $\omega_{sa} = \omega_3 + \omega_2 - \omega_1$ is the central frequency of the third-order polarization. In the impulsive and large inhomogeneous broadening limits and

the degenerate case where $\omega_1 = \omega_2 = \omega_3 = \omega_{LO}$, we obtain

$$\begin{aligned}\mathfrak{S}_{HSPE}(t,T,\tau,\phi) &\propto \frac{2}{\hbar^3}\,\mathrm{Re}[(R_2(t,T,\tau)+R_3(t,T,\tau))e^{i\phi}] \\ &= \begin{cases} \frac{2}{\hbar^3}\,\mathrm{Re}[R_2(t,T,\tau)+R_3(t,T,\tau)] & \text{for } \phi = 0 \\ \frac{-2}{\hbar^3}\,\mathrm{Im}[R_2(t,T,\tau)+R_3(t,T,\tau)] & \text{for } \phi = \pi/2 \end{cases}\end{aligned} \tag{4.47}$$

In the second case, the spectrometer performs a Fourier transform of the fields with respect to t. The measured signal can be written as

$$\mathfrak{S}_{HSPE}(\omega_3,T,\tau,\phi) = \int_{-\infty}^{\infty} \mathfrak{S}_{HSPE}(t,T,\tau,\phi)e^{-i\omega_3 t}dt \tag{4.48}$$

We further Fourier transform $\mathfrak{S}_{HSPE}(\omega_3,T,\tau,\phi)$ with respect to the delay between the first two pulses τ to obtain the 2D spectrum:

$$\mathfrak{S}_{2D}(\omega_3,T,\omega_1,\phi) = \int_{-\infty}^{\infty} \mathfrak{S}_{HSPE}(\omega_3,T,\tau,\phi)e^{\mp i\omega_1\tau}d\tau \tag{4.49}$$

where "$\mp$" is for rephasing and non-rephasing diagrams respectively, because for pathways R_2 and R_3, the system interacts with a field of positive frequency ω_1, as opposed to a field of negative frequency $-\omega_1$ for R_1 and R_4.

Following the same argument in Section 4.1.4, we note that the response function for the pure homogeneous rephasing diagrams is:

$$R_2 = R_3 \propto e^{-i\omega_1 t_1}e^{-\Gamma_{ge}t_1}e^{i\omega_3 t_3}e^{-\Gamma_{eg}t_3} \tag{4.50}$$

and for the pure homogeneous non-rephasing diagrams is:

$$R_1 = R_4 \propto e^{i\omega_1 t_1}e^{-\Gamma_{eg}t_1}e^{i\omega_3 t_3}e^{-\Gamma_{eg}t_3} \tag{4.51}$$

Combining Eqs. 4.48, 4.49, 4.50 and 4.51, the Fourier transform of Eqs. 4.50

and 4.51 renders:

$$\begin{aligned} R_2(\omega_1,\omega_3) = R_3(\omega_1,\omega_3) &\propto \frac{1}{i(\omega_1-\omega)-\Gamma_{ge}} \cdot \frac{1}{-i(\omega_3-\omega)-\Gamma_{eg}} \\ R_1(\omega_1,\omega_3) = R_4(\omega_1,\omega_3) &\propto \frac{1}{-i(\omega_1-\omega)-\Gamma_{eg}} \cdot \frac{1}{-i(\omega_3-\omega)-\Gamma_{eg}} \end{aligned} \tag{4.52}$$

The rephasing and non-rephasing 2D spectra contain both absorptive and dispersive contributions and show a phase-twisted line shape along the diagonal and anti-diagonal axes respectively [71]. When the rephasing and non-rephasing spectra are added (i.e. $R(\omega_1,\omega_3) = \sum_{n=1,4} R_n(\omega_1,\omega_3)$), the dispersive features will cancel each other to yield a purely absorptive spectrum [71].

4.2.4 Collinear measurement

Another approach to measure photon echo is the phase-locked collinear measurement (Figure 4.3(A)) [28]. As shown in Eq. 4.41, the stimulated photon echo signal has phase dependence $-\phi_1+\phi_2+\phi_3$. This means that different Liouville pathways have unique phase dependence on the excitation pulses. Therefore, in the collinear geometry, even though we cannot isolate pathways by phase-matching, selected pathways can be eliminated with phase-cycling [72].

The external field in the collinear measurement is comprised of three phase-locked pulses with delays τ_1 and τ_2

$$\tilde{\mathbf{E}}(t) = \mathbf{E}_1(t)e^{i(\omega_0 t-\phi_1)} + \mathbf{E}_2(t-\tau_1)e^{i(\omega_0 t-\phi_2)} + \mathbf{E}_3(t-\tau_1-\tau_2)e^{i(\omega_0 t-\phi_3)} + c.c. \tag{4.53}$$

where $E_j, j = 1,2,3$ is the temporal envelope of the jth incident pulse. Each pulse has an extra phase shift ϕ_j on top of the carrier phase $\omega_0 \cdot t$, where ω_0 is the central frequency of the pulses. If the pulses are generated by a pulse-shaper, the phase difference between two pulses ($\Delta\phi$) does not necessarily need to be the natural frequency of the light (ω_0) times the delay between the two pulse (ΔT), but can be shifted to a rotating frame at lower frequency. Because the pulses and the induced signal are collinear, the direction of the field does

not need to be specified.

In the collinear geometry, we are measuring multiple nonlinear process simultaneously, such as the pump-probe signal that involves excitation by two of the pulses, and the photon echo that comes from interaction with all three pulses. In the case of a photon echo process, at $t = 0$, the first pulse creates an optical coherence ρ_{ge} in the ground state density matrix ρ_{gg}, which then evolves according to the time evolution operator. At $t = \tau_1$, the second pulse interacts with the system twice, i.e. it serves simultaneously as the second and the third pulses in the FWM geometry with $T = 0$ and leaves the system in optical coherence ρ_{eg}. At delay $\tau_1 + \tau_2$, the third pulse converts the coherence back to a population of the excited-states [73]. Finally, a fluorescence signal orthogonal to the excitation wave vectors is measured as a function of τ_1 and τ_2. Because each nonlinear process has different phase dependence, by tailoring the relative phase between pulses, we can selectively eliminate signal from certain pathways.

We can express the population ρ_{ee} as a sum of contributions from all possible nonlinear pathways in a series of terms which have different dependence on phase of three pulses: $c_i(\phi_1, \phi_2, \phi_3)$, and each term has amplitude a_i [72]

$$\rho_{ee} \propto \sum_{i=1,} a_i c_i(\phi_1, \phi_2, \phi_3) e^{i\omega_1\tau_1} e^{i\omega_2\tau_2} \tag{4.54}$$

Here we follow the notations in [28] to label the phase-dependent population ρ_{ee} as $\rho_{\phi_1\phi_2\phi_3}$, where the phase ($\phi_1, \phi_2$, or ϕ_3) can be $X = 0$, $Y = \pi/2$, $\bar{X} = \pi$, and $\bar{Y} = 3\pi/2$. Note that X and Y refer to the pulses phases as been used in NMR conventions, but are not used to label the direction of the polarization of the light. It is obvious from the Feynman diagrams (R_2 and R_3 in Figure 4.2) that the photon echo signal has phase dependence $e^{i(-\phi_1+2\phi_2-\phi_3)}$. On the other hand, signals from other Liouville pathways have different phase dependence. For example, the pump-probe signal that involves only the first and the third pulses is independent of ϕ_1 and ϕ_2. Because each pathway has a unique phase-dependence, we can eradicate contributions from the pump-probe and keep the PLPP signal with phase-cycling. For example, in a two-step phase-cycling measurement, we take the difference between the two 2D spectra collected with $(\phi_1, \phi_2, \phi_3) = (0, 0, 0)$ and $(\pi, 0, 0)$. Because $\rho^{PE}_{XXX} = -\rho^{PE}_{\bar{X}XX}$, the amplitude

of the photon echo peaks is doubled in the two-step phase-cycling signal ρ_2:

$$\rho_2 = \rho_{XXX} - \rho_{\bar{X}XX} \tag{4.55}$$

while the pump-probe signal is eliminated in the light of $\rho^{PP}_{XXX} = \rho^{PP}_{\bar{X}XX}$. A 16-step phase-cycling ρ_{16}, therefore, can remove all other peaks in a 2D spectrum but the photon echoes [72]:

$$\begin{aligned}\rho_{16} &= \rho_{XXX} - \rho_{XX\bar{X}} - \rho_{\bar{X}XX} + \rho_{\bar{X}X\bar{X}} - \rho_{YXY} + \rho_{YX\bar{Y}} + \rho_{\bar{Y}XY} - \rho_{\bar{Y}X\bar{Y}} \\ &+ i(\rho_{\bar{X}X\bar{Y}} - \rho_{\bar{X}XY} + \rho_{XXY} - \rho_{XX\bar{Y}} + \rho_{YXX} - \rho_{YX\bar{x}} - \rho_{\bar{Y}XX} + \rho_{\bar{Y}X\bar{X}})\end{aligned} \tag{4.56}$$

4.2.5 Hole burning spectroscopy

The third method of measuring the third-order response is hole burning (Figure 4.3(C)). It first excites a group of molecules within a broad inhomogeneous spectrum with a "spectrally narrow" pulse, and then measures the change in absorption of the second probe. The experimental configuration for hole burning is identical to pump-probe spectroscopy, but the first pulse is much longer than a femtosecond impulse, because a narrow bandwidth is crucial for selective excitation [63]. As a result, in hole burning spectroscopy, the temporal resolution is compromised in order to achieve a good spectral resolution. Feynman diagrams representing different pathways for the hole burning measurement are shown in Figure 4.4.

From Eq. 4.41, the hole burning signal can be described as:

$$\begin{aligned}\mathfrak{S}^{(3)}_{HB}(T) &\propto \frac{2}{\hbar^3}\,\mathrm{Re}\int_{-\infty}^{\infty} dt \int_0^{\infty} dt_3 \int_0^{\infty} dt_2 \int_0^{\infty} dt_1 \\ &\times \{[R_2(t_3,t_2,t_1) + R_3(t_3,t_2,t_1)]\chi(t_3-t_1)\mathbf{E}_2^*(t-T)\mathbf{E}_2(t-T-t_3) \\ &\times \mathbf{E}_1(t-t_3-t_2)\mathbf{E}_1^*(t-t_3-t_2-t_1)\exp[i\omega_2 t_3 - i\omega_1 t_1] \\ &+ [R_1(t_3,t_2,t_1) + R_4(t_3,t_2,t_1)]\chi(t_3+t_1)\mathbf{E}_2^*(t-T)\mathbf{E}_2(t-T-t_3) \\ &\times \mathbf{E}_1^*(t-t_3-t_2)\mathbf{E}_1(t-t_3-t_2-t_1)\exp[i\omega_2 t_3 + i\omega_1 t_1]\}\end{aligned} \tag{4.57}$$

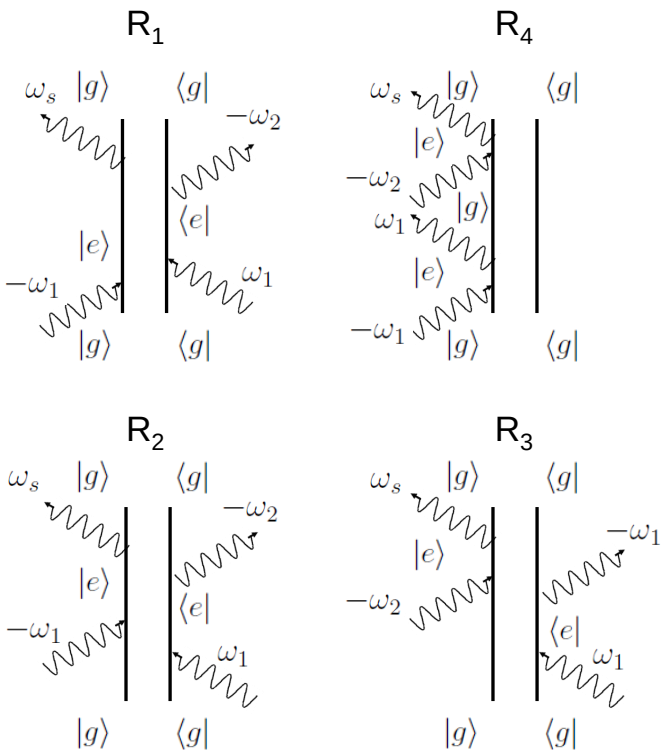

Figure 4.4: Liouville pathways for pump-probe and hole burning spectroscopy.

4.2.6 Phase-locked pump-probe spectroscopy

The last approach we introduce in this chapter, phase-locked pump-probe (PLPP) spectroscopy, is the one we implemented in the lab. It can be thought of as a three-pulse pump-probe absorption measurement carried out with a pair of phase-locked pump pulses and optical heterodyne detection. Because the first two pulses are collinear, $\boldsymbol{k}_1 = \boldsymbol{k}_2$, PLPP measures the sum of equally weighted rephasing and non-rephasing signals, and obtains an absorptive 2D spectrum [71]. A positive signal represents a decrease in the probe absorption in the presence of the pump caused by ground state bleaching (GSB), while a negative spectrum corresponds to an increase in the probe absorption due to excited-state absorption (ESA). From Eq. 4.41, the induced third-order polarization in PLPP spectroscopy is:

$$\begin{aligned}
& \tilde{\mathbf{P}}^{(3)}_{PLPP}(t,T,\tau,\phi) \\
= \; & \left(\frac{-i}{\hbar}\right)^3 \int_0^\infty dt_3 \int_0^\infty dt_2 \int_0^\infty dt_1 \\
\times \; & \{[R_2(t_3,t_2,t_1) + R_3(t_3,t_2,t_1)]\chi(t_3-t_1)\mathbf{E}_3(t-\tau-T-t_3) \\
\times \; & \mathbf{E}_2(t-\tau-t_3-t_2)\mathbf{E}_1^*(t-t_3-t_2-t_1)\exp[i\omega_3 t_3 - i\omega_1 t_1 - i\phi] \\
+ \; & [R_1(t_3,t_2,t_1) + R_4(t_3,t_2,t_1)]\chi(t_3+t_1)\mathbf{E}_3(t-\tau-T-t_3) \\
\times \; & \mathbf{E}_2^*(t-\tau-t_3-t_2)\mathbf{E}_1(t-t_3-t_2-t_1)\exp[i\omega_3 t_3 + i\omega_1 t_1 + i\phi]\}
\end{aligned} \tag{4.58}$$

where $\phi \equiv \phi_1 - \phi_2$ is the relative phase between pulse$_1$ and pulse$_2$.

The third pulse $\tilde{\mathbf{E}}_3$ served simultaneously as the third excitation field and the local oscillator. Empirically, we direct the light into a spectrometer, which performs a Fourier transform with respect to t and measures the superposition of $\tilde{\mathbf{E}}_3$ and the new field generated by $\tilde{\mathbf{P}}^{(3)}_{PLPP}$. From Eqs. 4.33, 4.45, 4.48, and 4.58, the measured spectrum is:

$$\begin{aligned}
& \mathfrak{S}^{(3)}_{PLPP}(\omega_3,T,\tau,\phi) \propto \mathrm{Im}[\mathbf{E}_3^*(\omega)\mathbf{P}^{(3)}_{PLPP}(\omega_3,T,\tau,\phi)] \\
\propto \; & \mathrm{Re}[\mathbf{E}_3^*(\omega)[(R_2(\omega_3,T,\tau) + R_3(\omega_3,T,\tau))e^{-i\phi_{12}} \\
+ \; & (R_1(\omega_3,T,\tau) + R_4(\omega_3,T,\tau))e^{i\phi_{12}}]]
\end{aligned} \tag{4.59}$$

where $\mathbf{E}_3^*(\omega)$ and $\mathbf{P}^{(3)}_{PLPP}(\omega_3, T, \tau, \phi)$ are Fourier transform of $\mathbf{E}_3^*(t)$ and $\mathbf{P}^{(3)}_{PLPP}(t, T, \tau, \phi)$ respectively.

Note that any noise in the field $\tilde{\mathbf{E}}_3$ will write onto the measured signal. So instead of increasing the S/N, this heterodyne detection actually introduces an non-negligible amount of noise. This is why we set up the fourth beam, the reference, in the setup to account for any common noise in the laser pulses. Details of the reference beam were described in Section 2.4 .

In this geometry, besides the rephasing and non-rephasing process, the pump-probe absorption that involves the interactions with one of pump pulses and once with the probe is also being measured. The actual signal collected has contribution from PLPP and pump-probe absorption ($\mathfrak{S}_{pp_1}$, $\mathfrak{S}_{pp_2}$):

$$\mathfrak{S}(\omega_3, T, \tau, \phi) = \mathfrak{S}^{(3)}_{PLPP}(\omega_3, T, \tau, \phi) + \mathfrak{S}_{pp_1}(\omega_3, \tau + T) + \mathfrak{S}_{pp_2}(\omega_3, T) \quad (4.60)$$

Since the two transient absorption signals, unlike the PLPP signal, are independent of the phase between the two pump pulses ϕ, they can be eliminated with phase-cycling. We follow the same procedure as described in [32] to remove the TA signal. TA does not depend on the relative phase between $\tilde{\mathbf{E}}_1$ and $\tilde{\mathbf{E}}_2$, i.e. $\mathfrak{S}_{pp}(\phi = 0) = \mathfrak{S}_{pp}(\phi = \pi)$. On the other hand, the PPLP signal $\mathfrak{S}^{(3)}_{PLPP}$ flips sign when ϕ and ϕ' are π out of phase, i.e. $\mathfrak{S}^{(3)}_{PLPP}(\phi = 0) = -\mathfrak{S}^{(3)}_{PLPP}(\phi = \pi)$. As a result, subtracting $\mathfrak{S}(\phi = \pi)$ from $\mathfrak{S}(\phi = 0)$ removes the transient absorption but makes the PLPP signal twice as large. We collect two spectra $\mathfrak{S}(\phi_1 = 0, \phi_2 = 0)$ and $\mathfrak{S}(\phi_1 = 0, \phi_2 = \pi)$ sequentially at each delay τ, and obtain our final spectrum by combining these two measurements:

$$\mathfrak{S}^{(3)}_{PLPP}(\omega_3, T, \tau) = \mathfrak{S}(\phi_1 = 0, \phi_2 = 0) - \mathfrak{S}(\phi_1 = 0, \phi_2 = \pi) \quad (4.61)$$

We further Fourier transform Eq. 4.61 with respect to the delay between the first two pulses: τ to obtain the 2D spectrum $\mathfrak{S}^{(3)}_{PLPP}(\omega_3, T, \omega_1)$. A series of $\mathfrak{S}^{(3)}_{PLPP}(\omega_3, T, \omega_1)$ are collected at different T to probe the excited-state dynamics of the molecules. In later sections, T will be denoted as the pump-probe delay. In this geometry, because the two pump pulses generated by the pulse shaper are identical, we cannot distinguish if pulse_1 is the leading pulse, i.e. $\tau > 0$, or vice versa. Therefore, the spectrum measured by the

spectrometer is symmetric with respect to $\tau = 0$, i.e. $\mathfrak{S}^{(3)}_{PLPP}(\omega_3, T, \tau) = \mathfrak{S}^{(3)}_{PLPP}(\omega_3, T, -\tau)$. Because $\mathfrak{S}^{(3)}_{PLPP}(\omega_3, T, \tau)$ is real and symmetric, its Fourier transform spectrum $\mathfrak{S}^{(3)}_{PLPP}(\omega_3, T, \omega_1)$ is also real. This is consistent with the fact that PLPP is measuring equally weighted rephasing and non-rephasing signals and should yield an absorptive spectrum [71].

4.2.7 Recovering rephasing and non-rephasing spectra from PLPP measurements

Phase-cycling also helps to retrieve the rephasing and non-rephasing spectra from PLPP measurements. Set the phase between the pump pulse in Eq. 4.59 as 0 and $\pi/2$:

$$\begin{aligned}
&\mathfrak{S}^{(3)}_{PLPP}(t, T, \tau, 0) \propto R^{(R)}(t, T, \tau) + R^{(NR)}(t, T, \tau) \\
&\mathfrak{S}^{(3)}_{PLPP}(\omega_3, T, \tau, \pi/2) \propto -iR^{(R)}(t, T, \tau) + iR^{(NR)}(t, T, \tau)
\end{aligned} \tag{4.62}$$

where $R^{(R)}(\omega_3, T, \tau)$ is the rephasing response function, with $R^{(R)} = R_2 + R_3$, and $R^{(NR)}(\omega_3, T, \tau)$ is the non-rephasing response function, with $R^{(NR)} = R_1 + R_4$. The rephasing and non-rephasing response function can be retrieved by combing $\mathfrak{S}^{(3)}_{PLPP}(\omega_3, T, \tau, \phi)$ at $\phi = 0, \pi/2$:

$$\begin{aligned}
R^{(R)}(t, T, \tau) &\propto \mathfrak{S}^{(3)}_{PLPP}(t, T, \tau, 0) + i\mathfrak{S}^{(3)}_{PLPP}(t, T, \tau, \pi/2) \\
R^{(NR)}(t, T, \tau) &\propto \mathfrak{S}^{(3)}_{PLPP}(t, T, \tau, 0) - i\mathfrak{S}^{(3)}_{PLPP}(t, T, \tau, \pi/2)
\end{aligned} \tag{4.63}$$

Because there will be no third-order polarization if pulse_3 interacts with the sample before the pump pulses, to recover $\mathfrak{S}^{(3)}_{PLPP}(t, T, \tau, \phi)$ from $\mathfrak{S}^{(3)}_{PLPP}(\omega_3, T, \tau, \phi)$, causality has to be enforced after we performed the inverse Fourier transform with respect to ω_3, i.e., set $\mathfrak{S}^{(3)}_{PLPP}(t, T, \tau, \phi) = 0$ for $t < 0$. The 2D spectrum for the rephasing/non-rephasing process can be covered by Fourier transform $R^{(R)}(t, T, \tau)$ and $R^{(NR)}(t, T, \tau)$ along t and τ.

4.2.8 Generating phase-locked pulses with a pulse shaper

In Chapter 2, we mention briefly that phase-locked pulses are generated with a pulse-shaper, that we apply a programmable amplitude/phase mask with an acousto-optic modulator (AOM) to shape light in the frequency domain. In the time domain, two light pulses with delay τ can be expressed as:

$$\begin{aligned} \tilde{\mathbf{E}}_1(t) &= \mathbf{A} e^{-\frac{t^2}{\tau_p^2}} e^{i(\omega_0 t+\phi_1)} + c.c. \\ \tilde{\mathbf{E}}_2(t) &= \mathbf{A} e^{-\frac{(t-\tau)^2}{\tau_p^2}} e^{i(\omega_0 t+\phi_2)} + c.c. \end{aligned} \tag{4.64}$$

where $1.18\tau_p$ is the FWHM of the pulse duration. In the frequency domain, the pulse are:

$$\begin{aligned} \tilde{\mathbf{E}}_1(\omega) &= \mathbf{A} e^{i\phi_1(\omega)} e^{-\frac{(\omega-\omega_0)^2}{\Delta\omega^2}} + c.c. \\ \tilde{\mathbf{E}}_2(\omega) &= \mathbf{A} e^{i\phi_2(\omega)} e^{-\frac{(\omega-\omega_0)^2}{\Delta\omega^2}} + c.c. \end{aligned} \tag{4.65}$$

For pulses generated by a Michelson interferometer, $\phi_2(\omega) = \phi_1(\omega) + \omega \cdot \tau$, but for pulses generated by a pulse-shaper, the central frequency can be shifted to a rotating frame $\omega' = \omega - \omega_R$ by the following procedure. From Eq. 2.2, the two acoustic waveforms to generate two laser pulses with delay τ in a rotating frame are:

$$\begin{aligned} S_1(t_{ac}) &= \frac{1}{2} e^{i(2\pi f t_{ac}+\phi_1)} \\ S_2(t_{ac}) &= \frac{1}{2} e^{i(2\pi f t_{ac}+\phi_2)} \\ \phi_2(\omega) &= \phi_1(\omega) + \omega' \cdot \tau = \phi_1(\omega) + (\omega - \omega_R) \cdot \tau \end{aligned} \tag{4.66}$$

Because the acoustic wave is static to the femtosecond laser pulse, t_{ac} can be thought of as different pixels in the AOM crystal, and different colors in the light are mapped to different pixels in the crystal:

$$\omega = k \cdot t_{ac} + C \tag{4.67}$$

where k and C are empirical constants. Combining Eqs. 4.66 and 4.67, the phase difference between the acoustic waveforms is:

$$\begin{aligned}\phi_2(\omega) &= \phi_1(\omega) + (\omega - \omega_R)\cdot\tau \\ &= \phi_1(\omega) + (k\cdot t_{ac} + C - k\cdot t_R - C)\cdot\tau \\ &= \phi_1(\omega) + k\cdot(t_{ac} - t_R)\tau \end{aligned} \tag{4.68}$$

which means that we can shift the measurement to a rotating frame by simply moving the starting point of the acoustic carrier wave to a desired AOM pixel (light frequency).

After introducing various ultrafast nonlinear spectroscopy, in the following sections, we will introduce results of ultrafast pump-probe and 2D spectroscopy measurements on DNA bases.

4.3 Ultrafast measurements on DNA bases

DNA, RNA and proteins are the three building blocks of all known forms of life. For all living organisms except RNA viruses, their genetic information for development and functioning are stored in the DNA. DNA and RNA are very similar in structure, both consisting of long strands of simple nucleotide units. Each nucleotide contains a nucleobase (which will be abbreviated as DNA/RNA base or simply as base in later sections), a ribose sugar, and a phosphate group. The information in DNA is stored as a code by four bases: adenine (A), thymine (T), guanine (G), and cytosine (C). In RNA, uracil (U) substitutes thymine as one of the four bases. Long before the existence of life and when there was no ozone layer around Earth to block UV radiation from the Sun, the DNA/RNA bases emerged at that time were exposed to strong UV radiation. However, despite the fact that DNA bases absorb strongly in the UV (for example, Figure 4.5 shows the UV-Vis spectrum of adenine and uracil), from the simple fact that life successfully evolved from DNA bases, DNA/RNA bases are highly stable to photochemical decay [35, 74, 75]. In recent years, because of increasing harmful solar radiation caused by ozone layer depletion, there is growing interest in studying DNA excited-state dynamics under UV radiation. Understanding the relaxation dynamics of DNA bases would be

the foundation to elucidate the photophysical properties of more complicated molecules like DNA.

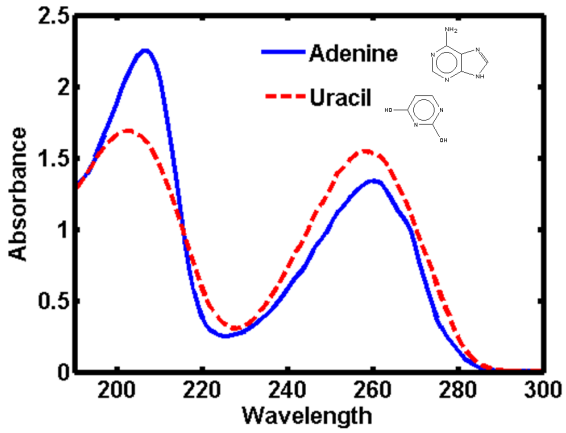

Figure 4.5: Adenine and Uracil UV-Vis spectrum. Both absorbs strongly in the UV.

Generally, excited-states of molecules are more reactive than the ground states, and when the DNA bases are driven to singlet excited-states by the UV radiation, they become prone to damage. For example, photolesions like pyrimidine dimers can form after excitation, which alter the structure of DNA and consequently inhibit polymerases and replication. This interference can lead to mutations, genomic instability, and carcinogenesis [76]. Fortunately, the quantum yields of photolesion formation are generally much less than 1% [75], and there exist non-adiabatic processes to convert the electronic energy to vibrational energy on ultrafast timescales. Early literature frequently described the DNA bases as "nonfluorescent" because of low fluorescence yield, which indicates that the bases have very short life time. Recent studies suggest that the excited-states are deactivated back the ground state S_0 through nonradiative decay by internal conversion. It has been suggested that there exist low-lying S_0-$S_{\pi\pi^*}$ conical intersections (where the electronic potential energy surfaces (PESs) cross) which provide effective channels for deactivation of the electronic excitation [51] and bring the molecule from the excited-state back to the ground state rapidly. Here, $S_{\pi\pi^*}$ (and $S_{n\pi^*}$) are used to describe the character of the states, and singlet excited-states are denoted as S_i where i=1,2 is the order of the state. Prior ultrafast studies on the DNA bases in the gas phase include resonance-enhanced multi-photon ionization (REMPI) [77],

pump-probe mass spectrometry [78], and time-resolved photoelectron spectroscopy [79]. For measurements on DNA in solution that are directly related to our 2D measurement on adenine and uracil in solution, there are UV transient absorption [74, 80–85] and femtosecond fluorescence upconversion [85–91].

Ultrafast TA and FU measurements on DNA/RNA in solution have shown that population in the first bright singlet excited-state $S_{\pi\pi^*}$ decays rapidly to the ground state S_0 on sub-picosecond timescales via conical intersections (CIs). Other relaxation pathways on the picosecond time scale include decay from $S_{\pi\pi^*}$ to a dark state $S_{n\pi^*}$, which can also lead to S_0 via non-adiabatic coupling (i.e. conical intersections). FU measurements on uracil [88] and adenine [87] show a rapid decay in the fluorescence for both molecules (100 and 250 fs for uracil and adenine respectively), with the adenine fluorescence also containing a slow component (8 ps lifetime). The existent of the slower component indicates that adenine has a flat excited-state PES, so it takes longer for the excited wavepacket to decay to the ground state. TA measurements on uracil and adenine derivatives [81–83] have shown ultrafast decay on a similar time scale which were interpreted in terms of rapid (few hundred fs) relaxation to the ground electronic state, followed by vibrational cooling on > 1 ps timescales.

In this thesis, we would like to provide a complimentary view of DNA base excitation relaxation dynamics with 2D spectroscopy on DNA bases in aqueous solutions.

4.4 2D spectroscopy on adenine and uracil in aqueous solutions

4.4.1 Background subtraction

As mentioned in Section 2.4, there is strong linear and nonlinear UV absorption by the solvent and fused silica windows on the sample holder, which can be several times larger than the DNA/RNA signal and mask the real DNA dynamics near short pump-probe delays.

For delays less than 125 fs, there is a significant solvent (water) contribution

to the 2D spectrum. To isolate the DNA response from background water signal, we measure the DNA + water ($S_{DNA+water}$) and water (S_{water}) 2D spectrum separately at each delay, and subtract the water contribution from $S_{DNA+water}$. The water subtraction is complicated by the fact that the average intensity of the pump pulse sequence in DNA solutions is less than the average intensity of the pump pulse sequence in pure water due to absorption of the pump pulses by the DNA. As a result, for a given input pump intensity, the solvent sees less light in DNA solution than in pure water. To mimic the lowered pump intensity seen by solvent, we made the measurements on water alone at a reduced pump intensity where the ESA at zero time delay was roughly the same for pure solvent and for DNA solution. This is, however, still not adequate for accurately extracting the water contribution, because the measured signal, $S_{DNA+water}$, is a sum of S_{water} and S_{DNA} contributions. Therefore, in order to refine the water subtraction, we looked to features in the spectrum outside the pump or probe bandwidth which are due to water alone, and do not have a contribution from the DNA signal. We multiplied S_{water} by a constant factor k before subtracting it from $S_{DNA+water}$, with the factor chosen to minimize the features outside the pump and probe spectra:

$$S_{DNA} = S_{DNA+water} - k \times S_{water} \tag{4.69}$$

Figure 4.6 demonstrates how we adjust k until the spectrum looks smooth and vertical stripes outside of pump spectrum (37700 $cm^{-1} \sim$ 38300 cm^{-1}) are minimized at the optimal k value. Each panel of Figure 4.6 represents S_{DNA} calculated with a different k. When either too little (Figure 4.6(A), $k = 0.4$) or too much (Figure 4.6(C), $k = 1.1$) S_{water} has been removed from $S_{DNA+water}$, vertical absorption (Figure 4.6(A): region above Frequency 1 = 38300 cm^{-1}) or emission (Figure 4.6(C): region above Frequency 1 = 38360 cm^{-1}) stripes emerge from the spectrum. Only when we account for the right amount of water signal, S_{water}, (Figure 4.6(B), $k = 0.7$), does the DNA signal, S_{DNA}, look free of artifacts. This analysis is reinforced by Figure 4.7, which shows horizontal lineouts of the data shown in Figure 4.6 at a frequency of 38400 cm^{-1} (outside of the pump spectral bandwidth) for a range of k values. This plot shows that the unphysical absorption or emission feature is minimized for k=0.7.

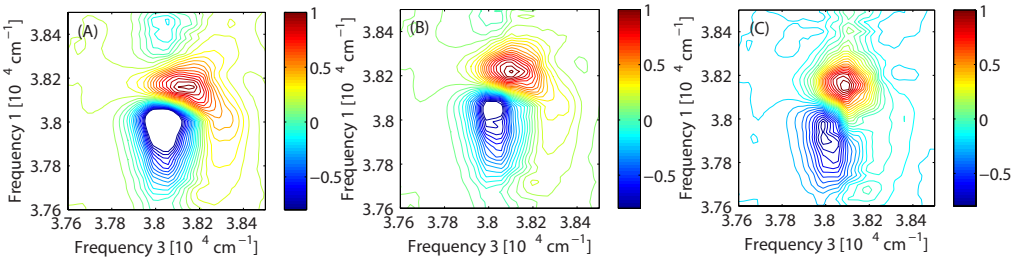

Figure 4.6: Adenine 2D spectrum at 60 fs subtracted with (A) k=0.4 (B) k=0.7 (C) k=1.1 X water 2D spectrum.

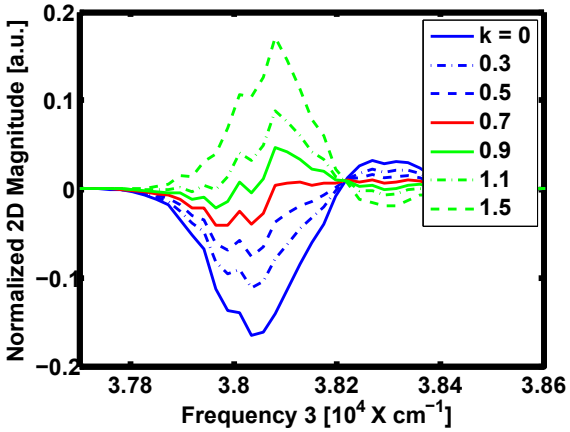

Figure 4.7: Horizontal lineouts of the data shown in Figure 4.6 at 38400 cm^{-1} for different k values.

4.4.2 Center of gravity (COG) and variance

Figure 4.8 and Figure 4.9 show adenine and uracil 2D spectra $\mathfrak{S}^{(3)}_{PLPP}$ individually, for pump-probe delays of 60, 125 (150 for uracil), 400 (500 for uracil) and 1000 fs. At delays below 100 fs, the spectrum shows evidence of both increased transmission and absorption of the probe - ground state bleaching (GSB) and excited-state-absorption (ESA) respectively. The ESA signal evolves rapidly with delay and is overwhelmed by the GSB signal at around 125 fs. After 150 fs, the DNA 2D spectrum contains a single GSB peak, with its magnitude rising until about 300 fs and then decaying gradually with the delay and only subtle changes in the shape of the peak taking place. This general behavior is common to several molecules that we have studied, including adenine, uracil, cytosine and NADH. The decay of the GSB signal is consistent with earlier TA measurements of adenine [83] which were interpreted in terms of relaxation via conical intersections (CIs) followed by vibrational cooling in the electronic ground state. A single peak in the spectrum is consistent with driving a single (homogeneously/inhomogeneously broadened) transition. The spectrum becomes structureless on a relatively short time scale as a result of dephasing and spectral diffusion caused by the solute-bath coupling [92]. As analysis of the long time dynamics (for delays greater than 500 fs) does not yield information beyond what is available with traditional pump probe measurements, we concentrate on dynamics within the the first few hundred femtoseconds.

In order to gain more insight into the molecular dynamics after 150 fs, we calculate the center-of-gravity (COG - the first moment of the distribution) and variance along diagonal and anti-diagonal axes of the GSB peaks at each delay. Previous 2D studies have interpreted oscillations in the ratio of diagonal to anti-diagonal FWHM of the 2D spectrum in terms of coherent wave packet motion on the excited-state PES [93]. Figure 4.10 shows the values for measurements and their averages over several sets of measurements made on separate days with separate solutions. We note that the COG and variance for adenine show little systematic variation with time delay, while the uracil data shows significant changes in both the COG and variance of the peak with time delay over the first few hundred femtoseconds.

In addition to the COG and variance, we show the integral of the 2D spectrum as a function of pump probe delay in order to compare the magnitude

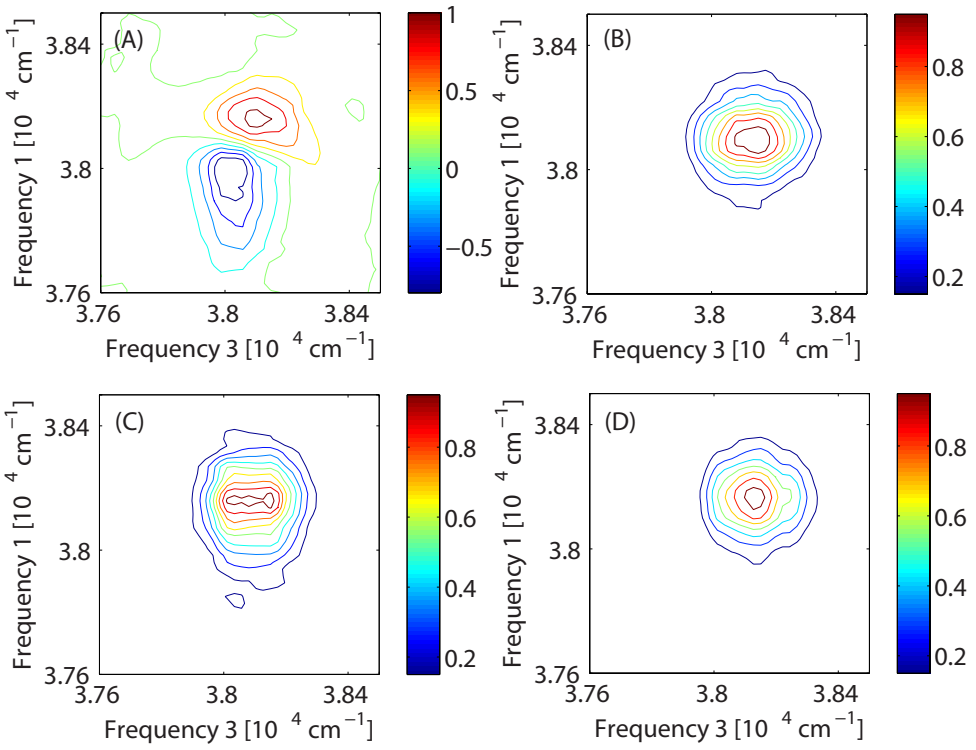

Figure 4.8: Adenine 2D spectrum at pump-probe delay = (A) 60 fs (B) 125fs (C) 400fs and (D) 1000 fs.

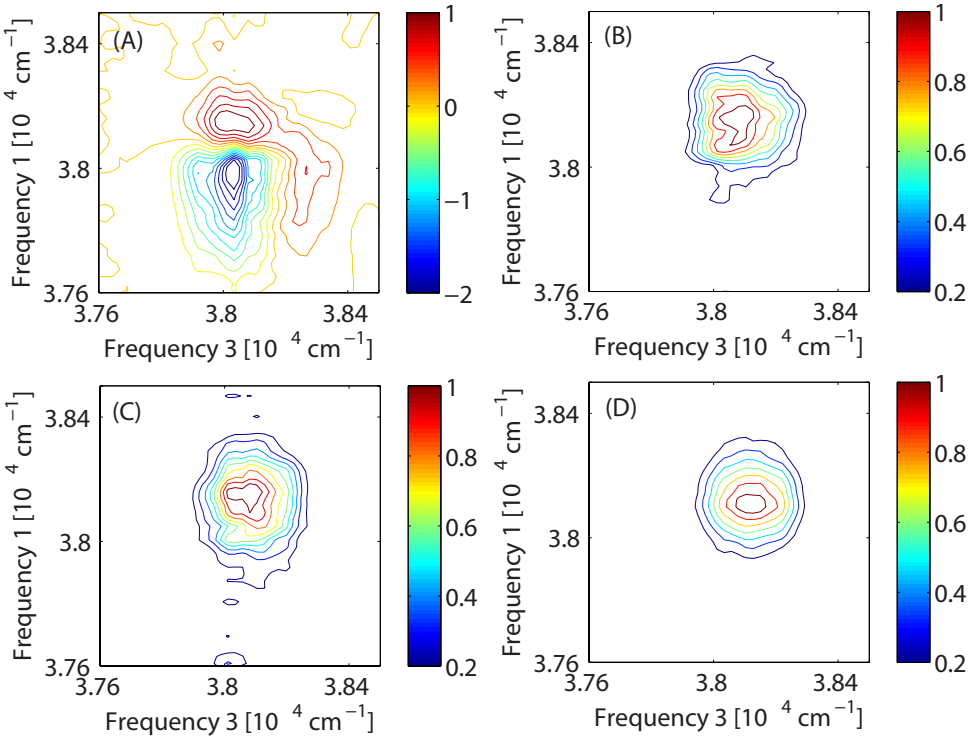

Figure 4.9: Uracil 2D spectrum at pump-probe delay = (A) 60 fs (B) 150fs, (C) 500fs and (D) 1000 fs.

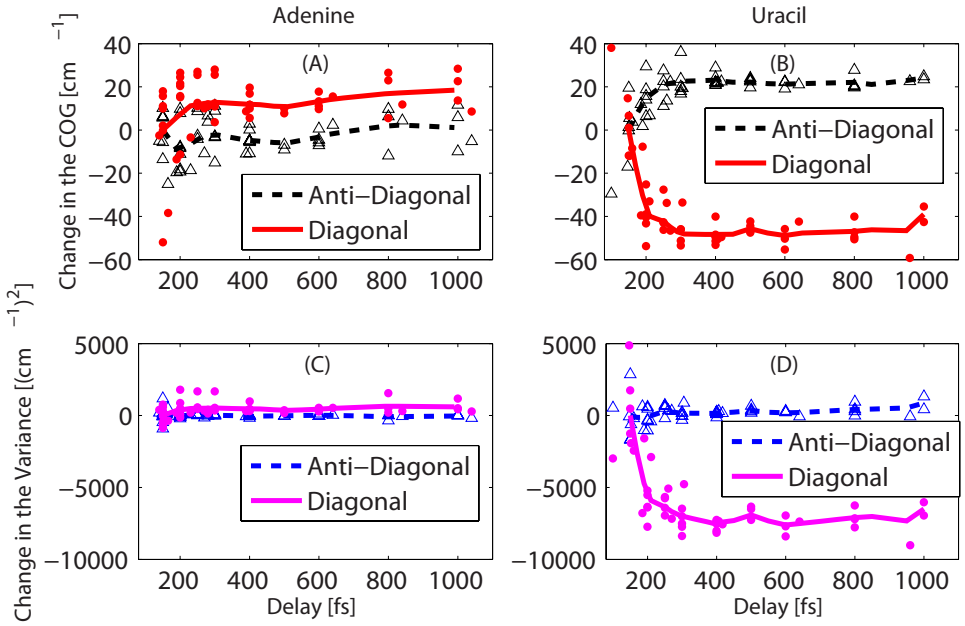

Figure 4.10: (A) COG of adenine along diagonal (solid) and anti-diagonal (dashed) axes. (B) COG of uracil along diagonal and anti-diagonal axes. (C) Variance of adenine along diagonal and anti-diagonal axes. (D) Variance of uracil along diagonal and anti-diagonal axes. Dots and triangles refer to measurements made on different days and lines are the average of different measurements.

of the ground state bleach signal with the COG as a function of time delay over the first picoseconds. This is shown in Figure 4.11.

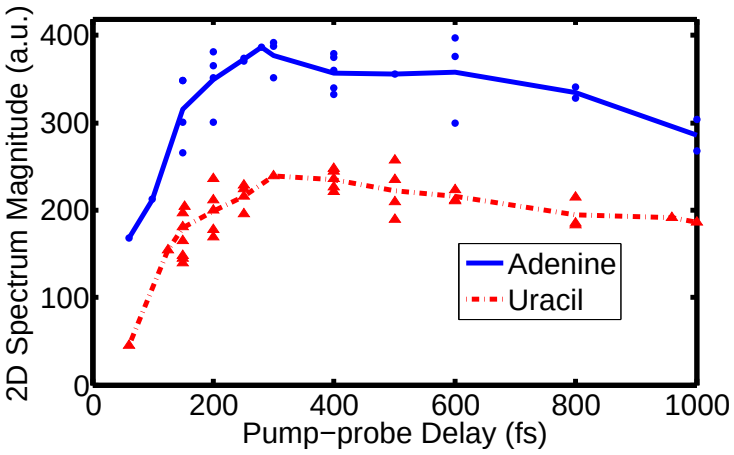

Figure 4.11: Magnitude of the 2D signal as a function of pump probe delay for adenine and uracil. The 2D spectrum was integrated over the region of the peak and is shown for several different measurements (dots: adenine, and triangles: uracil) as a function of delay along with the average (solid line: adenine and dashed line: uracil) of different measurements (made on different days).

4.4.3 UV-UV pump-probe measurements on adenine and uracil vapor

We also compare our 2D results with other methods measuring relaxation dynamics of DNA bases. Figure 4.12 shows molecular ion yield of adenine and uracil as a function of pump probe delay (data courtesy of Marija Kotur). The molecular ionization signal was produced by focusing the same UV pump and probe pulses into an effusive molecular beam in a time-of-flight mass spectrometer and measuring the parent ion yields as a function of pump probe delay. Here the pump and probe beams have a much tighter focus and higher intensities (more than two orders of magnitude) than those in the 2D measurement to produce enough ion yields for the measurement. Details on the uracil molecular beam source can be found in [94].

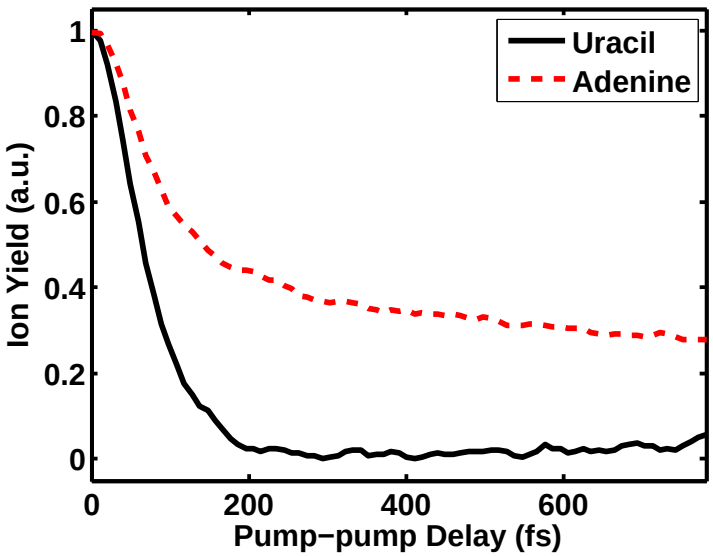

Figure 4.12: Adenine (solid curve) and uracil (dashed curve) ion yields vs pump probe delay. Adenine signal has a fast decay with lifetime $\sim$ 150 fs and another much slower component. Uracil signal decays within 100 fs. Data courtesy of Marija Kotur.

4.4.4 Discussion

Adenine and uracil 2D spectra show very similar features at first sight. Both suggest the existence of ESA for early time delays and GSB at longer delays, while only uracil exhibits systematic changes in COG and variance for the 2D spectra. We interpret the evolution of the ESA and GSB spectrum in terms of wave packet motion on the excited-state potential. As illustrated in Figure 4.13, at Franck Condon point, the minimum energies required for vertical ionization are about 8.4 eV and 9.5 eV ($\pm$0.3 eV) for adenine and uracil respectively [94–97]. This implies that both molecules can be ionized from the excited-state near FC point by absorbing another UV photon (4.77 eV) from the probe pulse. However, as the wave packet moves away from the FC point, the IP rises rapidly [94], and absorption from excited-states becomes less favorable if it is driven by ionization (or absorption to Rydberg states). As a result, ESA for adenine and uracil both decrease gradually with pump probe delay. At delays $<$ 100 fs, negative signals in adenine and uracil 2D spectra dwindle down towards lower frequencies and are replaced by positive signals before 110 fs. It might be surprising that ESA takes place at lower

frequencies and GSB occurs at higher frequencies. From the perspective of the wave packet moving down on $S_{\pi\pi^*}$ and the IP increasing, one might expect that the ESA would occur at higher transition frequencies. However, the 2D spectrum contains both GSB (S_0 to the first bright state, $S_{\pi\pi^*}$) and ESA ($S_{\pi\pi^*}$ to S_n or D_0 - the ground (doublet) state of the ion) with their relative magnitudes depending on the the instantaneous detuning and transition dipole moments as the wave packet evolves on the excited-state. Initially, strong ESA dominates the 2D spectrum, as it diminishes away because of growth in IP at longer delays that no longer favors $S_{\pi\pi^*}$ to S_n transitions, positive GSB signals start to prevail in the 2D spectrum.

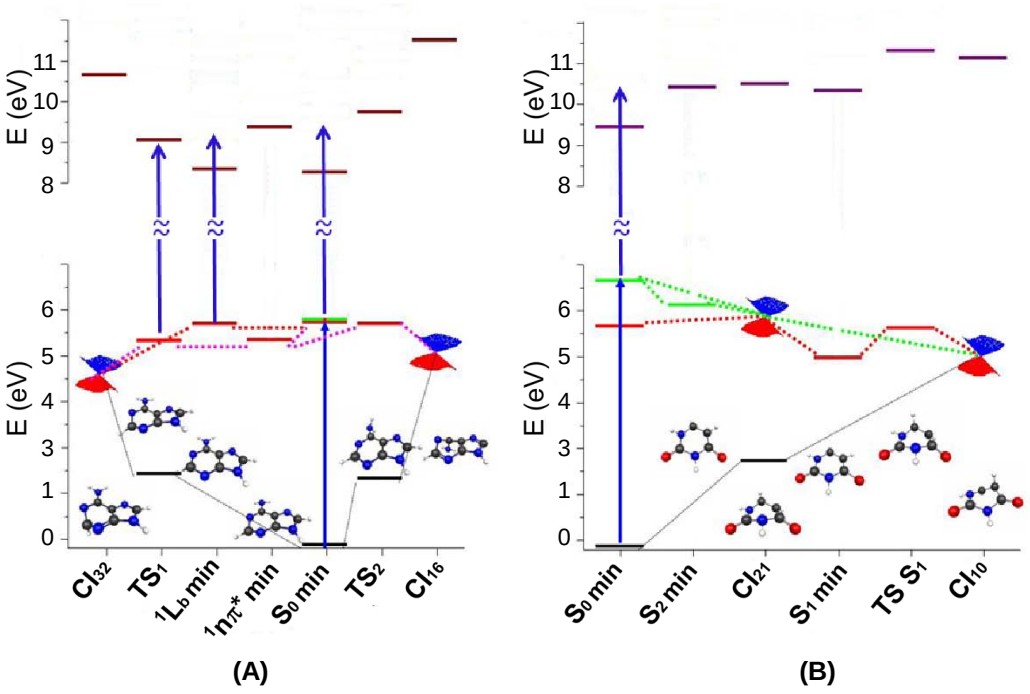

Figure 4.13: Neutral and ionic energies of (A) adenine and (B) uracil. Lower panel: Energies for neutral states [58, 98]. Black: ground state, red: S_1 state, green: S_2 state. Upper panel: Energies for the lowest-laying ionic state (D_0). For adenine, $S_{\pi\pi^*}$ is the S_1 state, and for uracil, $S_{\pi\pi^*}$ is the S_2 state. Dotted lines are used to mark predicted connections between states. Note that the theoretical $S_0 \rightarrow S_{\pi\pi^*}$ excitation energies are overestimated compared to the experimental measurements. Calculations courtesy of Spiridoula Matsika.

Even though adenine and uracil 2D spectra are both dominated by the GSB signal at delays longer than 150 fs, subtle changes in the two GSB peaks

reveal different excited-state dynamics for adenine and uracil. The COG of the uracil 2D peak along the diagonal axis (Figure 4.10(B)) shifts to lower frequencies with delay, while that of adenine does not. We consider two separate mechanisms for the evolution of the COG in uracil, both of which suggest the same picture - the wave packet moves toward lower energy on the $S_{\pi\pi^*}$ potential energy surface as it leaves FC region. The first mechanism is competition between ESA and GSB. The ESA decays quickly as the wavepacket on $S_{\pi\pi^*}$ can no longer be excited to ionic or high lying neutral states because of an increasing $S_{\pi\pi^*}$ to S_n energy difference. The COG for the 2D lineshape naturally descends to lower frequencies as a negative contribution of ESA declines with delay. The peak in the 2D signal Figure 4.11 occurs at about the same time ($\sim$ 250 fs) as the COG stops evolving for uracil, which is consistent with this interpretation. However, we note that the peak in the 2D signal in adenine is unaccompanied by a change in the COG. This is not consistent with the changes in the COG being driven by competition between ESA and GSB. The second mechanism which may produce a change in the COG is a decrease in the $S_{\pi\pi^*} \rightarrow S_0$ transition energy with time delay. As the wavepacket moves down the $S_{\pi\pi^*}$ surface, the COG for GSB naturally shifts to lower frequencies because of the smaller energy difference of the $S_{\pi\pi^*} \rightarrow S_0$ transition.

While the magnitudes of adenine and uracil 2D spectrum both peak at $\sim$ 250 fs, only the uracil COG (along the diagonal) decays noticeably with delay over the range of delays for which we are able to calculate reliably. For adenine, there is no substantial variation in the COG from 150 to 1000 fs. This indicates that the $S_{\pi\pi^*}$ potential near the FC region is steeper for uracil than for adenine, and that the minimum on the $S_{\pi\pi^*}$ surface is shallower for adenine than it is for uracil. This is illustrated in Figure 4.14 and consistent with our collaborators' calculation and previous studies [56, 91, 99]. In calculation [94], the IP change (difference between $S_{\pi\pi^*}$ and D_0) for adenine between the FC region and the ^1L_b minimum is negligible (< 0.1 eV), but for uracil, the IP increases by 1.5 eV from the S_0 minimum to the S_2 minimum.

Each DNA base has a number of structural isomers formed by permuting hydrogen atoms among the set of heteroatoms. These isomers are called tautomers. In the gas phase, $\sim$ 99% of the adenine is in the form of 9H-adenine (Figure 4.15). In aqueous solutions, adenine exists mostly in the form

of 7H-adenine and 9H-adenine. Here we assume the adenine 2D signal comes mostly from 9H-adenine, since the fraction of the two tautomers, 7H-adenine and 9H-adenine, in aqueous solution is $\sim$ 22% and $\sim$ 78% respectively, and we observed a relatively fast decay in the ESA signal which agrees with the 9H-adenine signature which is much faster than the 7H-adenine excited-state lifetime [81, 87].

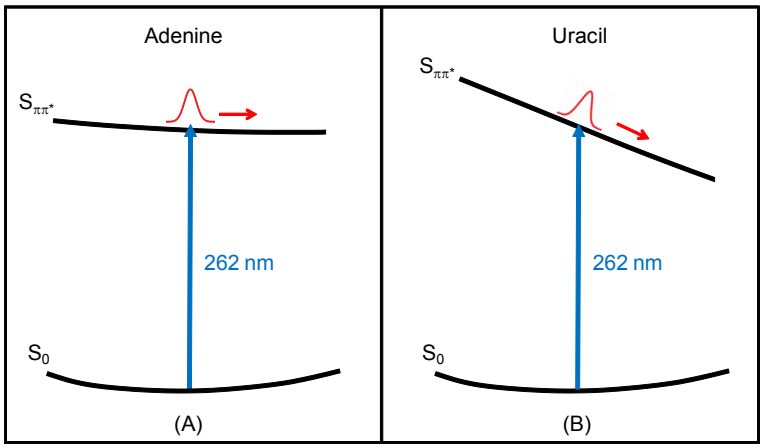

Figure 4.14: Cartoons illustrating the excited-state PES for (A) adenine and (B) uracil near the FC region. Based on our measurements, we argue that adenine has a flatter excited-state potential surface, $S_{\pi\pi^*}$, than for uracil. In adenine the energy difference between $S_{\pi\pi^*}$ and the ground state S_0 remains roughly constant as the wavepacket moves down the PES, whereas the excited-state potential surface for uracil is much steeper.

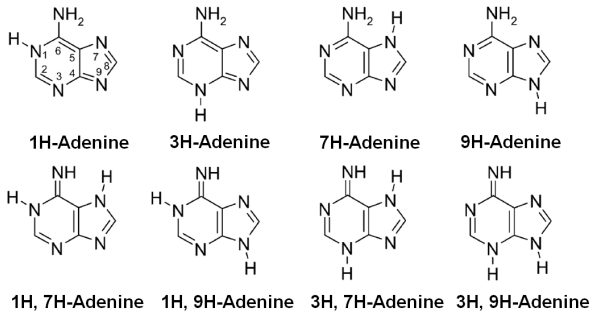

Figure 4.15: Adenine tautomers

Pump-probe measurements on adenine and uracil in the gas phase also support the above interpretation. Figure 4.12 shows the parent ion yields for adenine and uracil as a function of pump probe delay. The uracil signal

decays away by 200 fs while the adenine signal lasts much longer. The results are consistent with the interpretation that for uracil, the wavepacket moves on a steeper excited-state PES, and the ion yield decays rapidly when the IP increase beyond the probe photon energy as the wavepacket leaves the FC region. For adenine, the ion signal last longer because of a much flatter excited-state PES.

UV resonance Raman vibrational scattering spectroscopy measurements on uracil and 9-methyladenine (9-MeA) solutions [100–102] yield a similar picture of the excited state dynamics - i.e. that the excited state PES is flatter for adenine than for uracil. Previous work [103–106] has related the measured Raman intensities to displacements on the excited state surface by modeling the excited state potential in terms of a superposition of several displaced multi-dimensional harmonic potentials. While this is generally not true for a reactive system, for short-time dynamics, one can compare the resonance Raman measurements with our measurements by looking at the displacements quoted in the resonance Raman literature [100–102]. The intensity of a resonance Raman vibrational band coupled to the electronic excitation is directly proportional to the initial slope of the exited state PES along that vibrational coordinate [103–106]. The larger the excited-state PES slope along certain nuclear coordinate, the more intense the corresponding resonance Raman vibrational peak. The initial displacements depend mainly on the multidimensional slopes of the excited-state PES near the FC region, which are well determined by the Raman intensities [104]. For 9-MeA, 12 observed bands from 535 cm^{-1} to 1680 cm^{-1} after excitation at 266 nm have normalized displacement from 0.07 to 0.35 [101]. For uracil, the displacements for the 6 observerd modes from 579 cm^{-1} to 1664 cm^{-1} are at least twice as large, ranging from 0.3 to 0.74. These results indicate that the initial slope of the excited-state PES for uracil is larger than that of 9-MeA along all of the normal mode coordinates. The pump-probe measurement in the gas phase, the 2D spectroscopy measurements, and the resonance Raman spectroscopy results together provide a consistent picture of the slopes of the excited-state PESs of adenine and uracil near the FC region (Figure 4.14).

The persistence of the GSB signal for over 1 ps is consistent with uv-pump uv-probe TA measurements of Kohler [81–83], which have been interpreted in

terms of electronic relaxation followed by vibrational cooling on the ground electronic state. In looking at the variance in the GSB signal as a function of time for adenine and uracil, we note that the variance along the diagonal changes substantially for uracil although it does not change substantially with time delay for adenine. This could be due to different solvent interactions for the two molecules [107, 108]. One possible contribution to this difference is the presence of the dark $n\pi^*$ states, which have different locations relative to the bright states in adenine and uracil and are more sensitive to the solvent than the bright $\pi\pi^*$ states [84]. However, we note that this also could be due to the interplay between ESA and GSB in uracil, which might lead to changes in the variance. The fact that the diagonal variance and COG vary on similar timescales for uracil is consistent with this second explanation.

Chapter 5

Conclusion and Perspectives

In this thesis we explored coherent control spectroscopy in the weak field. In Chapter 3, we demonstrated that pulse shaping in conjunction with two-photon absorption can be used to distinguish between unbound and enzyme-bound NADH in solution. The control exploits different responses between the two forms to spectral phase (π phase flip) shaping. The response to the parameter scan is sensitive to the NADH-enzyme binding ratio which is a function of multiple parameters, e.g. NADH and enzyme concentrations and temperature. The results are promising for discrimination-based microscopy.

In Chapter 4, we developed the two-dimensional (2D) Fourier transform spectroscopy in the deep UV (262 nm) to study DNA excited state relaxation dynamics. We interpreted the 2D spectrum of single adenine and uracil bases in aqueous solution in terms of wavepacket motion on the excited state PES. Both the adenine and the uracil spectrum show excited-state absorption at short delays, and ground-state bleach beyond > 1 ps. At the Franck Condon point, the minimum energies required for vertical ionization are 8.4 eV and 9.5 eV ($\pm$0.3 eV) for adenine and uracil respectively. Both molecules can be ionized from the excited state near the FC point by absorbing another probe photon. As the wavepacket moves away from the FC point, ionization becomes less favorable and the the magnitude of ESA decreases. We also observed that only uracil COG (along the diagonal) decays noticeably with delay, but there is no substantial variation in adenine COG from delay 150 fs to 1 ps. There are two possible mechanisms for the change in the COG: the first is competition between ESA and GSB, and the second is a decrease in the $S_{\pi\pi^*}$

$\rightarrow S_0$ transition energy as the wavepacket moves down the excited-state PES. The first mechanism is more unlikely, because if the COG decreases to lower frequencies simply due less negative contribution from the ESA, there should be a comparable amount of change in both adenine and uracil. The second interpretation is that uracil has steeper excited state PES near the FC region, so the COG of its lineshape decays noticeably with delay, while the adenine has a flatter excited state PES, so the COG does not change substantially. Our results are consistent with gas-phase measurements and *ab initio* calculations.

While measurements have shown that single bases eliminate excess electronic energy non-radiatively on a subpicosecond time scale, the detailed relaxation dynamics of base pairs and DNA strands are not yet clear. Crespo-Hernandez *et al.* [109] suggest that vertical base stacking, not base pairing, determines the relaxation dynamics in single and double-stranded oligonucleotides comprised of adenine and thymine bases based on transient absorption measurements. Because 2D spectroscopy can identify coupled chromospheres, it would be especially powerful to study macro-molecules like DNA with 2D spectroscopy and provide a more comprehensive picture to energy transfer in DNA. Naturally, the next step for 2D spectroscopy could be to look at DNA base pairs and polymers dynamics.

Another future project is to extend to 2D two-color UV-blue spectroscopy. As shown in Figure 4.5, the absorption bandwidth of DNA bases is $30 \sim 40$ nm, much larger the bandwidth of currently available ultrafast UV lasers. Because of dispersion issues, generally, the bandwidth of a UV laser is less than 10 nm. It is hardly likely to cover multiple electronic transitions with a single UV laser. But it is possible to initiate the transition from the ground (S_0) to the second bright state (S_2) with the third harmonic from a Ti:sapphire laser, and probe the transition between the ground (S_0) and the first excited state (S_1) with its second harmonic in the blue regime. This spectroscopy directly measures if there is coupling between S_1 and S_2 via S_0.

One final note to the future 2D spectroscopy is to construct a pulse-shaper based spectroscopy in the boxcar geometry. In the pump-probe geometry, the third beam serves as the third excitation and the local oscillator, and its noise becomes the largest source of error in our measurement. Stone *et al.* [29] have demonstrated 2D spectroscopy in the boxcar geometry with a 2D

spatial-light-modulator (SLM) pulse shaper. It is also possible to convert our current pulse-shaper to make the two pump pulses propagate along different $\boldsymbol{k}$ vectors without a 2D SLM. In the boxcar geometry, the induced signal will propagate towards the fourth corner of a diamond, which is free of background. This improvement could greatly enhance the S/N of the apparatus and help to resolve finer structures in the spectrum.

Bibliography

[1] Paul Brumer and Moshe Shapiro. Control of unimolecular reactions using coherent light. *Chem. Phys. Lett*, 126(6):541–546, 1986.

[2] Doron Meshulach and Yaron Silberberg. Coherent quantum control of two-photon transitions by a femtosecond laser pulse. *Nature*, 396(2): 239–242, 1998.

[3] Doron Meshulach and Yaron Silberberg. Coherent quantum control of multiphoton transitions by shaped ultrashort optical pulses. *Phys. Rev. A*, 60(2):1287–1292, 1999.

[4] David J. Tannor and Stuart A. Rice. Control of selectivity of chemical reaction via control of wave packet evolution. *J. Chem. Phys*, 83:5013–5018, 1985.

[5] David J. Tannor, Ronnie Kosloff, and Stuart A. Rice. Control pulse sequence induced control of selectivity of reactions: Exact quantum mechanical calculations. *J. Chem. Phys*, 85:5805–5820, 1986. URL `http://link.aip.org/link/JCPSA6/v85/i10/p5805/s1`.

[6] W. Wohlleben, T. Buckup, Jennifer L. Herek, and Marcus Motzkus. Coherent control for spectroscopy and manipulation of biological dynamics. *ChemPhysChem*, 6(5):850–857, 2005.

[7] Katherine A. Walowicz, Igor Pastirk, Vadim V. Lozovoy, and Marcos Dantus. Multiphoton intrapulse interference. 1. control of multiphoton processes in condensed phases. *J. Phys. Chem. A*, 106(41):9369–9373, 2002.

[8] I. Pastirk, J. M. D. Cruz, K. A.Walowicz, V. V. Lozovoy, and M. Dantus. Selective two-photon microscopy with shaped femtosecond pulses. *Opt. Express*, 11:1695–1701, 2003.

[9] J. P. Ogilvie, D. Debarre, X. Solinas, J.-L. Martin, E. Beaurepaire, and M. Joffre. Use of coherent control for selective two-photon fluorescence microscopy in live organisms. *Opt. Express*, 14:759–766, 2006.

[10] Rajesh S. Pillai, Caroline Boudoux, Guillaume Labroille, Nicolas Olivier, Israel Veilleux, Emmanuel Farge, Manuel Joffre, and Emmanuel Beaurepaire. Multiplexed two-photon microscopy of dynamic biological samples with shaped broadband pulses. *Opt. Express*, 17(15):12741–12752, 2009.

[11] Guillaume Labroille, Rajesh S. Pillai, Xavier Solinas, Caroline Boudoux, Nicolas Olivier, Emmanuel Beaurepaire, and Manuel Joffre. Dispersion-based pulse shaping for multiplexed two-photon fluorescence microscopy. *Opt. Lett*, 35:3444–3446, 2010.

[12] D. M. Jonas. Two-dimensional femtosecond spectroscopy. *Annu. Rev. Phys. Chem.*, 54(1):425–463, 2003.

[13] A. M. Weiner. Femtosecond optical pulse shaping and processing. *Prog. Quant. Electr.*, 19:161–237, 1995.

[14] C. W. Hillegas, J. X. Tull, D. Goswami, D. Strickland, and W. S. Warren. Femtosecond laser pulse shaping by use of microsecond radio-frequency pulses. *Opt. Lett*, 19:737–739, 1994.

[15] J. X. Tull, M. A. Dugan, and W. S. Warren. High resolution, ultrafast laser pulse shaping and its applications. *Adv. Magn. Opt. Res.*, 20:1–50, 1997.

[16] W. Denk, J.H. Strickler, and W.W. Webb. 2-photon laser scanning fluorescence microscopy. *Science*, 248:73–76, 1990.

[17] K. König. Multiphoton microscopy in life sciences. *J. Microsc.*, 200(2): 83–104, 2000.

[18] P.T.C. So, C.Y. Dong, B.R. Masters, and K.M. Berland. Two-photon excitation fluorescence microscopy. *Annu. Rev. Biomed. Eng.*, 2:399–429, 2000.

[19] D. C. Cardoza and T. C. Weinacht. *Understanding and Applying Learning Control to Molecular Fragmentation.* PhD thesis, Stony Brook University, 2006.

[20] L. Davis. *A Handbook of Genetic Algorithms.* van Nostrand Reinhold, 1991.

[21] D. Zeidler, S. Frey, K.-L. Kompa, D. Proch, and M. Motzkus. Evolutionary algorithms and their application to optimal control studies. *Phys. Rev. A*, 64:023420, 2001.

[22] T. C. Weinacht and P. H. Bucksbaum. Using feedback for coherent control of quantum systems. *J. Optics B*, 4:R35–R52, 2002.

[23] Robin M. Hochstrasser. Multidimensional ultrafast spectroscopy special feature. *Proc. Natl. Acad. Sci. USA*, 104:14189–14544, 2007.

[24] T. Brixner, J. Stenger, H. M. Vaswani, M. Cho, R.E. Blankenship, and G.R. Fleming. Two-dimensional spectroscopy of electronic coupolings in photosynthesis. *Nature*, 434(7033):625–628, 2005.

[25] M. L. Cowan, J. P. Ogilvie, and R. J. D. Miller. Two-dimensional spectroscopy using diffractive optics based phased-locked photon echoes. *Chem. Phys. Lett.*, 386:184–189, 2004.

[26] T. Brixner, I.V. Stiopkin, and G. R. Fleming. Tunable two-dimensional femtosecond spectroscopy. *Opt. Lett.*, 29:884–886, 2004.

[27] T. H. Zhang, C. N. Borca, X. Q. Li, and S. T. Cundiff. Optical two-dimensional fourier transform spectroscopy with active interferometric stabilization. *Opt. Express*, 13:7432–7441, 2005.

[28] P.F. Tian, D. Keusters, Y. Suzaki, and W. S. Warren. Femtosecond phase-coherent two-dimensional spectroscopy. *Science*, 300:1553–1555, 2003.

[29] Katherine W. Stone, Kenan Gundogdu, Daniel B. Turner, Xiaoqin Li, Steven T. Cundiff, and Keith A. Nelson. Two-quantum 2d ft electronic spectroscopy of biexcitons in GaAs quantum wells. *Science*, 324(5931): 1169–1173, 2009.

[30] E. M. Grumstrup, S.-H. Shim, M. A. Montgomery, N. H. Damrauer, and M. T. Zanni. Facile collection of twodimensional electronic spectra using femtosecond pulse-shaping technology. *Opt. Express*, 15:16681–16689, 2007.

[31] Jeffrey A. Myers, Kristin L. Lewis, Patrick F. Tekavec, and Jennifer P. Ogilvie. Two-color two-dimensional fourier transform electronic spectroscopy with a pulse-shaper. *Opt. Express*, 16:17420–17428, 2008.

[32] S.-H. Shim and M. T. Zanni. How to turn your pump-probe experiment into a multidimensional spectrometer: 2d ir and vis spectroscopies via pulse shaping. *Physical Chemistry Chemical Physics*, 11:748–761, 2009.

[33] B. J. Pearson and T. C. Weinacht. Shaped ultrafast laser pulses in the deep ultraviolet. *Opt. Express*, 15:4385–4388, 2007.

[34] C.-H. Tseng and T. C. Weinacht. Shaped ultrafast laser pulses in the deep ultraviolet. *Opt. Express*, 17(21):18788–18793, 2009.

[35] C. E. Crespo-Hernandez, B. Cohen, P. M. Hare, and B. Kohler. Ultrafast excited-state dynamics in nucleic acids. *Chem. Rev.*, 104:1977, 2004.

[36] N. Dudovich, D. Oron, and Y. Silberberg. Single-pulse coherently controlled nonlinear raman spectroscopy and microscopy. *Nature*, 418: 512514, 2002.

[37] Vladislav V. Yakovlev, Christopher J. Bardeen, Jianwe Che, Jianshu Cao, and Kent R. Wilson. Chirped pulse enhancement of multiphoton absorption in molecular iodine. *J. Chem. Phys.*, 108:2309, 1998.

[38] J. J. Sakurai. *Modern Quantum Mechanics*. Addison Wesley, New York, 1994.

[39] Robert W. Boyd. *Nonlinear Optics*. Academic Press, New York, 1992.

[40] H. Barry Bebb and Albert Gold. Multiphoton ionization of hydrogen and rare-gas atoms. *Phys. Rev.*, 143:1–24, 1966.

[41] Developmental Resource for Biophysical Imaging Opto-Electronics (DRBIO) at Cornell University.

[42] R. S. Balaban and L. J. Mandel. Optical methods for the study of metabolism in intact cells. in noninvasive techniques in cell biology. In J. K. Foskett and S. Grinstein, editors, *Noninvasive Techniques in Cell Biology*, pages 213–236, New York, 1990. Wiley-Liss.

[43] B. R. Masters and B. Chance. Redox confocal imaging: intrinsic fluorescent probes of cellular metabolism. In W. T. Mason, editor, *Fluorescent and Luminescent Probes for Biological Activity*, page 4457, New York, 1993. Academic Press.

[44] Shaohui Huang, Ahmed A. Heikal, , and Watt W. Webb. Two-photon fluorescence spectroscopy and microscopy of nad(p)h and flavoprotein. *Biophysical J.*, 82:28112825, 2002.

[45] Harshad Dilip Vishwasrao. *QUANTITATIVE TWO-PHOTON REDOX FLUORESCENCE MICROSCOPY OF NEUROMETABOLIC DYNAMICS*. PhD thesis, Cornell University, 2005.

[46] D. H. Williamson, Patricia Lund, and H. A. Krebs. The redox state of free nicotinamide-adenine dinucleotide in the cytoplasm and mitochondria of rat liver. *Biochem. J.*, 103:514527, 1967.

[47] Jay R. Knutson, Joseph M. Beechem, and Ludwig Brand. Simultaneous analysis of multiple fluorescence decay curves: A global approach. *Chem. Phys. Lett.*, 102:501–507, 1983.

[48] J. R. Lakowicz. *Principles of Fluorescence Spectroscopy*. Kluwer Academic/Plenum Publishers, New York, 1990.

[49] J R Lakowicz, H Szmacinski, K Nowaczyk, and M L Johnson. Fluorescence lifetime imaging of free and protein-bound nadh. *Proc. Natl. Acad. Sci. USA*, 89(4):1271–1275, 1992.

[50] A. L. Sobolewski, W. Domcke, C. Dedonder-Lardeux, and C. Jouvet. Excited-state hydrogen detachment and hydrogen transfer driven by repulsive (1)pi sigma* states: A new paradigm for nonradiative decay in aromatic biomolecules. *Phys. Chem. Chem. Phys.*, 4:1093–1100, 2002.

[51] S. Perun, A. L. Sobolewski, and W. Domcke. Photostability of 9hadenine: mechanisms of the radiationless deactivation of the lowest excited singlet states. *Chem. Phys.*, 313:107–112, 2005.

[52] H. Chen and S. H. Li. Theoretical study toward understanding ultrafast internal conversion of excited 9h-adenine. *J. Phys. Chem. A*, 109:8443–8446, 2005.

[53] C. M. Marian. A new pathway for the rapid decay of electronically excited adenine. *J. Chem. Phys.*, 122:104314, 2005.

[54] L. Blancafort. Excited-state potential energy surface for the photophysics of adenine. *J. Am. Chem. Soc.*, 128:210–219, 2006.

[55] L. Serrano-Andrés, M. Merchán, and A. C. Borin. Adenine and 2-aminopurine: Paradigms of modern theoretical photochemistry. *Proc. Natl. Acad. Sci. U.S.A.*, 103:8691–8696, 2006.

[56] I. Conti, M. Garavelli, , and G. Orlandi. Deciphering low energy deactivation channels in adenine. *J. Am. Chem. Soc.*, 131:16108–16118, 2009.

[57] W. M. I. Hassan, W. C. Chung, N. Shimakura, S. Koseki, H. Kono, and Y. Fujimura. Ultrafast radiationless transition pathways through conical intersections in photo-excited 9h-adenine. *Phys. Chem. Chem. Phys.*, 12:5317–5328, 2010.

[58] Spiridoula Matsika. Radiaionless decay of excited states of uracil throught conical intersections. *J. Phys. Chem. A*, 108:7584–7590, 2004.

[59] M. Merchán, R. Gonzalez-Luque, T. Climent, L. Serrano-Andrés, E. Rodriuguez, M. Reguero, and D. Pelaez. Unified model for the ultrafast decay of pyrimidine nucleobases. *J. Phys. Chem. B*, 110:26471–26476, 2006.

[60] M. Z. Zgierski, S. Patchkovskii, T. Fujiwara, and E. C. Lim. On the origin of the ultrafast internal conversion of electronically excited pyrimidine bases. *J. Phys. Chem. A*, 109:93849387, 2005.

[61] T. Gustavsson, Á. Bányász, E. Lazzarotto, D. Markovitsi, M. J. Frisch G. Scalmani, V. Barone, and R. Improta. Singlet excited-state behavior of uracil and thymine in aqueous solution: A combined experimental and computational study of 11 uracil derivatives. *J. Am. Chem. Soc.*, 128:607–619, 2006.

[62] H. R. Hudock, B. G. Levine, A. L. Thompson, H. Satzger, D. Townsend, N. Gador, S. Ullrich, A. Stolow, and T. J. Martinez. Ab initio molecular dynamics and time-resolved photoelectron spectroscopy of electronically excited uracil and thymine. *J. Phys. Chem. A*, 111:8500–8508, 2007.

[63] S. Mukamel. *Principles of Nonlinear Optical Spectroscopy.* Oxford University Press, Inc., New York, 1995.

[64] M. C. Asplund, M. T. Zanni, and Robin M. Hochstrasser. Two-dimensional infrared spectroscopy of peptides by phase-controlled femtosecond vibrational photon echoes. *Proc. Natl. Acad. Sci. USA*, 97(15): 8219–8224, 2000.

[65] John D. Hybl, Allison Albrecht Ferro, and David M. Jonas. Two-dimensional fourier transform electronic spectroscopy. *J. Chem. Phys*, 115:6606–6022, 2001.

[66] Joshua C. Vaughan, T. Hornung, K. W. Stone, and Keith A. Nelson. Coherently controlled ultrafast four-wave mixing spectroscopy. *J. Phys. Chem. A*, 111:48734883, 2007.

[67] Shaul Mukamel and Roger F. Loring. Nonlinear response function for time-domain and frequency-domain four-wave mixing. *J. Opt. Soc. Am. B*, 3:595606, 1986.

[68] Yi Jing Yan and Shaul Mukamel. Electronic dephasing, vibrational relaxation, and solvent friction in molecular nonlinear optical line shapes. *J. Chem. Phys*, 89:5160–5176, 1988.

[69] Yi Jing Yan and Shaul Mukamel. Photon echoes of polyatomic molecules in condensed phases. *J. Chem. Phys*, 94:179–190, 1990.

[70] Minhaeng Cho, Norbert F. Scherer, Graham R. Fleming, and Shaul Mukamel. Photon echoes and related four-wave-mixing spectroscopies using phase-locked pulses. *J. Chem. Phys*, 96:5618–5629, 1992.

[71] M. Khalil, N. Demirdöven, , and A. Tokmakoff. Obtaining absorptive line shapes in two-dimensional infrared vibrational correlation spectra. *Phys. Rev. Lett.*, 90:047401, 2003.

[72] D. Keusters, H.S. Tan, and W.S. Warren. The role of pulse phase and direction in two dimensional optical spectroscopy. *J. Phys. Chem. A*, 103:10369, 1999.

[73] W. S. Warren and A. H. Zewail. Optical analogs of nmr phase coherent multiple pulse spectroscopy. *J. Chem. Phys.*, 75:5956–5958, 1981.

[74] J.-M. L. Pecourt, J. Peon, and B. Kohler. Ultrafast internal conversion of electronically excited rna and dna nucleosides in water. *J. Am. Chem. Soc.*, 122:9348, 2000.

[75] C. T. Middleton, K. de La Harpe, C. Su, Y. K. Law, C. E. Crespo-Hernandez, and B. Kohler. Dna excited-state dynamics: From single bases to the double helix. *Annu. Rev. Phys. Chem.*, 60:217–239, 2009.

[76] Gerd P. Pfeifer, Young-Hyun You, and Ahmad Besaratinia. Mutation research/fundamental and molecular mechanisms of mutagenesis. *Biological Effects of Ultraviolet Radiation*, 571:1931, 2005.

[77] E. Nir, C. Pltzer, K. Kleinermanns, and M. de Vries. Properties of isolated dna bases, base pairs and nucleosides examined by laser spectroscopy. *Eur. Phys. J. D*, 207:317–329, 2002.

[78] C. Canuel, M. Mons, F. Piuzzi, B. Tardivel, I. Dimicoli, and M. Elhanine. Excited states dynamics of dna and rna bases: Characterization of a stepwise deactivation pathway in the gas phase. *J. Chem. Phys D*, 122: 074316, 2005.

[79] C. Z. Bisgaard, H. Satzger, and A. Stolow S. Ullrich. Excited-state dynamics of isolated dna bases: A case study of adenine. *ChemPhysChem*, 10:101–110, 2009.

[80] J.-M. L. Pecourt, J. Peon, and B. Kohler. Dna excited-state dyhamics: Ultrafast internal conversion and vibrational cooling in a series of nucleosides. *J. Am. Chem. Soc.*, 123:10370–10378, 2001.

[81] B. Cohen, P. M. Hare, and B. Kohler. Ultrafast excited-state dynamics of adenine and monomethylated adenines in solution: Implications for the nonradiative decay mechanism. *J. Am. Chem. Soc.*, 125:13594–13601, 2003.

[82] P. M. Hare, C. E. Crespo-Hernández, and B. Kohler. Solvent-dependent photophysics of 1-cyclohexyluracil: Ultrafast branching in the initial bright state leads nonradiatively to the electronic ground state and a long-lived $^1n\pi^*$ state. *J. Phys. Chem. B*, 110:18641, 2006.

[83] Chris T. Middleton, Boiko Cohen, and Bern Kohler. Solvent and solvent isotope effects on the vibrational cooling dynamics of a dna base derivative. *J. of Phys. Chem. A*, 111:10460–10467, 2007.

[84] P. M. Hare, C. E. Crespo-Hernandez, and B. Kohler. Internal conversion to the electronic ground state occurs via two distinct pathways for the pyrimidine bases in aqueous solution. *Proc. Natl. Acad. Sci. U.S.A.*, 104: 435–440, 2007.

[85] W.-M. Kwok, C. Ma, and D. L. Phillips. Femtosecond time- and wavelength- resolved fluorescence and absorption spectroscopic study of the excited states of adenosine and an adenine oligomer. *J. Am. Chem. Soc.*, 128:11894–11905, 2006.

[86] J. Peon and A. H. Zewail. Dna/rna nucleotides and nucleosides: direct measurement of excited-state lifetiimes by femtosecond fluorescence upconversion. *Chem. Phys. Lett.*, 348:255–262, 2001.

[87] T. Gustavsson, A. Sharonov, D. Onidas, and D. Markovitsi. Adenine, deoxyadenosine and deoxyadenosine 5-monophosphate studied by fem-

tosecond flrorescence upconversion spectroscopy. *Chem. Phys. Lett.*, 356: 49–54, 2002.

[88] T Gustavsson, Á. Bányász, E. Lazzarotto, D. Markovitsi, G. Scalmani, M. J. Frisch, V. Barone, and R. Improta. Singlet excited-state behavior of uracil and thymine in aqueous solution: A combined experimental and computational study of 11 uracil derivatives. *J. Am. Chem. Soc.*, 128:607–619, 2006.

[89] Thomas Gustavsson, Á. Bányász, Nilmoni Sarkarb, Dimitra Markovitsia, and Roberto Improta. Assessing solvent effects on the singlet excited state lifetime of uracil derivatives: A femtosecond fluorescence upconversion study in alcohols and D_2O. *Chem. Phys.*, 350:186–192, 2008.

[90] Á. Bányász, T. Gustavsson, E. Keszei, R. Improta, and D. Markovitsi. Effect of amino substitution on the excited state dynamics of uracil. *Photochem. Photobiol. Sci.*, 7:765–768, 2008.

[91] T. Gustavsson, R. Improta, and D. Markovitsi. DNA/RNA: Bulding blocks of life under uv irradiation. *J. Phys. Chem. Lett.*, 1:2025–2030, 2010.

[92] Graham R. Fleming and Minhaeng Cho. Chromophore-solvent dynamics. *Annu. Rev. Phys. Chem.*, 47:109–134, 1996.

[93] P. F. Tekavec, J. A. Myers, K. L. M. Lewis, and J. P. Ogilvie. Two-dimensional electronic spectroscopy with a continuum probe. *Opt. Lett.*, 34:1390–1392, 2009.

[94] Marija Kotur, Thomas C. Weinacht, Congyi Zhou, and Spiridoula Matsika. Following ultrafast radiationless relaxation dynamics with strong field dissociative ionization: A comparison between adenine, uracil, and cytosine. *IEEE Journal of Selected Topics in Quantum Electronics*, 99: 1–8, 2011.

[95] C. Lifschitz, E. D. Bergmann, and B. Pullman. The ionization potentials of biological purines and pyrimidines. *Tetrahedron Lett.*, 46:4583–4586, 1967.

[96] N. S. Hush and A. S. Cheung. Ionization potentials and donor properties of nucleic acid bases and related compounds. *Chem. Phys. Lett.*, 34:11–13, 1975.

[97] A. Padva, P. R. LeBreton, R. J. Dinerstein, and J. N. A. Ridyard. Uv photoelectron studies of biological pyrimidines: The electronic structure of uracil. *Biochem. Biophys. Res. Commun.*, 60(4):1262–1268, 1974.

[98] S. Perun, A. L. Sobolewski, , and W. Domcke. Ab initio studies on the radiationless decay mechanisms of the lowest excited singlet states of 9h-adenine. *J. Am. Chem. Soc.*, 127:6257–6265, 2005.

[99] Bern Kohler. Nonradiative decay mechanisms in dna model systems. *J. Phys. Chem. Lett.*, 1:2047–2053, 2010.

[100] Soujanya Yarasi, Susan Ng, and Glen R. Loppnow. Initial excited-state structural dynamics of uracil from resonance raman spectroscopy are different from those of thymine (5-methyluracil). *J. Phys. Chem. B*, 113:14336–14342, 2009.

[101] Sulayman A. Oladepo and Glen R. Loppnow. Initial excited-state structural dynamics of 9-methyladenine from uv resonance raman spectroscopy. *J. Phys. Chem. B*, 115:6149–6156, 2011.

[102] Susan S. Ng, Faranak Teimoory, and Glen R. Loppnow. Mass-tuned initial excited-state structural dynamics of dna nucleobases from uv resonance raman spectroscopy: 5-deuterouracil. *J. Phys. Chem. Lett.*, 2: 2362–2365, 2011.

[103] Soo-Y. Lee and E. J. Heller. Time-dependent theory of raman scattering. *J. Chem. Phys.*, 71:4777–4788, 1979.

[104] Anne B. Myers and Richard A. Mathies. Excited-state torsional dynamics of cis-stilbene from resonance raman intensities. *J. Chem. Phys.*, 81: 1552–1558, 1984.

[105] Anne B. Myers. *Excited Electronic State Properties from Ground-State Resonance Raman Intensities. In Laser Techniques in Chemistry.* Wiley, New York, 1995.

[106] Anne Myers Kelley. Resonance raman intensity analysis of vibrational and solvent reorganization in photoinduced charge transfer. *J. Phys. Chem. A*, 103:6891–6903, 1999.

[107] John D. Hybl, Anchi Yu, Darcie A. Farrow, and David M. Jonas. Polar solvation dynamics in the femtosecond evolution of two-dimensional fourier transform spectra. *J. Phys. Chem. A*, 106(34):7651–7654, 2002.

[108] Sean T. Roberts, Joseph J. Loparo, and Andrei Tokmakoff. Characterization of spectral diffusion from two-dimensional line shapes. *J. Chem. Phys.*, 125:084502–1–084502–8, 2006.

[109] C. E. Crespo-Hernandez, Boiko Cohen, and B. Kohler. Base stacking controls excited-state dynamics in a·t dna. *Nature*, 436:1141–1144, 2005.

[110] J. J. Holbrook and R. G. Wolfe. Malate dehydrogenase. x. fluorescence microtitration studies of d-malate, hydroxymalonate, nicotinamide dinucleotide, and dihydronicotinamide-adenine dinucleotide binding by mitochondrial and supernatant porcine heart enzymes. *Biochemistry*, 11 (13):2499, 1972.

Appendix A

Appendix: NADH Solution Preparation

The NADH solution and the NADH+MDH mixture were prepared in the following procedure: powdered NADH (Acros, CAS 606-68-8) was first mixed into Trizma (Sigma Aldrich, hydrochloride buffer solution, pH 7.0, 1 M) solution to reach the desired molar concentration. Different amount of mMDH (Roche, pH ~ 6) in 3.2 M ammonium sulfate solution was then mixed into the free NADH solution to reach the stated molar concentrations. The binding fraction of the enzyme and NADH mixture is determined by the equilibrium formula $K_d = \frac{[N]\times[M]}{[A]}$, where [N], [M] and [A] are the equilibrium molar concentrations of NADH, mMDH and mMDH-bound NADH respectively, and $K_d = 4.7$ μM [110] is the dissociation constant. Different solutions are then put into a 10 mm path length glass fluorometer cuvette (NSG precision cells) separately and illuminated by π phase step pulses.

Appendix B

Appendix: Inhomogeneous Line-broadening

In Section 4.2.1, we define the spectral inhomogeneous lineshape broadening as $\chi(\omega)$. In this appendix, we will explain why the inhomogeneous broadening can be represented as $\chi(t_3 - t_1)$ in the rephasing process, and for the non-rephasing process, it is in the form of $\chi(t_3 + t_1)$.

Most molecules scientists interested in are, unavoidably, immersed in a solid, liquid, or dense gas and interacts with many degrees of freedom of the so-called bath. Theories on spectral line-broadening traditionally describe broadening in two extreme cases. The inhomogeneous broadening arises from molecules absorbing at different frequencies because of different local environments. As a result, different molecules exhibit different transition lineshapes. The broadening is static and carries no dynamic information. Inhomogeneous broadening is described by convoluting the response function with a distribution of transition frequencies. In contrast, the homogeneous broadening reflects an interaction with the bath on a fast timescale, and the transition lineshapes of all molecules are broadened equally.

B.1 Time evolution operator of a time dependent Hamiltonian

In Chapter 2.2, the time evolution operator with respect to the Hamiltonian H_0 is defined as $U_0(t, t_0 = 0) = e^{-iH_0 t/\hbar}$, which is true only for time-independent H_0. To generalize the definition of the time-evolution operator to the case of a time-dependent Hamiltonian, we plug in $|\psi, t_0; t\rangle_S = U_0(t, t_0)|\psi, t_0\rangle_S$ to the time-dependent Schrödinger equation:

$$\begin{aligned} \frac{\partial}{\partial t} U_0(t, t_0)|\psi, t_0\rangle_S &= -\frac{-i}{\hbar} H_0(t) U_0(t, t_0)|\psi, t_0\rangle_S \\ \frac{\partial}{\partial t} U_0(t, t_0) &= \frac{-i}{\hbar} H_0(t) U_0(t, t_0) \end{aligned} \tag{B.1}$$

Integrating both side of Eq. B.1, we get the integral form of $U_0(t, t_0)$

$$U_0(t, t_0) = 1 - \frac{i}{\hbar} \int_{t_0}^{t} d\tau H(\tau) U_0(\tau, t_0) \tag{B.2}$$

Applying time-perturbation theory to Eq. B.2, we obtain the expansion in the form of a time-ordered integral

$$\begin{aligned} U_0(t, t_0) = 1 + \sum_{n=1}^{\infty} \left(\frac{-i}{\hbar}\right)^n \int_{t_0}^{t} d\tau_n \int_{t_0}^{\tau_n} d\tau_{n-1} \ldots \int_{t_0}^{\tau_2} d\tau_1 \\ H_0(\tau_n) H_0(\tau_{n-1}) \ldots H_0(\tau_1) \end{aligned} \tag{B.3}$$

where $\tau_1 \leq \tau_2 \leq \cdots \leq \tau_n$. To facilitate the discussion, we define a positive time ordered exponential and denote it as follows

$$\begin{aligned} \exp_+ \left[\frac{-i}{\hbar} \int_{t_0}^{t} d\tau H_0(\tau)\right] &\equiv 1 + \sum_{n=1}^{\infty} \left(\frac{-i}{\hbar}\right)^n \int_{t_0}^{t} d\tau_n \int_{t_0}^{\tau_n} d\tau_{n-1} \ldots \int_{t_0}^{\tau_2} d\tau_1 \\ &= H_0(\tau_n) H_0(\tau_{n-1}) \ldots H_0(\tau_1) U_0(t, t_0) \end{aligned} \tag{B.4}$$

Similarly, the adjunct of the time evolution operator can be written as the negative time ordered exponential:

$$\begin{aligned}\exp_{-}\left[\frac{i}{\hbar}\int_{t_0}^{t} d\tau H_0(\tau)\right] &\equiv 1+\sum_{n=1}^{\infty}\left(\frac{i}{\hbar}\right)^n \int_{t_0}^{t} d\tau_n \int_{t_0}^{\tau_n} d\tau_{n-1}\ldots\int_{t_0}^{\tau_2} d\tau_1 \\ &= H_0(\tau_1)H_0(\tau_2)\ldots H_0(\tau_n)U_0^{\dagger}(t,t_0) \end{aligned} \tag{B.5}$$

The time evolution operator will be used in the following section where we incorporate solvent effects to the electronic transitions.

B.2 Fluctuating transition frequencies for a two electronic level system

For a two-level system with a ground state $|g\rangle$ and an electronically exited state $|e\rangle$, which are coupled to nuclear degrees of freedom $\mathbf{q}$. In the Born Oppenheimer approximation, the adiabatic Hamiltonian is given by

$$H = |g\rangle H_g(\mathbf{q})\langle g| + |e\rangle H_e(\mathbf{q})\langle e| \tag{B.6}$$

where

$$\begin{aligned} H_g(\mathbf{q}) &= T(\mathbf{q}) + W_g(\mathbf{q}) \\ H_e(\mathbf{q}) &= \hbar\omega_{eg}^0 + T(\mathbf{q}) + W_e(\mathbf{q}) \end{aligned} \tag{B.7}$$

$T(\mathbf{q})$ is the nuclear kinetic energy and $W_e(\mathbf{q})$ and $W_g(\mathbf{q})$ are the adiabatic potential for the excited and ground states respectively. $\hbar\omega_{eg}^0$ is the energy gap between the minima of the two states. Now we introduce the energy gap operator $\Omega = H_e - H_g - \hbar\omega_{eg}$, where $\hbar\omega_{eg}$ refers to the average energy gap. We first look into the linear absorption, from Eq. 4.34, the first term in the

equation is:

$$\begin{aligned} J(t_1) &\equiv \langle \mu_I(t_1)\mu_I(0)\rho(-\infty)\rangle \\ &= \langle \mu_{ge}(t_1)\mu_{eg}(0)\rho(-\infty)\rangle \\ &= \left\langle e^{-\frac{i}{\hbar}H_g t_1}\mu_{ge}e^{-\frac{i}{\hbar}H_e t_1}\mu_{eg}\rho(-\infty)\right\rangle \\ &= \left\langle e^{-\frac{i}{\hbar}H_g t_1}\mu_{ge}e^{-\frac{i}{\hbar}(H_g+\Omega+\hbar\omega_{eg})t_1}\mu_{eg}\rho(-\infty)\right\rangle \\ &= e^{-i\omega_{eg}t_1}\mu^2\left\langle \exp_+\left(-i\int_0^{t_1}d\tau\Omega(\tau)\right)\rho(-\infty)\right\rangle \end{aligned} \tag{B.8}$$

where $\Omega(\tau)$ is the electronic energy gap operator in the interaction picture with respect to the ground state:

$$\Omega(\tau) \equiv e^{\frac{i}{\hbar}H_g\tau}\Omega e^{\frac{-i}{\hbar}H_g\tau} \tag{B.9}$$

Eq. B.8 can be generalized to third-order response. The Liouville pathway R_1 in Eq. 4.39 can be rewritten as

$$\begin{aligned} R_1 &= \langle \mu_{ge}(t_3+t_2+t_1)\mu_{eg}(0)\rho(-\infty)\mu_{ge}(t_1)\mu_{eg}(t_2+t_1)\rangle \\ &= \langle \mu_{ge}(t_1)\mu_{eg}(t_1+t_2)\mu_{ge}(t_1+t_2+t_3)\mu_{eg}(0)\rho(-\infty)\rangle \\ &= \langle \exp\left[\frac{i}{\hbar}H_g t_1\right]\mu_{ge}\exp\left[\frac{-i}{\hbar}H_e t_1\right]\exp\left[\frac{i}{\hbar}H_e(t_1+t_2)\right]\mu_{eg}\exp\left[\frac{-i}{\hbar}H_g(t_1+t_2)\right] \\ &\times \exp\left[\frac{i}{\hbar}H_g(t_1+t_2+t_3)\right]\mu_{ge}\exp\left[\frac{-i}{\hbar}H_e(t_1+t_2+t_3)\right]\mu_{eg}\rho(-\infty)\rangle \\ &= \exp(-i\omega_{eg}t_1 - i\omega_{eg}t_3) \\ &\times \langle \mu_{ge}^2\mu_{eg}^2\exp_+\left[-i\int_0^{t_1}d\tau\Omega(\tau)\right]\exp_-\left[i\int_0^{t_1+t_2}d\tau\Omega(\tau)\right] \\ &\times \exp_+\left[-i\int_0^{t_1+t_2+t_3}d\tau\Omega(\tau)\right]\rho(-\infty)\rangle \end{aligned} \tag{B.10}$$

where we utilize results from Eqs. B.8 and B.9 in the last step of the derivation.

Similarly, the other Liouville pathways can be expressed as:

$$\begin{aligned} R_2 &= \exp(i\omega_{eg}t_1 - i\omega_{eg}t_3) \\ &\times \langle \mu_{ge}^2 \mu_{eg}^2 \exp_- \left[i \int_0^{t_1+t_2} d\tau \Omega(\tau) \right] \exp_+ \left[-i \int_0^{t_1+t_2+t_3} d\tau \Omega(\tau) \right] \\ &\times \exp_+ \left[-i \int_0^{t_1} d\tau \Omega(\tau) \right] \rho(-\infty) \rangle \end{aligned} \tag{B.11}$$

$$\begin{aligned} R_3 &= \exp(i\omega_{eg}t_1 - i\omega_{eg}t_3) \\ &\times \langle \mu_{ge}^2 \mu_{eg}^2 \exp_- \left[i \int_0^{t_1} d\tau \Omega(\tau) \right] \exp_+ \left[-i \int_0^{t_1+t_2+t_3} d\tau \Omega(\tau) \right] \\ &\times \exp_- \left[i \int_0^{t_1+t_2} d\tau \Omega(\tau) \right] \rho(-\infty) \rangle \end{aligned} \tag{B.12}$$

$$\begin{aligned} R_4 &= \exp(-i\omega_{eg}t_1 - i\omega_{eg}t_3) \\ &\times \langle \mu_{ge}^2 \mu_{eg}^2 \exp_+ \left[-i \int_0^{t_1+t_2+t_3} d\tau \Omega(\tau) \right] \exp_- \left[i \int_0^{t_1+t_2} d\tau \Omega(\tau) \right] \\ &\times \exp_+ \left[-i \int_0^{t_1} d\tau \Omega(\tau) \right] \rho(-\infty) \rangle \end{aligned} \tag{B.13}$$

By performing an ensemble average of Eqs. B.10-B.13 over the distribution of Ω, the response functions become

$$R_\alpha(t_3, t_2, t_1) = R_\alpha^H(t_3, t_2, t_1)\chi(t_3 \pm t_1) \tag{B.14}$$

Where R_α^H is the homogeneous part of the response function. The $\chi(t_3 \pm t_1)$ function is the inhomogeneous broadening that comes from the ensemble average of the $\exp[-i\omega_{eg}(t_3 \pm t_1)]$ factor. For rephasing pathways R_2 and R_3, $\chi = \chi(t_3 - t_1)$, and for non-rephasing pathways R_1 and R_4, $\chi = \chi(t_3 + t_1)$